



**Derivation of Atmospheric Water Based on Radio  
Signals, Frequency Manipulation and Intersatellite  
Communication Network.**



**STUDENT NAME:** Ramson Munyaradzi Nyamukondiwa

**STUDENT ID:** 205F5003

**SUPERVISOR:** Professor Mengu Cho

Department of Engineering  
Graduate School of Engineering  
Kyushu Institute of Technology  
Kitakyushu, Japan

Thesis submitted in partial fulfillment of the requirements  
for the degree of  
**Doctor of Philosophy in Engineering (Ph.D.)** in Electrical and Space Systems  
Engineering  
**December, 2023**



## ABSTRACT

The atmospheric total water vapor content (TWVC) affects climate change, weather patterns, and radio signal propagation. Recent techniques such as global navigation satellite systems (GNSS) are used to measure TWVC but with either compromised accuracy, temporal resolution, or spatial coverage. This study demonstrates the feasibility of predicting, mapping, and measuring TWVC using spread spectrum (SS) radio signals and software-defined radio (SDR) technology on low Earth-orbiting (LEO) satellites. An intersatellite link (ISL) communication network from a constellation of small satellites is proposed to achieve three-dimensional (3D) mapping of TWVC. However, the calculation of TWVC from satellites in LEO contains contribution from the ionospheric total electron content (TEC). The TWVC and TEC contribution are determined based on the signal propagation time delay and the satellites' positions in orbit. Since TEC is frequency dependent unlike TWVC, frequency reconfiguration algorithms have been implemented to distinguish TWVC. The novel aspects of this research are the implementation of time stamps to deduce time delay, the unique derivation of TWVC from a constellation setup, the use of algorithms to remotely tune frequencies in real time, and ISL demonstration using SDRs. This mission could contribute to atmospheric science, and the measurements could be incorporated into the global atmospheric databases for climate and weather prediction models.

**Keywords:** total water vapor content; total electron content; frequency reconfiguration; intersatellite link; software-defined radio; small satellites.

## ACKNOWLEDGEMENT

In the pursuit of knowledge and the completion of this Ph.D. journey in Electrical and Space Systems Engineering, I am humbled and profoundly grateful for the support, guidance, and blessings I have received along the way. First and foremost, I offer my heartfelt thanks to the Almighty God, whose unwavering presence and guidance have been my source of strength and inspiration throughout this academic odyssey. Your divine wisdom has illuminated my path and granted me the resilience to overcome challenges and reach this significant milestone. I owe a debt of gratitude to my esteemed supervisor, Professor Mengu Cho, whose mentorship and unwavering belief in my potential have been pivotal in shaping my research and nurturing my growth as a scholar. Your dedication to academic excellence, tireless guidance, and visionary leadership have left an indelible mark on my academic and personal development. To my cherished family members, I extend my deepest appreciation for your unending love, encouragement, and unwavering support. Your sacrifices, understanding, prayers, motivation, and belief in my aspirations have been the bedrock upon which I have built my academic journey. I am profoundly thankful for your presence in my life. My heartfelt gratitude also goes out to my dedicated colleagues and peers in the field of Electrical and Space Engineering. Your collaboration, intellectual exchange, and collective pursuit of knowledge have made this academic endeavour an enriching and rewarding experience. The camaraderie and shared passion for exploration have fuelled my determination. In addition, I am grateful to the wider academic community, mentors, and institutions that have contributed to my education and research. Kyushu Institute of Technology and its exceptional resources, libraries, and research opportunities have been instrumental in my academic growth. I also acknowledge the support provided by the government of Zimbabwe, the Zimbabwe National Geospatial and Space Agency (ZINGSA), the University of Zimbabwe (UZ) and Professor Cho Laboratory (LaSEINE), which made this research possible and allowed me to focus on advancing our understanding of the field. Lastly, I extend my appreciation to my friends and loved ones for their patience, encouragement, and unwavering belief in my abilities, especially during the demanding periods of this academic journey. In closing, this Ph.D. thesis represents the culmination of years of dedication and hard work, and it would not have been possible without the blessings and contributions of many. Each of you has played a vital role in this achievement, and for that, I am profoundly grateful. With heartfelt thanks,

**Ramson Munyaradzi Nyamukondiwa, Kyushu Institute of Technology, December, 2023.**

## Contents

<b>ABSTRACT</b> .....	i
<b>ACKNOWLEDGEMENT</b> .....	ii
<b>LIST OF FIGURES</b> .....	vii
<b>LIST OF TABLES</b> .....	x
<b>LIST OF ABBREVIATION</b> .....	xi
<b>CHAPTER 1</b> .....	1
<b>INTRODUCTION</b> .....	1
<b>1.1 Overview</b> .....	1
<b>1.2 Problem Statement</b> .....	3
<b>1.3 Motivation, Challenges and Research Questions</b> .....	7
<b>1.4 Research Aim</b> .....	10
<b>1.5 Research Objectives</b> .....	10
<b>1.6 Mission Requirements</b> .....	11
<b>1.7 Research Scope</b> .....	11
<b>1.8 Research Methodology</b> .....	12
<b>1.9 Research Novelty and Contribution</b> .....	13
<b>1.10 Dissertation Organization</b> .....	14
<b>CHAPTER 2</b> .....	16
<b>LITERATURE REVIEW</b> .....	16
<b>2.1 Overview</b> .....	16
<b>2.2 Atmospheric Water Vapor and Impact of Climate Change</b> .....	16
<b>2.2.1 Contribution of Atmospheric Water Vapor to Greenhouse Effects</b> .....	16
<b>2.2.2 Resultant Disruptive Weather Patterns and Climate Changes</b> .....	19
<b>2.3 Measurement of Atmospheric Water Vapor and Total Electron Content</b> .....	19
<b>2.3.1 The Normalized Differential Spectral Attenuation (NDSA)</b> .....	19
<b>2.3.2 The GNSS Concept</b> .....	21
<b>2.3.3 Medium and Moderate Resolution Imaging Spectroradiometer (MODIS and MERIS)</b>	26

2.3.4	The Interferometric Synthetic Aperture Radar (In-SAR) .....	26
2.3.5	The Very-long-baseline interferometry (VLBI) .....	28
2.3.6	The Geostationary Satellite Observation .....	29
2.3.7	SPIRE Satellite Constellation .....	31
2.3.8	Kyutech Spatium Projects .....	31
2.3.9	Others: Surface Meteorology, Radio Sonde, Lidar, Microwave Radiometers, Stratospheric Ballons .....	33
2.4	Summary of Atmospheric Water Vapor and TEC Measurement Techniques .....	39
	<b>CHAPTER 3</b> .....	<b>41</b>
	<b>SATELLITE AND GROUND SYSTEMS DESIGN CONFIGURATION</b> .....	<b>41</b>
3.1	Overview .....	41
3.2	Proposed System Design Configuration for Measuring TWVC .....	41
3.2.1	Satellite Mission Board Hardware .....	41
3.2.1.1	USRP 205mini-i Software Define Radio (SDR) Transceiver .....	42
3.2.1.1.1	USRP 205mini-i SDR Output Power .....	45
3.2.1.2	Raspberry Pi and Software's .....	46
3.2.1.3	GPS System .....	47
3.2.1.4	RF Switch Mechanism .....	48
3.2.1.5	RF Amplifier and Delay Pulse Generator .....	49
3.2.2	Satellite Design Configuration .....	50
3.2.3	Mission Execution Sequency .....	51
3.2.4	Mission Succession Criteria .....	53
3.3	Proposed Ground Station Design Configuration .....	54
3.3.1	Primary Channel Configuration .....	54
3.3.2	Secondary Channel Configuration .....	55
3.3.3	GS Data Budget Computation .....	55
	<b>CHAPTER 4</b> .....	<b>57</b>
	<b>INTERSATELLITE LINK RANGING AND CONSTELLATION MANAGEMENT</b> .....	<b>57</b>
4.1	Overview .....	57
4.2	Intersatellite Link Ranging .....	57
4.2.1	Implemented ISL network with SS- BPSK Coding Scheme .....	64

4.2.1.1	SS-BPSK Transmitter.....	65
4.2.1.2	SS-BPSK Receiver.....	67
4.2.1.2.1	SS Frequency Detection at the Receiver .....	69
4.2.1.2.2	SS BPSK Received Signal Constellations.....	70
4.2.1.2.3	SS BPSK Time Oscilloscopes .....	70
4.3	Management of ISL Satellite Constellation .....	72
	<b>CHAPTER 5.....</b>	<b>77</b>
	<b>WATER VAPOR MEASUREMENT CONCEPT, FREQUENCY MANIPULATION</b>	
	<b>AND MISSION DETERMINATION BASED ON TIME DELAY EVALUATIONS.....</b>	<b>77</b>
5.1	Overview .....	77
5.2	Theoretical Deduction of Atmospheric Water Vapor.....	<b>Error! Bookmark not defined.</b>
5.2.1	Procedure to Determine the Time Delay.....	85
5.2.2	Procedure to Determine the ISL Frequency Bands .....	84
5.3	Frequency Reconfiguration in the ISL Network.....	85
5.3.1	Feasibility of Frequency Manipulation .....	85
5.3.2	Procedure of Modified XML-RPC Algorithm .....	88
5.3.3	Procedure of the TCP/IP Algorithm .....	89
5.3.4	Frequency Manipulation Results and Analysis.....	89
5.4	Determination of Location Data .....	92
5.5	Time Stamping with 1PPS GPS Signal .....	93
5.6	Delayed Time Stamp using Delay Pulse Generator .....	95
5.7	ISL Communication Feasibility.....	97
	<b>CHAPTER 6.....</b>	<b>100</b>
	<b>DISCUSSIONS, CONCLUSION AND FUTURE WORK .....</b>	<b>100</b>
6.1	Discussions .....	100
6.2	Conclusions and Future Work.....	104
	<b>APPENDIXs.....</b>	<b>106</b>
	<b>Systems Integration Configuration .....</b>	<b>106</b>
A.	Integration configuration of RPi GNU and USRP SDR.....	106
B.	RPi and GPS Integration.....	109
C.	SS-BPSK_transceiver_with_XMLPC server algorithm.....	115

<b>D.</b>	<b>XMLRPC external python client program 1</b> .....	121
<b>E.</b>	<b>XMLRPC client program 2</b> .....	122
<b>F.</b>	<b>SS-BPSK with TCP/IP server algorithm</b> .....	125
<b>G.</b>	<b>TCP/IP external python client program 1</b> .....	135
<b>H.</b>	<b>TCP/IP telnet client program 2</b> .....	135
<b>I.</b>	<b>Other software</b> .....	139
<b>I.</b>	<b>Audacity</b> .....	139
<b>II.</b>	<b>FavBin Edit</b> .....	139
<b>III.</b>	<b>MATLAB programs</b> .....	139
<b>IV.</b>	<b>SDRAngel/ SDR Sharp</b> .....	140
<b>V.</b>	<b>Power Viewer</b> .....	140
	<b>References</b> .....	141



## LIST OF FIGURES

Figure 1. Depicts the global distribution of (a) catastrophes, (b) mortality, and (c) economic losses by hazard category and decade. Source: World Meteorological Organization[7].....	2
Figure 2. Climate risk management and adaptation framework.....	2
Figure 3. Atmospheric water vapor measurement techniques .....	3
Figure 4. 3D Mapping of atmospheric TWVC .....	8
Figure 5. Atmospheric water vapor implementation methodology .....	12
Figure 6. Percentage of atmospheric water vapor to (a) Greenhouse gases (b) The troposphere. 17	
Figure 7. Positive and negative contribution of TWVC to greenhouse gases .....	17
Figure 8. GNSS satellites probing of the troposphere and ionosphere and received with ground-based GPS receiver [61].....	22
Figure 9. GNSS radio occultation rising and setting scenarios for assessing the ionosphere and the neutrosphere. ....	25
Figure 10. Tropospheric delay effect on SAR .....	27
Figure 11. <a href="https://www.sciencedirect.com/topics/earth-and-planetary-sciences/geostationary-satellite">https://www.sciencedirect.com/topics/earth-and-planetary-sciences/geostationary-satellite</a> .....	30
Figure 12. Kyutech SPATIUM satellites (a) SPATIUM-I (b) KISTUNE carry SPATIUM-II payload.....	32
Figure 13. USRP B205 mini-i SDR board.....	43
Figure 14. USRP B205mini-I schematic   ETTUS research SDR architecture [91].....	43
Figure 15. Power meter measurement test for SDR output power .....	45
Figure 16. (USRP B205 mini-i maximum output power).....	45
Figure 17. USRP output power vs gain curve.....	46
Figure 18. Raspberry Pi-4 model B configuration with SDR.....	47
Figure 19. GPS module Orion B16.....	48
Figure 20. RF switch schematic and board (credit: Inherited from KITSUNE satellite) .....	49
Figure 21. Delay pulse generator and specifications .....	49
Figure 22. System design configuration block diagram .....	50
Figure 23. Mission execution scenario. ....	52
Figure 24. Ground station setup.....	54
Figure 25. ISL deployment statistics.....	58

Figure 26. ISL network test bed.....	65
Figure 27. SS-BPSK transmitter at Sat A. ....	66
Figure 28. SS-BPSK receiver at Sat B.....	67
Figure 29. Recovered SS-transmitted GPS data at Sat B.....	68
Figure 30. Decoded SS-transmitted GPS data at Sat B. ....	68
Figure 31. (a) Frequency spectrum at 400.15 MHz: brown: upper bound, pink: lower bound, blue: average spectrum; (b) Frequency spectrum at 460 MHz: brown: upper bound, pink: lower bound, blue: average spectrum .....	69
Figure 32. (a) Constellation at 400.15 MHz; (b) Constellation at 460 MHz. ....	70
Figure 33. (a) Time domain oscillograph at 400.15 MHz (b) Time domain oscillograph at 460 MHz .....	71
Figure 34. (a) Correlated data graph at 400.15 MHz (b) Correlated data graph at 460 MHz .....	72
Figure 35 (a) Altitude vs vapor density (b) TWVC variation of altitude vs temperature .....	78
Figure 36. (a) TEC variations of altitude vs electron density. (b) Delayed wave in tropo- ionosphere region.....	79
Figure 37. TWVC probing with the ISL network.....	81
Figure 38. Time delay deductions.....	81
Figure 39. Mission execution scenario .....	85
Figure 40. Frequency manipulation flow diagrams: (a) XML-RPC algorithm architecture; (b) TCP/IP algorithm architecture. ....	87
Figure 41. Static and dynamic parameters .....	88
Figure 42. Demonstration of frequency manipulation: (a) 460.00 MHz to 400.15 MHz; (b) 400.15 MHz to 460.00 MHz. ....	89
Figure 43. Demonstration of frequency manipulation.....	90
Figure 44. Server-Client connection confirmation inside the GNURadio.....	91
Figure 45. Results of time and location data.....	92
Figure 46. GPS location confirmed by google maps .....	92
Figure 47. Synchronized 1PPS GPS signal for Tx (yellow) and for Rx (blue). ....	93
Figure 48. Sample of data at 1 MSPS at 460.00 MHz. ....	93
Figure 49. Analysis of data frames from the received signal at 450 MHz and 1 MSPS.....	94
Figure 50. GPS 1PPS pulse (yellow) and a delay pulse (blue) output of delay pulse generator. .	96

Figure 51. Results of the test with delay pulse generator at 400.15 MHz with large delay.....	96
Figure 52. Results of the test with delay pulse generator at 460 MHz with small delay.....	96
Figure 53. Sensitivity test setup.....	97
Figure 54. Deployable helix antenna Simulations .....	101

## LIST OF TABLES

Table 1. Comparison of greenhouse gases [53]. .....	18
Table 2. Comparison of water vapor measurement methods .....	39
Table 3. List of satellite mission hardware and functions.....	41
Table 4. Details the main specifications of the SDR in both paths.....	43
Table 5: SDR output power vs corresponding gains.....	46
Table 6. Mission success criteria .....	53
Table 7. Data budget .....	55
Table 8. Intersatellite missions between 2000 and 2023.....	58
Table 9. SS signal data format .....	66
Table 10. Frequency selection table.....	84
Table 11. Comparison of XML-RPC and TCP/IP algorithms.....	91
Table 12. Sensitivity test results (o: full packets decoded, $\Delta$ : partial decoding, x: failed to decode).....	98
Table 13. Link budget for ISL network.....	99
Table 14. GPS performance assessments.....	102

## LIST OF ABBREVIATION

TWVC	Total Water Vapor Content
P/I/S WV	Precipitable/Integrated/Slant Water Vapor
TEC	Total Electron Content
GNSS	Global Navigation Satellite System
ISL	Intersatellite Link
LEO	Low Earth Orbit
UHF	Ultra-High Frequency
SDR	Software Defined Radio
BPSK	Binary Phase Shift Keying
GPS	Global Positioning Systems
SDG	Sustainable Development Goal
NWP	Numerical Weather Prediction
GCM	Global Climate Model
GIM	Global Ionospheric Model
CRMA	Climate Mapping for Resilience and Adaption Model
SS	Spread Spectrum
COTS	Commercial Off the Shelf Components
WMO	World Meteorological Organization
I/Q	Inphase/Quadrature
NDSA	Normalized Differential Spectral Attenuation
2/3/-D	Two/Three Dimensional
STD	Slant Tropospheric Delay
ZTD	Zenith Total Delay
ZHD	Zenith Hydrostatic Delay
ZWD	Zenith Wet Delay
RO	Radio Occultation
InSAR	Interferometric Synthetic Aperture Radar
MERIS	MEDium Resolution Imaging Spectrometer
MODIS	MODerate Resolution Imaging Spectrometer
DEM	Digital Elevation Model

VLBI	Very Long Baseline Interferometry
EOP	Earth Orientation Parameter
MTSAT	Multi-Functional Transport Satellite
GOES	Geostationary Operational Environmental Satellite
SWCVR	Split-Window Covariance-Variance Ratio
EDP	Electron Density Profile
CSAC	Chip-Scale Atomic Clock
LIDAR	Light Detection and Ranging
MODIS	Moderate Resolution Imaging
MERIS	Medium Resolution Imaging
InSAR	Interferometric Synthetic Aperture Radar
SDSM	Statistical Downscaling Model
ANN	Artificial Neural Network
SPATIUM	Space Precision Atomic-Clock Timing Utility Mission
XML-RPC	Extensible Markup Language Remote Procedure Call
TCP/IP	Transport Control Protocol/Internet Protocol
GS	Ground Station
COTS	Commercial Off the Shelf
RPi	Raspberry Pi
DSP	Digital Signal Processing
NDSA	Normalized Differential Spectral Attenuation
APC	Antenna Phase Center
ECEF	Earth-Fixed Coordinate System
USRP	Universal Software Radio Peripheral
RF	Radio Frequency
GPU	Graphics Processing Unit
FPGA	Field Programmable Gate Array
GPP	General Purpose Processor
LNA	Low Noise Amplifier
ADC	Analog-to-Digital Converter
BPF	Band-Pass Filter

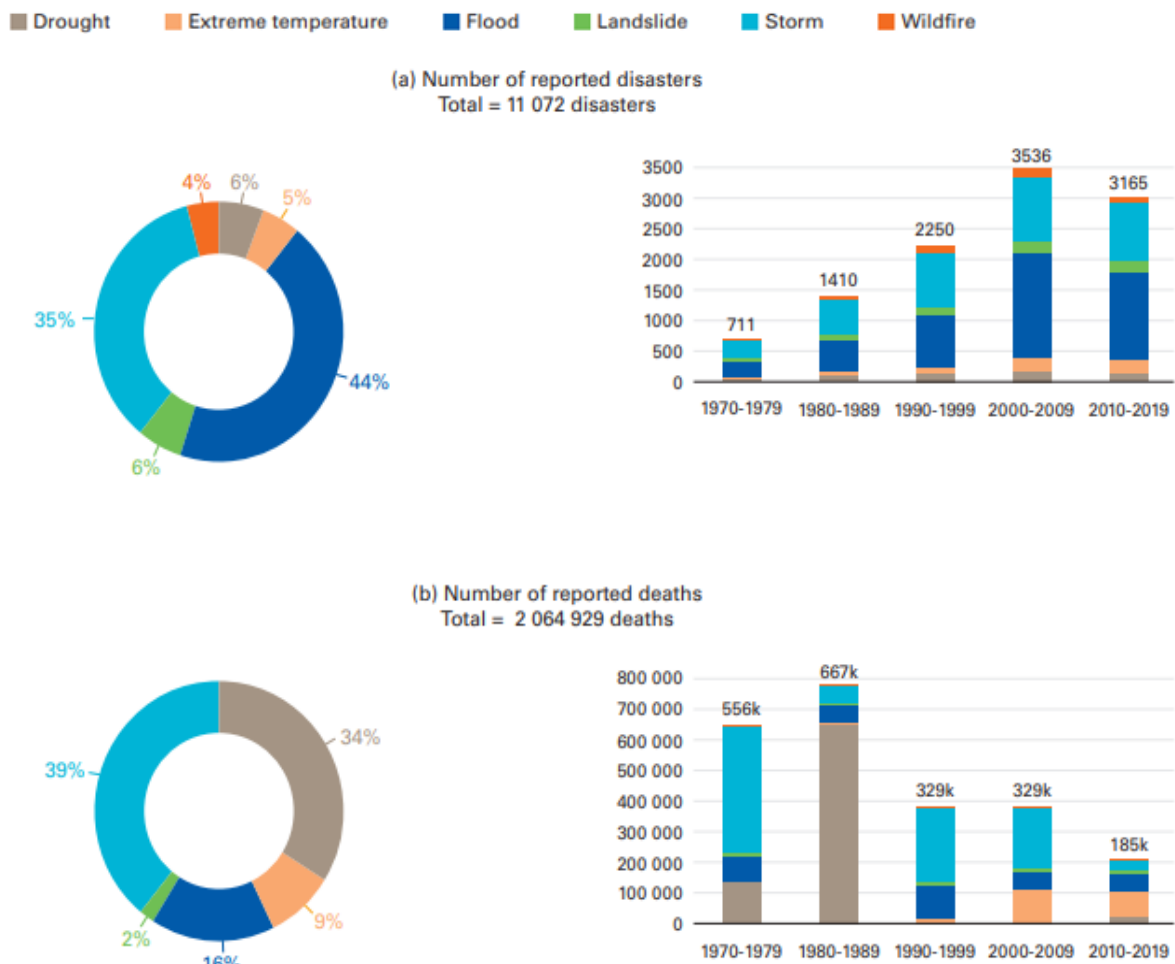
DAC	Digital-to-Analog Converter
DUC	Digital Up Conversion
DDP	Digital Down Conversion
RAM	Random Access Memory
UHD	USRP Hard Drives
RFNoC	Radio Frequency Network on Chip
GRC	GNU Radio Companion
UART	Universal Asynchronous Receiver-Transmitter
UTC	Coordinated Universal Time
GaS	Ground Station and Satellite Network
OBC	Onboard Computer
EPS	Electrical Power System
DIO	digital inputs/outputs
GPL	General Public License
TNC	Terminal Node Controller
SG	Signal Generator
PPS	Pulse Per Second
FSOC	Free Space Optical Communication
GRACE-FO	Gravity Recovery and Climate Experiment Follow-On
COSMIC	Constellation Observing System for Meteorology, Ionosphere & Climate
LAGEOS	Laser Geodynamics Satellite
ALADIN	Atmospheric Laser Doppler Instrument
PC	Personal Computer
AGC	Automatic Gain Controller
AMC	Adaptive Modulation and Coding
FHSS	Frequency-Hopping Spread Spectrum
DSA	Dynamic Spectrum Access
HTPPS	Hypertext Transfer Protocol Secure
IDE	Integrated Development Environment
EIRP	Equivalent Isotropic Radiated Power

# CHAPTER 1

## INTRODUCTION

### 1.1 Overview

The atmospheric water vapor content (TWVC) is a critical meteorological measurand for the hydrological cycle, weather forecasting, climate modeling, Earth's energy budget, and ozone chemistry [1,2]. Recently, the unprecedented global climate change crisis due to TWVC has been evidenced by frequent and intense disruptive weather patterns such as catastrophic floods, extreme droughts, heatwaves, rising sea levels, massive snowfalls, storms, and stronger hurricanes [3,4]. As shown in Figure 1, for the past five decades, the severity and impacts of some of the aforementioned disasters led to huge loss of lives, infrastructure, global economies, businesses, and natural ecosystems on Earth [5–7].





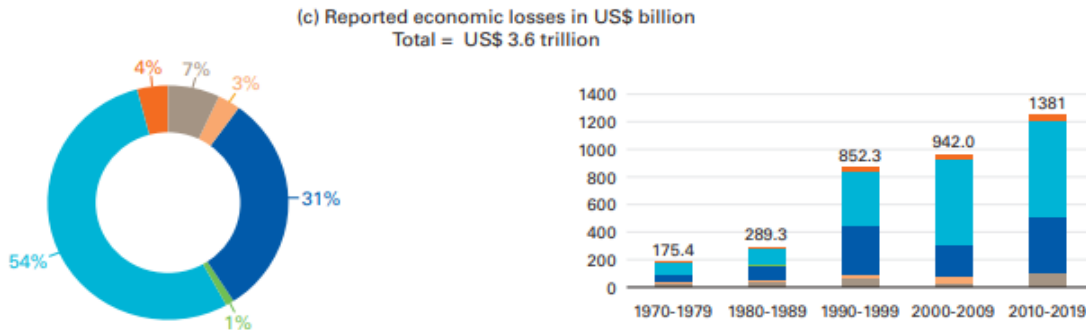


Figure 1. Depicts the global distribution of (a) catastrophes, (b) mortality, and (c) economic losses by hazard category and decade. Source: World Meteorological Organization[8]

Over the next decade, the devastating impacts due to climate change as a result of TWVC are predicted to plunge 130 million people into poverty, unravelling hard won development gains, and by 2050 could force migration of over 200 million people [8]. Taking immediate actions to combat TWVC driven climate changes and its effects is therefore critical to save lives and livelihoods, as well as making the 2030 Agenda for sustainable development goals (SDGs) and its goal number 13 on Climate Action a reality [6]. These problems demand the creation of accurate, reliable, resilient, and adaptative remote sensing techniques that predict, monitor, and mitigate the occurrence of these events with sufficient temporal resolution and spatial coverage for climate risk management and control as illustrated in Figure 2.

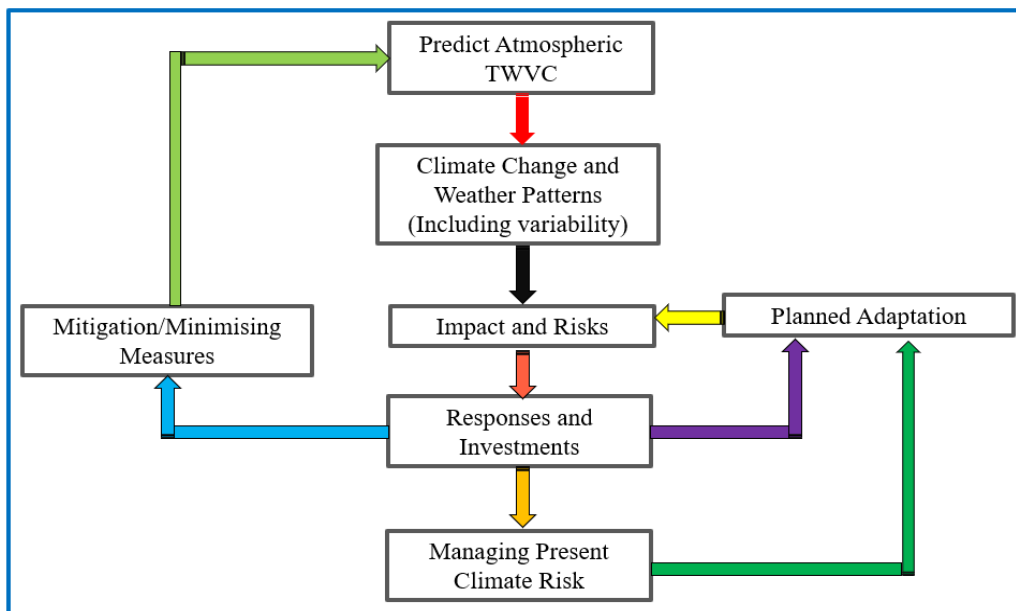


Figure 2. Climate risk management and adaptation framework

Close monitoring of TWVC and related hazards aids disaster relief operations by allowing

early detection of events, recognition of their scope, and reduction of overall damage by responding quickly and effectively. The techniques must provide invaluable TWVC data needed to develop scientific solutions, and make informed decisions that combat climate change and the resulting adverse and extreme weather patterns.

## 1.2 Problem Statement

Conventional ground, air, and space technologies are being used to predict, monitor and measure TWVC distribution as shown in Figure 3.

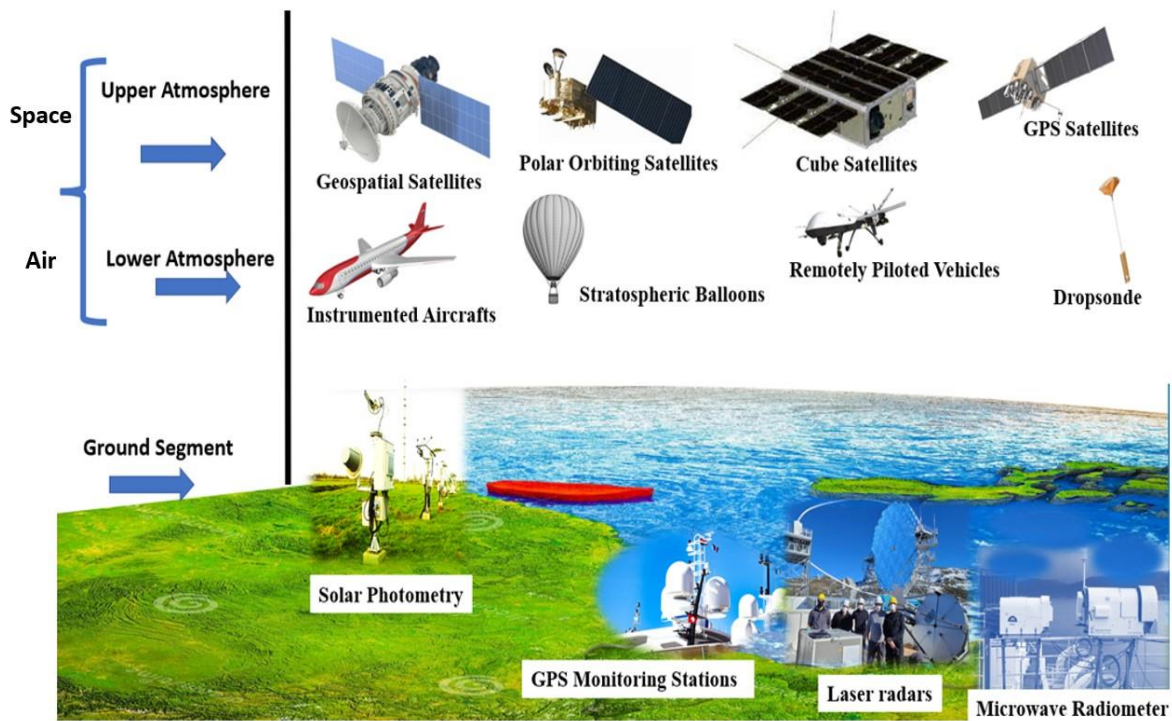


Figure 3. Atmospheric water vapor measurement techniques

Terrestrial remote sensing techniques that use ground or upward-looking observation infrastructure such as surface meteorology, Raman light detection and ranging instruments (R Lidar), microwave radiometry, differential absorption Lidar, and Sun photometers have proven successful in mapping the TWVC distribution with high temporal resolution and adequate precision [2,9–15]. However, these techniques are usually immovable, costly, require continuous maintenance, and have small spatial coverage. Also, surface meteorology related data is closely tied to land-air and cannot sufficiently map the complete boundary of atmospheric water vapor. Moreover, meteorological sensors on microwaves, Lidar instruments and Sun photometers are

greatly affected by rain, clouds, and intensity of sun, respectively. These effects greatly limit the efficiency and effectiveness of using these techniques in measuring parameters of the atmosphere. Very-long baseline interferometry is another ground-based technique that can detect atmospheric water vapor based on the delay of radio signal when observing extragalactic radio emitters such as quasars using a minimum of two terrestrial radio antennas [16,17]. Nevertheless, it is usually characterized with low temporal resolution depending on operation schedule.

Meteorological station data from 1966 to 2017 and ERA5 reanalysis data from 1979 to 2020 over Russia were used to study the incremental correlation between land-air temperatures and extreme daily precipitations as represented by the Clausius-Clapeyron (C-C) equation[18]. Northern Eurasia has not been adequately examined, despite major temperature shifts and a rapid transition from large-scale to convective precipitation. Reanalysis data might have inconsistencies and station data might have limited spatial coverage, especially in remote regions, potentially leading to spatial bias. Gaining insight into the mechanisms driving intense precipitation, necessitates improved weather predictions and climate projections that rely on enhanced satellite technologies for improved accuracy.

Polar orbiting satellites, radiosondes, interferometric synthetic aperture radar (In-SAR), imaging spectroradiometers such as the moderate and medium resolution imaging (MODIS onboard Terra and Aqua and MERIS onboard ENVISAT), remotely piloted vehicles, instrumented aircrafts, and global navigation satellite systems (GNSS) satellites are among the air and space-inclined techniques utilized to detect and measure TWVC [2,19–27]. These methods proved to be convenient and have large spatial resolutions; however, the space measurement technologies have low temporal resolution and compromised accuracy compared to ground-based methods. Furthermore, the use of imaging spectroradiometers (MERIS and MODIS) is affected by clouds in addition to their low temporal resolutions [27].

Two distinct Iranian regions with diverse climate conditions were explored to investigate the impact of shifts in meteorological indicators such as water vapor and temperature on groundwater reserves [28]. The application of Sentinel-1A acquisitions, InSAR technique, and advanced integration methods were implemented to determine meteorological indicators. General circulation models, meteorological data, synoptic observations, and the statistical downscaling models (SDSM) were all used to project the indicators. The prediction of groundwater levels was accomplished through a combination of groundwater level observations, water vapor data derived

from GPS estimations, and an evapotranspiration index relying on an artificial neural network (ANN) [28]. However, the ANN model's accuracy and reliability strongly rely on the quantity and quality of accessible data. Also, inadequate or inconsistent geodetic measurements and groundwater level data may further affect the analysis's robustness.

Optimal approaches that enhance downscaling process from the function-based tomography technique sourced from GNSS satellites was suggested [29]. The dependency on GNSS data and the related hardware infrastructure is one possible downside of adopting the function-based troposphere tomography approach for effective precipitation downscaling. This reliance on GNSS signals could pose challenges in areas prone to signal interference or regions with limited or disrupted satellite signal reception, such as densely forested regions, and urban canyons. The precision and reliability of the tomography approach may be affected in such areas, resulting in inaccuracies in the downscaling process.

Hussein et al [30] utilized copulas functions to depict the seasonal dependency of precipitation and temperature. Whilst they managed to capture the statistical dependency, they could not completely account for the complex physical mechanisms that drive these interactions in the atmosphere. Furthermore, copulas frequently assume stationarity, which implies that the interactions between variables remain constant across time. In reality, climate change and other variables might cause non-stationarity, this could impact risk prediction accuracy.

Geostationary (GEO) satellites like the geostationary operational environmental satellites (GOES) have been vital in effectively monitoring and tracking severe weather environments like storms and hurricanes in real time due to their high temporal resolution and ability to repeat observations over a specific area [31]. Nevertheless, for detecting water vapor, their high orbital attitudes contain large amounts of plasma. Additionally, the spatiotemporal interpolation methods used to derive water vapor from GEO satellites are computationally demanding, requires sophisticated algorithms, and likely biased by data anomalies [31].

Small satellites technologies such as CubeSats are also increasingly gaining relevance in climate and meteorology studies [32]. As part of space precision atomic-clock timing utility mission (SPATIUM), Kyushu Institute of technology (Kyutech) launched and successfully operated two low Earth orbit (LEO) satellites, which are SPATIUM-I (2U CubeSat), and SPATIUM-II (1U payload on a 6U CubeSat), for technology demonstration towards ionospheric electron density mapping [24,33,34]. Even though SPATIUM mission has an objective of three-

dimensional (3D) ionospheric mapping for TEC by a constellation of small satellites, SPATIUM I and II missions demonstrated technologies related to chip-scale atomic clock and onboard processing capabilities to receive and demodulate spread spectrum (SS) signal for time delay measurements between a satellite receiver and the ground stations (GS). As a result, two satellites have not investigated the influence of TWVC on the time delay measurements, 3D mapping of the atmospheric parameters, and employing an orbital constellation in addition to the intersatellite communication yet.

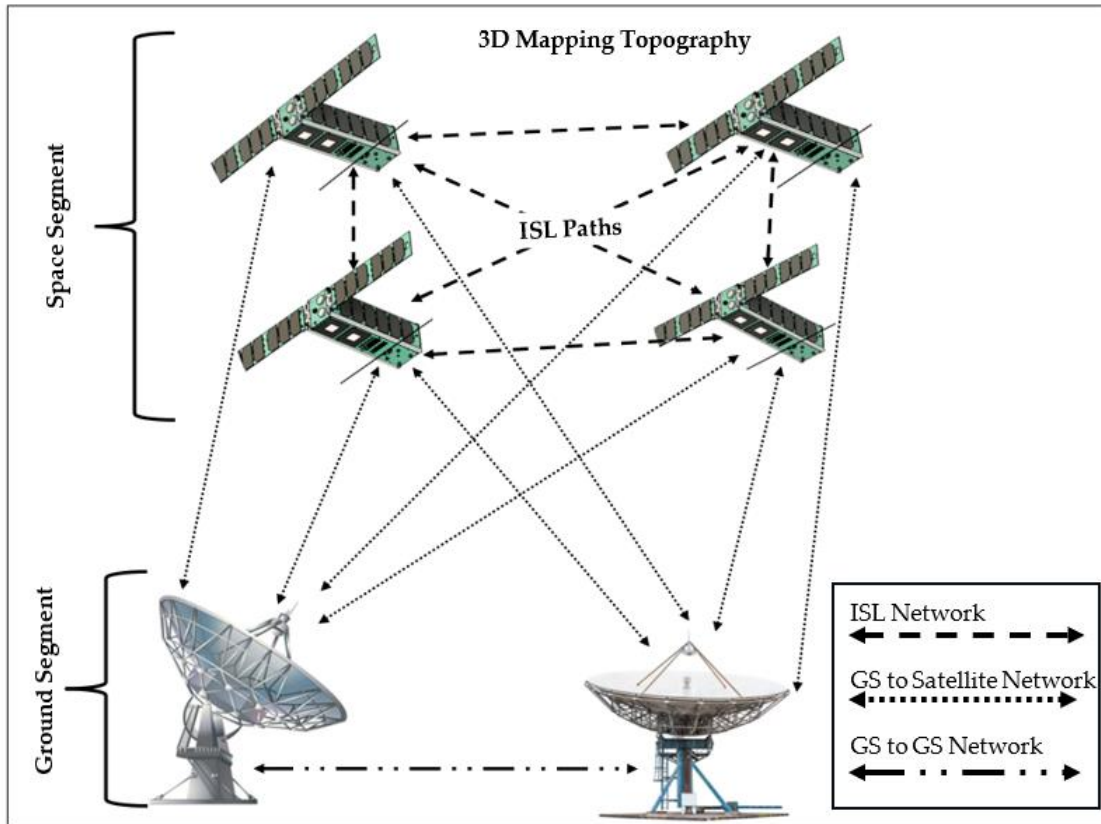
On a global scale, GNSS satellites have carried out modeling and mapping of the atmosphere's geophysical parameters, such as TWVC, TEC, temperature and pressure [35]. The GNSS constellation utilizes either the carrier phase or the pseudo-range radio occultation (RO) techniques to estimate the signal delay as a result of the mentioned geophysical parameters. The measurements are deduced along the GNSS signal array paths [14,20,36]. Models such as numerical weather prediction (NWP) models, global ionospheric models (GIM) and global circulation models were developed to map and model the vertical and horizontal profiles of the atmospheric parameters from GNSS satellites [37–39]. However, the precision of TWVC and TEC from GNSS carrier waves is compromised because GNSS higher L-band frequencies ( $L_1 = 1570$  MHz and  $L_2 = 1220$  MHz) are less affected by the atmospheric geophysical parameters. GNSS satellite were not developed to monitor water vapor distribution or electron density but rather for locating or timing purposes. Therefore, their precision in determining TWVC or TEC is limited. Like GEO satellites, GNSS high orbital altitudes have strong plasma contribution which influences measurement accuracy [24,40]. Furthermore, when estimating water vapor time delay using GNSS technique, the satellites antenna phase center (APC) is prone to fluctuations and they require correct APC modelling. Incorrect APC modeling could yield to false and extra trends in TWVC profiles [41]. Furthermore, GNSS satellites can assess atmospheric water vapor with spatial resolution that fluctuates within the range of tens of kilometers. This spatial resolution is contingent on factors such as the quantity of receiving stations and the revisit period, which can span from seconds to an hour [16]. Therefore, improving the accuracy and spatiotemporal resolutions still remains as an essential task for the measurements of TWVC in addition to the TEC.

### 1.3 Motivation, Challenges and Research Questions

Lower orbital altitude performs better for obtaining higher accuracy, temporal and spatial resolutions of TWVC measurement from satellite signal. Furthermore, lower frequencies than GNSS L-Band are more impacted by atmospheric TWVC and ionospheric TEC and these measurements can be acquired reliably and with better quality. This became the primary motive for this research.

Detecting atmospheric water vapor using low frequency radio signals from a constellation of LEO small satellites is proposed as an alternative method. Radio signals through space are primarily influenced by atmospheric water vapor content and total electron density. Approximately 99% of TWVC is in the troposphere, whereas TEC plasma density is dominant in the ionosphere [42]. Troposphere is a layer in the atmosphere's neutrosphere region. TWVC and TEC profiles could be acquired by a satellite constellation with high spatiotemporal resolutions and better accuracy than the GNSS and other conventional technologies. As a result, small satellites could be considered due to their short development span, affordable costs, and effectiveness in solving space scientific missions. Unlike SPATIUM-I and SPATIUM-II missions, the influence of both TWVC and TEC are taken into consideration and TWVC is separated from TEC. SS ranging signals which allow multiple signals to share the same frequency are transmitted from a network of satellites using intersatellite link (ISL) communication [24]. Software defined radio (SDR) technology has been adopted to transmit and receive the SS signals. SDR technology is significantly effective in that communication digital signal processing (DSP) hardware can be implemented as software, it supports a wide range of radio frequencies, and its architecture is reconfigurable, extensible, reprogrammable, and upgradable in real time [43]. The SS signals are modulated with binary phase shift keying (SS-BPSK) modulation because BPSK-modulated data travels long distances, and the original message is easily detected at the receiver due to the efficient properties of BPSK technology [44]. ISL technology has been employed for various satellite communication and formation flight applications, enabling ranging, commanding, timing control, and data transfer in a distributed network system [45]. In this proposal, the intersatellite ranging from satellites in different LEO orbital planes is performed in all directions to acquire three-dimensional mapping of atmospheric water vapor and ionospheric density along each line of transmission. Each satellite in the ISL network has a mission payload for TWVC derivation. The mission payload is designed to fit small satellites limited constraints of power, mass, and size. To derive the water vapor and

electron density three-dimensional distributions, we solve the inverse problems [24]. For a given set of water vapor and electron density distribution, we integrate the two quantities along each measurement path and compare TWVC and TEC with the ones derived from the measurement. We find the 3D water vapor and electron density distribution that best matches with the measurement. Figure 4 depicts the main notion of water vapor and electron density dispersion measured from a constellation of satellites.



*Figure 4. 3D Mapping of atmospheric TWVC*

The TWVC and TEC are detected based on signal propagation time delay, and the delay of SS signals along the intersatellite ranging path is calculated onboard each satellite. Since the total electron density varies inversely to the square of the radio signal frequencies, whereas TWVC does not, solving the inverse problem and manipulating multiple radio frequencies (RF) help to distinguish and separate TWVC from TEC [46]. Two remotely tuned algorithms that utilize extensible markup language remote procedure call (XML-RPC) and transport control protocol/internet protocol (TCP/IP) were coded to remotely reconfigure SDR transmitter and receiver frequencies in real time [47,48]. The algorithms were built using GNU Radio digital

processing blocks and the Python programming language. The algorithms achieve frequency translation within a second of reconfiguration. This is the shortest possible time to retrieve the mission data with high accuracy based on this method. Meteorological ultra-high frequency (UHF) bands were selected for communication since they are more vulnerable and influenced by the parameters of the atmosphere compared to GNSS L-band frequencies. The network of ground stations (GS to GS network) uses GS to satellite networks to operate missions, control the satellites, and acquire mission data from satellites in the ISL network. However, there are technological hurdles and research questions that must be addressed in the development of this technology which are:

1. Determining the TWVC measurement and calculation concept based on a constellation of small satellites using radio signals. The concept mathematical modelling should take into consideration all the parameters and assumptions that deduce the TWVC with very high accuracy.
2. Deducing TWVC measurement is based on time delay. However, on ground test there is no influence of TWVC not TEC. Therefore, a method that simulate atmospheric water should be implemented to demonstrate the feasibility of mission success in orbit.
3. Implementing a robust ISL network on a constellation of CubeSats. The ISL architecture is required to fit within the limited constraints of Kyutech based satellite architectures. In line with Kyutech projects incorporation of an ISL network has not been implemented. Moreover, laser-based systems have been so much implemented in kind of a mother and daughter satellite architecture, however no clear demonstration has been given using RF signals [49].
4. The most viable choice for the transceiver in both the satellite and ground station for SS transmission and reception is the commercially available SDR. This is because the SDR architecture supports remote reconfiguration of radio communication parameters. Also, SDR are scalable, upgradable, can be updated over time and they operate on a wider frequency bands and bandwidth. However, they have time offset errors which distort the accuracy of data.
5. To distinguish atmospheric water vapor from total electron content, frequency manipulation algorithms are required to remotely tune the SDR frequency parameters. Python and c++ based GNU Radio software has been proven the best method to



implemented the software transceiver that controls and tune the SDR. However, GNU Radio software parameters including the SDR radio frequency parameters are not easily accessed for tuning frequency outside the GNU Radio itself. Also, the reconfiguration algorithms if implemented they must achieve the frequency translation in the shortest possible time to attain accuracy.

6. To attain maximum performance of the TWVC mission system, onboard processing of TWVC data shall be done. The onboard processing time depends the microcontroller processing capacity and efficiency of the algorithms. High speed processing is required for system optimization, efficiency in processing, transmission and reception of SS signals. Processor choice and efficiency of processing algorithms is of paramount importance.
7. Can the mission success be achieved on the implementation based on SDR technology, on small satellite and using commercial off the shelf components (COTS).

This thesis will discuss the likely best approach for deducing atmospheric water while addressing all the challenges and unproven research questions present.

#### **1.4 Research Aim**

To invent space technology solutions that support atmospheric geophysical databases with water vapor data for

1. Accurate TWVC in orbit prediction,
2. Trend analysis of TWVC distribution in orbit over time,
3. Disaster and emergence preparedness
4. Insurance estimations
5. Informed decisions on climate and weather changes.

#### **1.5 Research Objectives**

The main objectives of this research encompass:

1. To deduce the TWVC measurement concept.
2. To design a satellite payload that measures atmospheric water vapor, determines the system requirements, selects the components and specifications, and conducts system interfaces and integration.
3. To implement a GNU radio-based SDR transceiver with both transmitting and receiving

- capabilities of SS ranging signals.
4. To perform ISL ranging. This is essential for 3D mapping when all LEO orbital planes will be considered.
  5. To demonstrate dual frequency reconfiguration of SS ranging signals by remotely tuning SDR parameters during runtime onboard each satellite. This is required for mission measurement accuracy and to distinguish TWVC and TEC.
  6. To eliminate instruments' clock offsets and errors as much as possible.
  7. To simulate how the signal time delay due to water vapor and electron density can be estimated. This is vital in deducing the final TWVC measurement.

## 1.6 Mission Requirements

The most critical requirements of this study are listed below:

- The frequency reconfiguration time and data processing time should be  $\leq 1$  s.
- A water vapor column of approximately a few mm and a delay measurement accuracy  $\leq 100$  ns.
- The size of the constellation should be more than 1000 small satellites [24].
- The temporal resolution should be between 5 min and 15 min, whereas spatial coverage should be between 15 km and 4600 km.
- The payload should be able to fit within the limited constraints of power, size, and mass for a small satellite.

## 1.7 Research Scope

The research was conducted in parallel to Kyutech satellite development projects where I earned a lot of skills to develop the TWVC mission concept and implementation. The scope of this thesis will include the mission concept design, selection of mission components, system design configuration for mission and bus subsystems, programming, hardware and software integration, testing and validation. The TWVC measurement concept and separating TWVC from TEC based on radio signals with the use of SDR technology shall be addressed. The scientific research on atmospheric radio sensing gives a comprehensive grasp on determination of the TWVC estimations and the fluctuations in atmospheric water vapor profiles. The hardware section of this study involves the integration of the SDR as the transceiver, Raspberry Pi (RPi) for processing,

GPS modules for clock accuracy and time reference, radio frequency (RF) switch for time stamping of the incoming and outgoing signals, delay pulse generator for delay simulation, antennas for electromagnetic radiation transmission and reception, and power bus. These hardware components are mounted on each satellite in the ISL network. Other hardware such as power meter, oscilloscope, RF shield box, current probe, spectrum analyzers, and power supplies has been used to support the test requirements. The software was mainly implemented utilizing Python programming and GNU Radio DSP software. The software was implemented to emulate DSP hardware functions, to control the SDR and to manipulate frequencies. The software was also made to do onboard processing of the mission data based on time delay.

### 1.8 Research Methodology

This research was conducted following several phases of implementation required to achieve the mission success. The milestones have been implemented in detail achieve the desired goal of TWVC measurement. The methodology was simplified as shown in Figure 5.

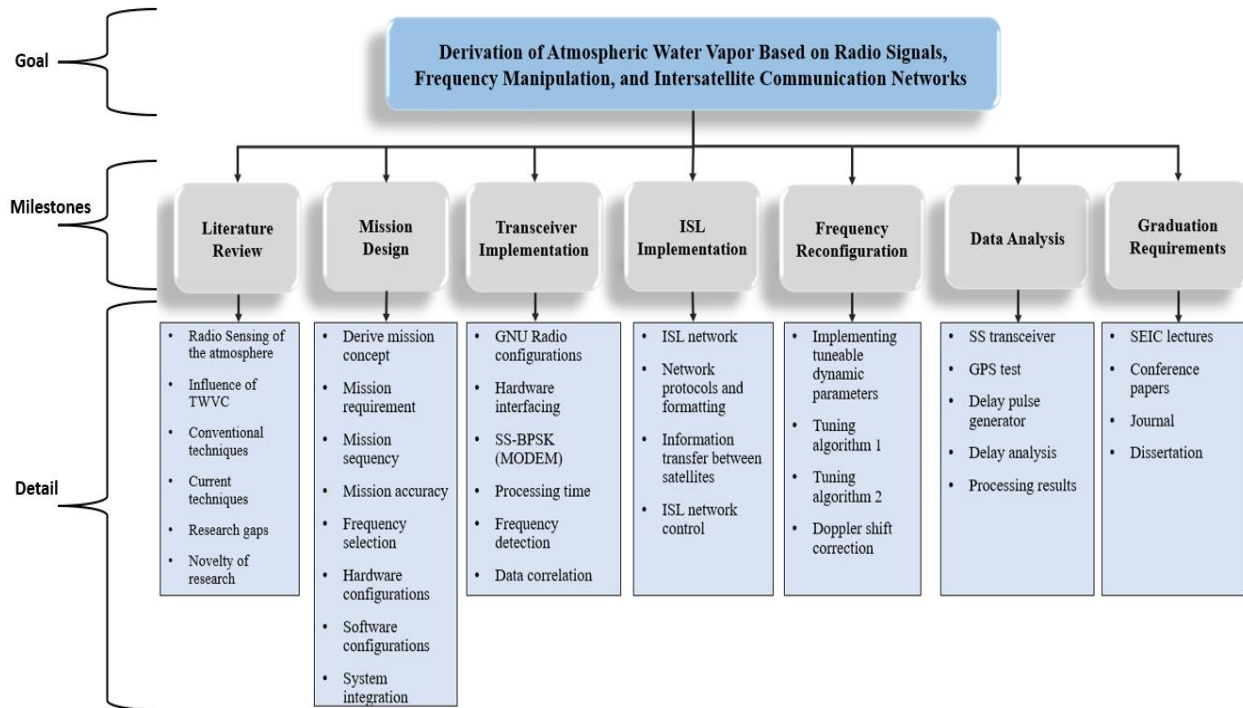


Figure 5. Atmospheric water vapor implementation methodology

1. **Literature Review:** An intense literature review was performed to comprehend the science of the atmosphere, variation of atmospheric geophysical parameters, and the influence of atmospheric water vapor to climate change, communication networks and weather patterns.

From the literature review, conventional and current technologies that are being used to predict TWVC were investigated to discover the research gaps and novelty of this research area.

2. **Mission Design:** Derivation of the mission concept, TWVC calculation mathematical modelling, determination of mission requirements and execution were done at this stage. Also, the design configuration at the satellite side and ground station sides were decided in terms of the hardware and software that achieves mission accuracy with better resolutions compared to conventional methods. After all the software and hardware were selected the system integration was conducted and tested.
3. **Transceiver Implementation:** All satellite in the ISL network has the capability to transmit and receive SS ranging signals. An implementation of the transceiver and frequency translation algorithms with GNU Radio was done.
4. **ISL Implementation:** A network of two satellites was implemented to demonstrate the feasibility of being able to exchange information between satellite in an automated fashion. All satellites in the ISL network can also be controlled from a network of ground stations in order to downlink mission data to the ground station
5. **Frequency Reconfiguration Implementation:** Frequency translation algorithms were implemented for mission accuracy. Two robust algorithms implemented in the client and server architecture were implemented. Doppler shift correction was also implemented to improve signal transmission and detection accuracy.
6. **Data Analyses.** Data analyses was done at several stages of the TWVC mission development. Acquisition of GPS location, clock and time reference data was done. The implemented transceiver performances were analyzed using digital and graphical method. Time delay detection and mission data processing was also investigated at this stage.
7. **Graduation Requirements.** All the requirements for doctoral graduation were fulfilled.

## 1.9 Research Novelty and Contribution

The novelty of the present paper is the use of SDR technology to deduce atmospheric water vapor delay based on radio signals, frequency manipulation, and the ISL network from a constellation of small satellites in LEO. Also, time stamps were implemented with RF switches in order to deduce the signal propagation time delay. The SDR capabilities were adopted to

implement an automated software transceiver that performs digital signal processing (DSP) and frequency manipulation remotely in the shortest possible time. Instead of each satellite being composed of several radio devices that operate at different frequencies, only a single SDR transceiver is mounted onboard each satellite to perform the communication mission requirements and this reduces the cost and strain on the limited resources of small satellites. In this way, the size of individual satellites becomes smaller and the number of satellites in the constellation can be increased. In the present paper, we propose a constellation of small satellites to carry out 3D mapping of ionosphere and troposphere with improved spatiotemporal resolutions on the condition that the satellite constellation is large enough to cover a wider area. Moreover, the feasibility of ISL ranging based on a low-cost commercial off-the-shelf (COTS) SDR transceiver and RPi microcomputer is uniquely demonstrated.

The ultimate goal of this study is to contribute to the advancements of climate and scientific studies of the atmosphere concerned with the influence of atmospheric water vapor and total electron content. In fact, prediction of TWVC assists in understanding the risks and impact of climate change and weather patterns so that mitigation and adaptation measures can be completed to safeguard life on Earth. The TWVC data acquired will be vital in the development of advanced climate and weather prediction models. Moreover, to a certain extent, this study finds its use in space communication and SDR technology applications

### **1.10 Dissertation Organization**

This thesis is partitioned into five major sections. The first section (Chapter 1) introduces an outline on the climatology of the atmosphere. Statistical information on the destructive calamities as a result of atmospheric water vapor has been given. After that research aim, and problem statement was given based on the conventional and current measurement techniques and models of water vapor. The implementation of this mission is still work in progress and several developments needs to be implemented to optimize the system performance to achieve the best results. Research motivation, challenges, research questions, objectives, scope and methodology were discussed in detail. In Chapter 2, a survey of the literature on the science of space weather conditions, traditional and modern TWVC measuring techniques, and their comparisons is provided. This chapter also summarizes Kyutech projects related to this research. Chapter 3 details the mission measurement concept and proposed method mission design configurations. Chapter 4

detail all the implementations and results obtained. All the challenges on the system and how they are addressed is discussed in this section. In Chapter 5, conclude this research, provides future studies and discussion. An appendix section with all the codes implemented is provided.

## CHAPTER 2

### LITERATURE REVIEW

#### 2.1 Overview

The literature review or the foundation for this research is detailed in this chapter. An overview of atmospheric water vapor composition and the impact it poses on catastrophic atmospheric weather events will be explained. The theoretical fundamental is composed of numerous themes and subthemes that support the core notion of TWVC measurements. The chapter proceeds with analyses of many related published studies on TWVC, and comparisons between the findings of these researches are given. The author will give a deep insight into GNSS signal analysis. Other radio sensing technologies for atmospheric water vapor will be discussed as well, as the approaches may complement one another. Conceptualization, application of the methodology, evaluation of each processed data set, drawbacks, and suggestions for improvement are all aspects of the measurement of the TWVC that may be achieved.

#### 2.2 Atmospheric Water Vapor and Impact of Climate Change

##### 2.2.1 Contribution of Atmospheric Water Vapor to Greenhouse Effects

Every planet in the solar system, as well as other celestial objects, including comets and even huge asteroids, contain water vapor, making it a common atmospheric component. Considering the Earth's atmosphere, WV stands out as the dominant greenhouse gas that extends up to 30km above the earth's surface, contributing to more than 95 percent of the current greenhouse gases and at most 4 percent of the atmospheric air, as shown in Figure 6 [50,51] . Since most of our weather events occur within the first 10 to 15 kilometers (km), water vapor has a significant impact on climate change and weather patterns.

Water consumption for aviation, agriculture, domestic use, and power plant cooling all contribute to human activity-related water vapor emissions. Such emissions result in an increase in atmospheric humidity and the greenhouse effect of water vapor, and they also have an impact on cloud cover, which might either raise or decrease the emissions' "direct" effect. Although anthropogenic water vapor emissions are not typically thought of as a significant climate forcing

factor since they are minor relative to ocean evaporation, they are considerable compared to emissions of other greenhouse gases like carbon dioxide (CO<sub>2</sub>).

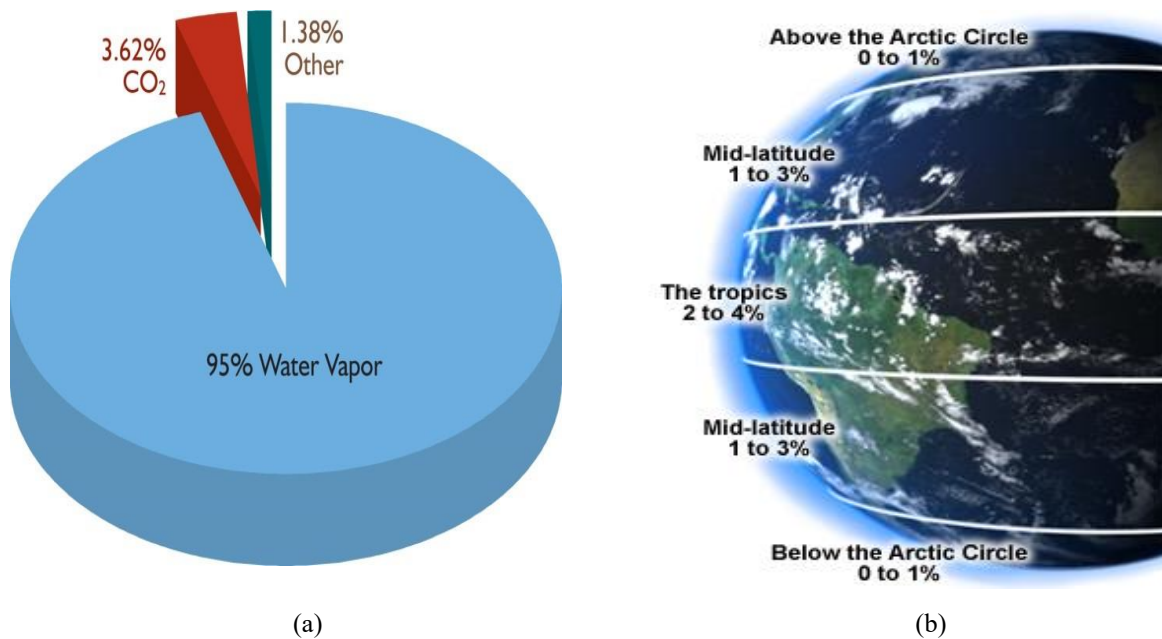


Figure 6. Percentage of atmospheric water vapor to (a) Greenhouse gases (b) The troposphere

Increased TWVC increases the warmth induced by other greenhouse gases. The mechanics underlying a positive and negative water vapor feedback loop [52] are depicted in Figure 7.

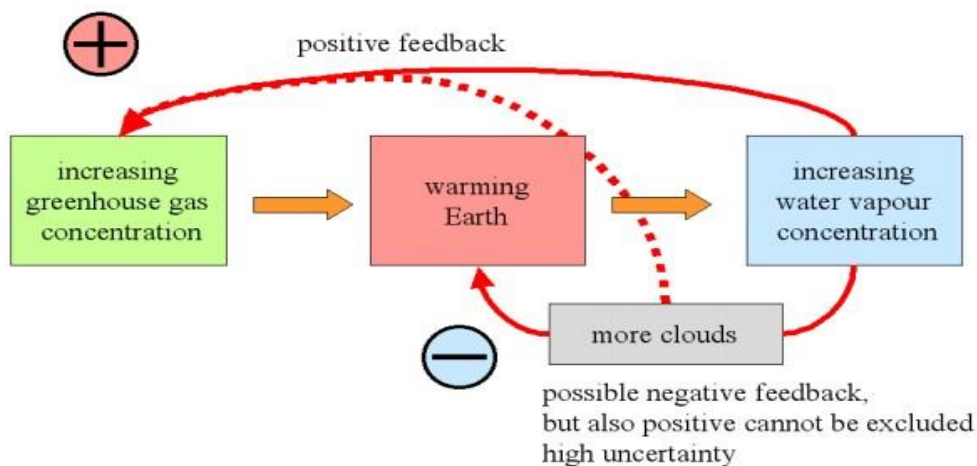


Figure 7. Positive and negative contribution of TWVC to greenhouse gases

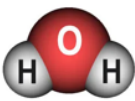
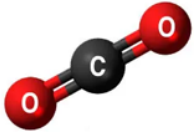

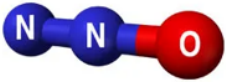
The sensitivity of the Earth's climate system is mostly governed by feedback loops or processes. Within the system, feedbacks occur that can either dampen or increase the reaction to external influences impacting the climate. In other words, the effect of one process produces



changes in another, which then influence the first. Positive feedback increases the direct impacts of the initial process, whereas negative feedback decreases them.

In the positive loop, Earth's temperature rises in reaction to an increase in greenhouse gases. This causes more evaporation from land and water surfaces. Warmer air has a higher moisture content; hence, it has more water vapor in it. This occurs because at higher temperatures, water vapor does not condense and precipitate out of the atmosphere as readily. The heat from the Earth is then absorbed by the water vapor, preventing it from escaping into space. As a result, the atmosphere becomes even warmer and contains even more water vapor. of the climate, such as sea levels, rainfall patterns, ocean and surface air temperatures. As shown in Table 1, unlike other greenhouse gases like nitrous oxide, carbon dioxide, and methane, water vapor does not stay longer in the atmosphere; therefore, it causes short-term but devastating impacts on climate changes and weather patterns.

*Table 1. Comparison of greenhouse gases [53].*

	<b>Water</b>	<b>Carbon Dioxide</b>	<b>Methane</b>	<b>Nitrous Oxide</b>
<b>Symbol</b>				
<b>Atmospheric Concentration</b>	0.01-4%	385 ppm	1797 ppb	322ppb
<b>Rate of Increase</b>	variable	1.5 ppm/year	7.0 ppb/year	0.8 ppb/year
<b>Atmospheric life time</b>	1-5 days	5-200 year	12 year	120 year

Within the negative feedback loop, the water vapor in the atmosphere will undergo condensation, leading to the formation of clouds. Clouds can have a dual impact on the greenhouse effect, as they might intensify it by trapping heat within the atmosphere or reduce it by reflecting solar radiation back into space. Depending on where the clouds grow, they can either warm or cool the environment, further complicating matters. High-level clouds tend to trap heat, hence boosting warming. Cloud formation at low altitudes has a cooling impact, offsetting some of the heat.

## **2.2.2 Resultant Disruptive Weather Patterns and Climate Changes**

Water vapor related climate change threatens water resources, agriculture, human health, forests, animals, and coastal regions. For instance, [5,7]:

1. Warmer temperatures are predicted to raise the risk of heat-related diseases and fatalities, as well as some forms of air pollution.
2. Sea level rise has the potential to degrade and inundate coastal habitats as well as remove wetlands.
3. Climate change has the potential to drastically alter present ecosystems by changing where species dwell and how they interact.
4. Warmer climate is projected to bring more severe disasters including:
  - i. More rain and flooding: Storms can create more severe rainfall events in some regions due to increased evaporation since there is more water in the air. The global water cycle is also accelerated by increases in atmospheric water vapor. They help to make wet areas wetter and dry areas dryer. The more water vapor there is in the air, the more energy it contains. This energy feeds violent storms, especially over land.
  - ii. More extreme drought: As a result of increased evaporation brought on by warmer temperatures, some parts of the world experience drought. Over the next century, it is predicted that drought-prone areas will get progressively drier. Farmers might expect fewer crops in these circumstances, which is unfavorable news for them.
  - iii. Stronger hurricanes: Warmer Ocean surface waters have the potential to strengthen hurricanes and tropical storms, making landfalls more dangerous. The frequency of storms will increase due to climate change.
  - iv. Heat waves: Heat waves have probably become more frequent in more parts of the planet.

## **2.3 Measurement of Atmospheric Water Vapor and Total Electron Content**

### **2.3.1 The Normalized Differential Spectral Attenuation (NDSA)**

Theoretically, a unique measurement concept for monitoring the vertical distribution of tropospheric WV has been validated, and presently being developed for space deployment [54].

The NDSA approach utilizes a linear relationship between spectral sensitivity ( $S$ ) and integrated water vapor (IWW) to calculate IWW along the radio link using data from two low Earth orbiting satellites. One of the satellites was mounted with a receiver and the other one with a transmitter [54]. The NDSA method converts  $S$  measured along the way from a transmitter to a receiver into the appropriate path IWW utilizing predefined  $S$ -IWW linear relationships.

The very significant association between  $S_{f_0}$  and integrated water vapor at distinct tangential altitudes (TAs) for frequency  $f_0$  (17-21) GHz was validated through simulations using an extensive dataset of radiosonde data [54]. The integrated water vapor along a specific microwave link operating at  $f_0$  may be determined mathematically using linear relationships:

$$IWW = a_0 S_{f_0} + b_0 \quad 1$$

Ideal values of  $f_0$  corresponding to various tangent height intervals, as well as the related values of constants  $a_0$  and  $b_0$ , are presented in [55]. The spectral sensitivity corresponding to a specific frequency is computed through approximation of finite differences applied to the attenuation function of the spectral. This function quantifies the total attenuation experienced by a tone signal during its propagation at the mentioned frequency, as expounded in reference[56]. It's worth noting that the setup involved two distinct LEO satellites, with one acting as the transmitter and the other as the receiver. One technique for determining  $S$  at  $f_0$  involves sending two sinusoidal tones with very near channels  $f_1$  and  $f_2$  ( $f_1 \approx f_2$ ), symmetrically arranged around  $f_0$ , which is known as the channel frequency. The powers, denoted as  $P_{w1}$  and  $P_{w2}$  pertaining to the two acquired sinusoids, are determined at the receiver using appropriate filtering, such that the spectral sensitivity associated with  $f_0$  is easily computed as follows:

$$S_{f_0} = \frac{P_{w2} - P_{w1}}{\Delta f P_{w2}} \quad 2$$

where  $\Delta f = f_1 - f_2$  denotes the spectral separation, which should be 200 or 400 MHz. This denotes the standardized scaling ratio of spectral attenuation within the K/Ku dual frequency bands in relation to the gradient of the WV suction line occurring at  $\approx 22.2$  GHz. Inverting a IWW data sequence taken in limb geometry at different tangent heights yields vertical profiles of WV. The focus was placed on the most recent findings derived from the endeavors of the Italian Space Agency SATCROSS project, with special attention to the improvements made to the prototype instrument [56]. These improvements have significantly augmented its operational capabilities, particularly in the aspects of the stability of power and resolutions of time. The SATCROSS project

focuses on implementing the NDSA approach in a scenario involving a series LEO satellites traversing common orbits. These satellites generate sets of integrated water vapor measurements, which can be used to derive two-dimensional WV fields on perpendicular planes to the surface of the Earth. Through this research, it was shown that tropospheric turbulence scintillation can considerably affect water vapor estimations obtained from limb observations between dual low Earth orbit satellites operating within the mentioned frequency band.

### **Limitations**

Two critical issues impacted the trustworthiness of the empirical IWV-S relationships discovered in the NDSA technique: 1) the precision of the radiosonde data used to create them, and therefore their placements, is not consistent in the south and north hemispheres; 2) the quantity of radiosonde samples above 10 km is restricted, and their dependability is rare, affecting the study of the IWV-S relations. The link budget necessitates a shorter distance, not exceeding 400–500 km, between the transmitting and receiving satellites. Similarly, ionizing radiation effects rule out altitudes over 400 km because radiation shielding equipment would overload the CubeSat payload. This implies that TEC considerations were omitted in this mission. The simulation's major purpose has been to minimize the temporal gap between a pair of consecutive satellite traversing over a specific mid-latitude region, at the same time also ensuring consistent spatial resolution; therefore, its temporal resolution is low. Additionally, in terms of the orbital inclination of the two satellites, a sun-synchronous orbit is chosen to cover all latitudes effectively, while also extending the average duration of coverage when contrasted with alternative values of inclination. In order to derive two-dimensional fields, inversion methods were utilized to reconstruct information from sequences of individual integrated water vapor estimations linked between low Earth orbit satellites pairs.

### **2.3.2 The GNSS Concept**

#### **a. Ground Based GNSS Measurement of Water Vapor**

The GNSS RO and ground-based techniques have been conventionally and recently employed to detect atmospheric water vapor [57–59]. The GNSS based GPS approach for monitoring atmospheric water vapor was introduced in early 1992 [60]. Currently, ground-based GNSS technology (see Figure 8), which has tens of thousands of stations globally, provides vital

information regarding water vapor variability. GNSS computation for the parameters of the troposphere have emerged as a crucial data source for applications in climatology and meteorology due to their fundamental characteristics, including year-round functionality, acceptable accuracy, moderate time resolution, and widespread coverage over terrestrial regions [61]

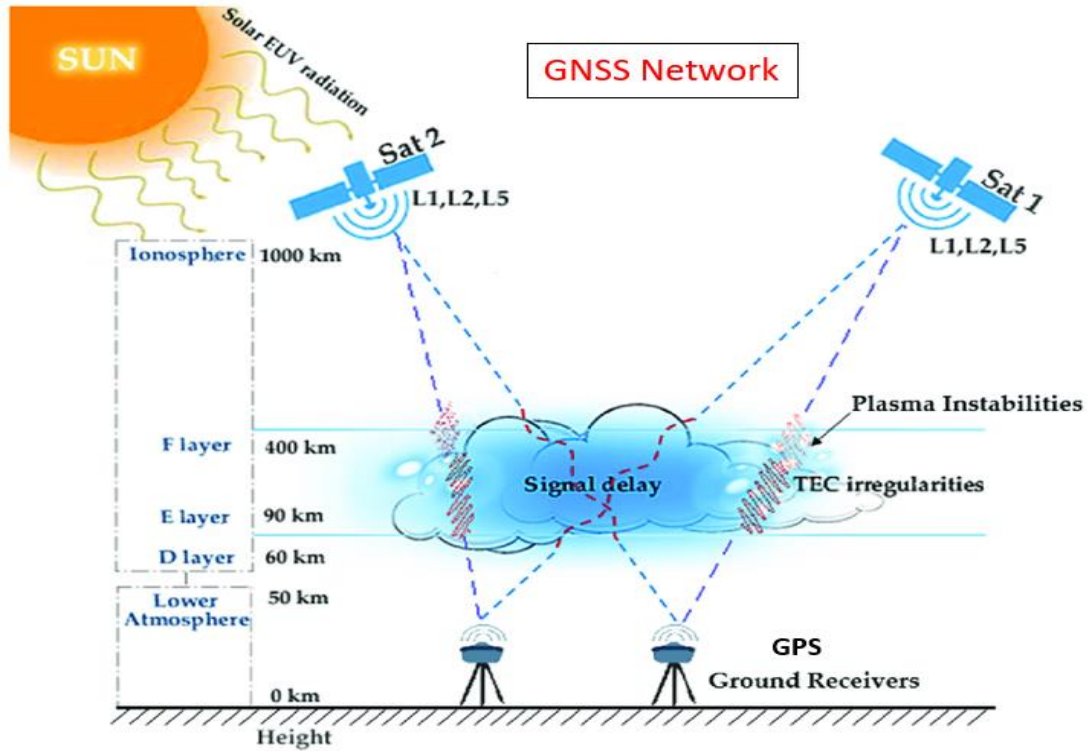


Figure 8. GNSS satellites probing of the troposphere and ionosphere and received with ground-based GPS receiver [62].

The core concept behind remote sensing of WV using GNSS revolves around the observation that the GNSS signal, as it propagates between the satellite and the terrestrial receiver, encounters delay predominantly influenced by the troposphere and ionosphere [63–65]. The GNSS computation for determining the receiver's location must consider slant tropospheric delay (STD). This delay is commonly expressed as a function of zenith tropospheric/total delay (ZTD) because it's independent of specific satellites. Converting STD to ZTD requires the use of mapping functions [66]. The delay is influenced by atmospheric conditions and can be transformed from slant paths at a 90-degree angle to vertical paths using mapping functions, resulting in the ZTD. After the calculation of the ZTD, meteorological data, mainly the surface atmospheric pressure, is utilized to derive the non-dipolar constituent of ZTD, commonly referred to as zenith hydrostatic delay (ZHD). After deducting ZHD from ZTD, the resultant value solely represents the dipolar

component, which is solely attributed to the existence of WV. The WV is the sole atmospheric constituent characterized by a consistent dipolar moment. This residual element is denoted as zenith wet delay (ZWD) and is determined as follows:

$$ZWD = ZTD - ZHD \quad 3$$

A linear correlation exists between precipitable water vapor (PWV) and ZWD shown in Equation 4 [67]:

$$PWV = \Pi \cdot ZWD \quad 4$$

The symbol  $\Pi$  denote the translation factor of precipitable water vapor and zenith wet delay. In a physical context, PWV represents the altitude at which the water vapor within a unit area of the Earth's atmosphere becomes saturated and converts into liquid water through condensation. The symbol  $\Pi$  is dependent on average temperature  $T_m$  of WV:

$$\Pi = \frac{10^6}{\rho_w \cdot \frac{R}{m_w} \cdot \left( \frac{k_3}{T_m} + k_2 - \frac{m_w}{m_d} \cdot k_1 \right)} \quad 5$$

In the equation  $\rho_w$  liquid water density,  $R = 8.314 \text{ kg} \cdot \text{m}^2 \cdot \text{s}^{-2} \cdot \text{K}^{-1} \cdot \text{mol}^{-1}$  stands for the universal gas constant,  $m_d = 28.96 \text{ kg/kmol}$  is the dry atmosphere's molar mass and  $m_w = 18.02 \text{ kg/kmol}$  refers to the TWVC molar mass. Additionally, there are three physical factual constants denoted as  $k_1 = 77.6 \text{ K/hPa}$ ,  $k_2 = 70.4 \text{ K/hPa}$ , and  $k_3 = 3.7 \times 10^5 \text{ K}^2/\text{hPa}$ . Finally,  $T_m$  is a variable associated with temperature and vapor pressure various atmospheric altitudes. In practical terms, the utilization of long-term radiosonde datasets in the analysis of linear regression yields an empirical equation for surface temperature and  $T_m$  [60]. The measurements of tropospheric WV tomography involve integrating the WVC along the path of the ray, referred to as slant water vapor (SWV). Equation 6 elucidate the aforementioned.

$$SWV = \int \rho_l(l) dl = PWV \cdot M_w + R \quad 6$$

where  $\rho_l(l)$  is the water vapor density,  $dl$  is the signal element length,  $M_w$  is the wet mapping coefficient, and  $R$  is the non-uniform changes in WVC, and it is determined as a product of the post-fit residual and factor of conversion.

## Limitations

The ZTD estimations uncertainty, and the quality and availability of pressure ( $P_s$ ) and  $T_m$

data at the GNSS sites, restrict the precision of the IWV retrievals.  $P_s$  and  $T_m$  should ideally be properly determined utilizing radiosondes and co-placed synoptic barometers [57,68]. The uncertainties of IWV obtained from GNSS can approach  $600 \text{ g m}^{-2}$  in this situation [41]. It's important to note that not all GNSS stations are equipped with barometers, and only a few of them are situated in close proximity to radiosondes.

Furthermore, high orbital altitudes do not give enough accuracy to determine WV due to high contribution of plasma. Moreover, GNSS were not developed to monitor atmospheric water vapor distribution but rather for locating or timing purposes; therefore, their precision in determining IWV is compromised. Because GNSS meteorology is a very indirect approach, errors can occur at any stage of the processes. For instance, the presence of patterns in the WV gradient can cause mistakes in GNSS-derived PWV to the point that strategies to adjust for this must be devised. The satellite Antenna Phase Center (APC) fluctuations are also essential when estimating ZTD from GNSS measurements. Correct modeling for APC is needed because incorrect modeling can yield false and extra trends in PWV.

#### **b. Radio Occultation Technique Measurement Water Vapor**

The satellite-based GNSS RO [38,69,70] technique has been developed over the last two decades as a novel remote sensing technique which offers Earth's upper and lower atmosphere's global vertical profiling with numerous applications, including tropospheric, ionospheric, space weather, and climate sciences [71,72]. The GNSS signal can be captured by a LEO spacecraft while it travels in a limb sounding configuration through the troposphere using a GNSS receiver aboard the satellite at an altitude lower than 1000 km. From the perspective of the LEO receiver, the transmitter of the GNSS signal, can attain lower than zero elevation angles, as illustrated in Figure 9. The occurrences of rising and setting occultations are identified by changes in the heights of the signal, resulting in signal bending as the satellite moves relative to the LEO receiver's line of sight. Because of the vertical fluctuation of the air refractive index, the bending strength will fluctuate. The neutrosphere index of refraction is affected by humidity and temperature, whereas the ionospheric one is affected by electron density [36]. The accuracy of GNSS and LEO satellite's location and speed is essential for the assessment of the RO measurements. The ultimate output data from GNSS-RO encompasses profiles of refractivity, temperature, refractivity, and air pressure spanning altitudes of approximately 4000m. Additionally, it provides data on lower

tropospheric WV content and profiles of plasma within the ionosphere.

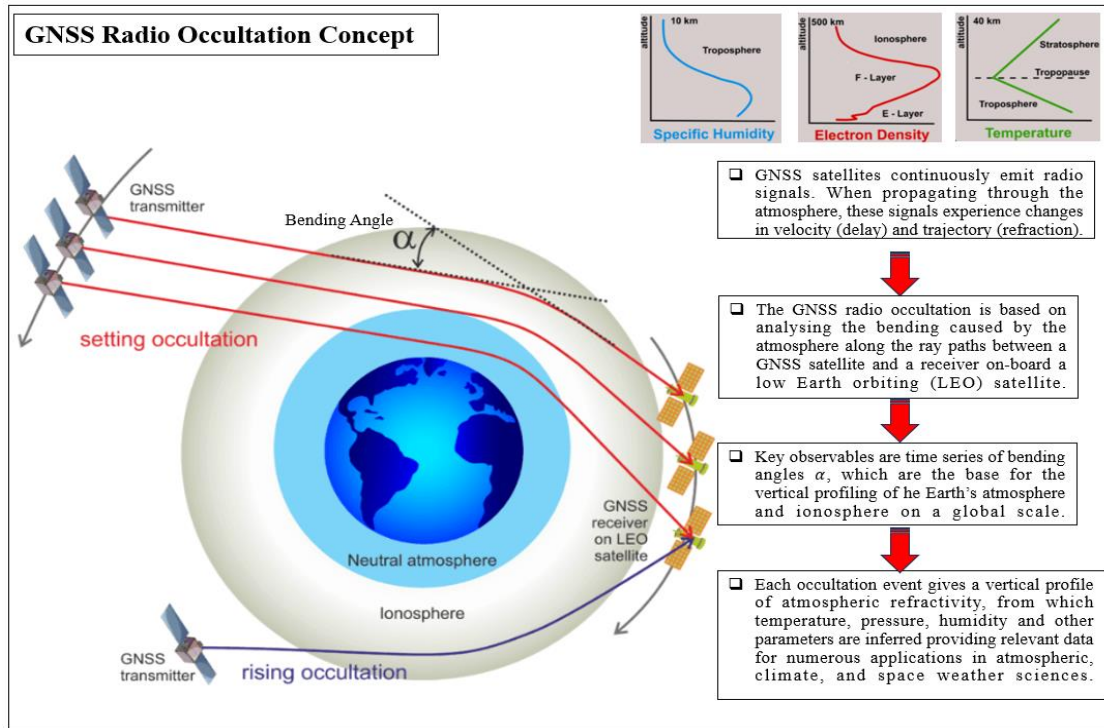


Figure 9. GNSS radio occultation rising and setting scenarios for assessing the ionosphere and the neutrosphere.

Using just a single LEO satellite, approximately 500 atmospheric profiles, distributed across the globe, become available for daily utilization exclusively with GPS data. This number grows dramatically when the satellite receiver has multi-GNSS capabilities (considering, for example, Galileo satellites). GNSS-RO observations in the lower troposphere can be used to estimate planetary boundary layer height and determine water vapor in the troposphere. Main meteorological centers use GNSS-RO information, and GNSS-RO data has a considerable influence on prediction error reduction.

### Limitations

One of the significant disadvantages of atmospheric sensing by radio occultation analysis is the rank deficiency problem in determining the most significant atmospheric parameters, namely temperature, pressure, and humidity concentrations, only from refractivity data. Also, the obscuration of radio waves by celestial bodies with atmospheres causes an excess of the Doppler shift of signal frequency. This excess, in comparison to the usual Doppler shift observed in vacuum when the transmitter and receiver are in relative motion, is due to atmospheric refraction deflecting



the ray lines connecting the two satellites from the straight-line path. Because the local air refraction index is affected by local pressure, temperature, and chemical breakdown, bending angle measurements must be accurately determined to provide some information about these variables.

### **2.3.3 Medium and Moderate Resolution Imaging Spectroradiometer (MODIS and MERIS)**

With a viewing swath that spans 2,330 km, MODIS is capable of observing the whole planet at a temporal resolution of 24 - 48hrs across 36 distinct multispectral bands [73]. MODIS surpasses other Terra sensors in tracking a wider array of crucial Earth indicators, rendering it an indispensable tool for scientific research. For instance, MODIS routinely quantifies the cloud cover percentage across the Earth's surface. The extensive spatial coverage provided by MODIS, combined with instruments like CERES and MISR, empowers scientists to evaluate the influence of aerosols and clouds on Earth's energy budget.

Furthermore, MODIS records cloud cover frequency and distribution, while also examining cloud properties such as the distribution and size of droplets found within liquid water and ice clouds. The instrument also measures aerosol properties, which are tiny solid or liquid particles present in the atmosphere, resulting from human actions such as biomass burning and pollution, as well as natural occurrences like dust storms, volcanic eruptions and forest fires. In addition, MODIS helps researchers in evaluating the quantity of WV present in the atmosphere's WV column, alongside the vertical disposition of temperature and water vapor. These measurements are paramount in understanding Earth's climate system.

However, the MODIS and MERIS spectroradiometers are greatly influence by clouds which affects the accuracy of measurements. Also, they have low temporal resolutions.

### **2.3.4 The Interferometric Synthetic Aperture Radar (In-SAR)**

Satellites may carry water vapor imaging spectrometers [57,74,75](see Figure 10) resembling MERIS [25] or MODIS [26]. In clear atmospheric conditions, the determination of IWV can be accomplished using infrared sensors. These sensors exhibit horizontal resolutions of 1 km for MODIS and 300 m for MERIS. The calculation of IWV relies on the assessment of the reduction in near-infrared (IR) solar radiation due to the presence of water vapor. The calculation of IWV involves the measurement of ratios between two nearby channels, one located inside the water vapor absorption spectral region and the other exterior of it. When clouds are present, the

IWV value reflects the WVC from the sensors to the topmost layer of the clouds [16] To ensure clarity in the interpretation of IWV data, water vapor readings from areas within the cloud coverage in MERIS images are systematically excluded.

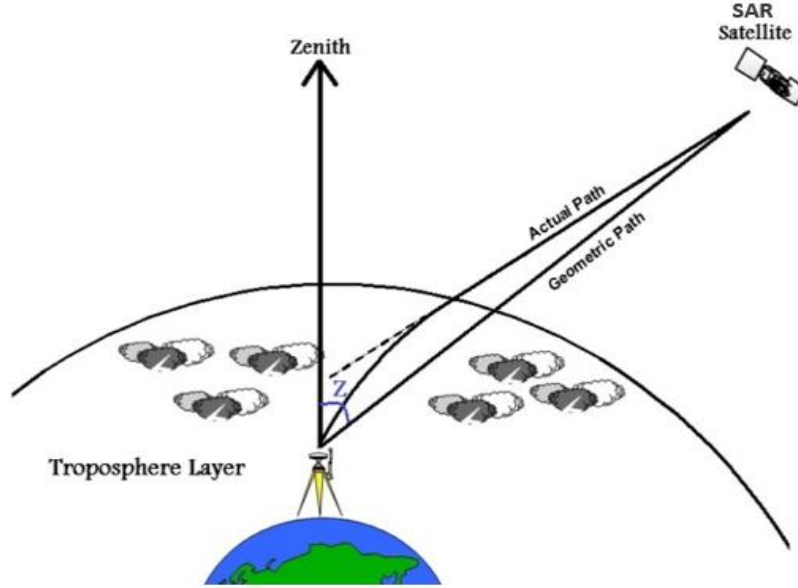


Figure 10. Tropospheric delay effect on SAR

SAR MODIS IWV, also known as the spectrometer correction technique, is a troposphere correction method that employs IWV data in near-infrared wavelengths [76]. This information gives a comprehensive measure of atmospheric moisture content in both terrestrial and marine regions. Equation (7) is used to calculate IWV.

$$IWV = \frac{1}{\rho_w R} \int_H^{\infty} \frac{W}{T_m} dH \quad 7$$

The variables denoted as  $\rho_w$ ,  $R$ ,  $W$ ,  $H$ , and  $T_m$ , represent the WV density, specific gas constant, WV, tropospheric height, and temperature, respectively. The equation (8) can be utilized to express the estimated delay of the spectrometer in the phase.

$$\phi_{trop}^{wet} = \frac{-4\pi}{\lambda} \frac{\Pi}{\cos\theta} \cdot IWV \quad 8$$

The symbol  $\Pi$  is a factor of conversion which is equal to 6.2, and is subsequently deducted from the tropospheric phase value acquired from MODIS."

### Limitations

Synthetic aperture radar satellites are often placed in low Earth, sun-synchronous orbits.

SAR systems capture images through a side-view approach, utilizing incidence angles of typically between  $18^\circ$  to  $50^\circ$ . This method leads to integrated delays occurring along a slanted ray that correlates with the line of sight (LOS). The problem of signal decorrelation arises when working with In-SAR data for extended periods due to the fluctuating backscatter characteristics of the Earth's surface. In order to address this issue, InSAR analysis directs attention towards Persistent Scatterers (PS) - stable elements that endure over time.

InSAR-derived zenith delays provide excellent coverage. However, their reliability in capturing large-scale regional trends and establishing an absolute reference is limited due to the discrete characteristics of interferometric measurements. Furthermore, residual orbital errors, tidal loading, and crustal tides introduce long-wavelength signals that may result in potential inaccuracies. To address data inconsistencies and modify spatial patterns, particularly the elongated wavelength signal component associated with the expected IWV, it is imperative to incorporate supplementary inputs or external data as constraining factors [76]. While InSAR was initially developed for purposes such as generating Digital Elevation Models and monitoring surface displacements, it also possesses the capability to deduce partial variations in Integrated Water Vapor, employing specialized spatial and temporal filtering techniques. This capability bears resemblance to that of GNSS[16]. In-SAR mounted on US AQUA and TERRA orbiting satellites are well-established tools for acquiring water vapor information [77]. Nevertheless, the majority of sun-synchronous satellites have low temporal resolution which ideally occurs between 24 – 48 hrs., rendering them incapable of observing rapid atmospheric fluctuations.

### **2.3.5 The Very-long-baseline interferometry (VLBI)**

Geodetic sensors offer the means to determine atmospheric water vapor content through various techniques, including VLBI, In-SAR and GNSS. VLBI relies on simultaneous observations of radio signals from extragalactic sources, such as quasars, using minimum pair of radio antennas on the ground. The received signals are analyzed with a wired link between two antennas and a correlator. Nonetheless, VLBI requires each observation place to maintain a precise atomic clock for the integration of signals received from remote antennae, facilitating the study of radio waves. The primary objective of VLBI is the accurate computation of the coordinates and the Earth orientation parameters (EOP) designated radio source locations. However, as argued by Böhm [17], an accurate modeling of WVC is critical for determining EOP or VLBI site coordinates,

as these parameters are closely linked to the neutral atmospheric delay and atmospheric water vapor concentration. To achieve this, methods outlined in Niell et al. [78] can be employed to predict a site's position, and prevalent wet delay.

### **Limitations**

VLBI, much like GNSS, was originally designed primarily for location and timing applications, rather than the monitoring of atmospheric water vapor distribution. Consequently, its measurements of IWV can be subject to compromises. Several factors contribute to imprecise ZWD estimation in VLBI:

1. **Observational Noise:** Variability in measurements introduces noise into the data.
2. **Inaccuracies in A Priori Hydrostatic Delay:** Errors can occur in the initial calculation of hydrostatic delay.
3. **Inaccuracies in Hydrostatic and Wet Mapping Functions:** The functions used to map the delay can contain inaccuracies.
4. **Systematic Delay Changes with Elevation:** Delays may change systematically with elevation, affecting measurements.
5. **Unmodeled Effects:** Azimuthal asymmetry of atmospheric delay and other unaccounted factors contribute to errors.

These factors collectively impact ZWD predictions over various time scales. Inaccuracies in the constants used for a priori computation of zenith hydrostatic delay result in inaccuracies in tropospheric delay estimates. Additionally, the hydrostatic mapping function changes daily, and observation noise and errors in surface pressure readings can occur, spanning from minutes to hours [78].

### **2.3.6 The Geostationary Satellite Observation**

GEO satellites like the GOES, Japanese multi-functional transport satellite (MTSAT) and the Chinese Feng-Yun satellite [31] in geosynchronous orbits, on the other hand, provide regular observations of the atmosphere. The utilization WV data from GEO satellites supplements existing techniques that rely mostly on measurements from sun-synchronous satellites and in-situ data. The split-window approach is used to calculate the IWV column from the brightness temperature of geostationary satellite data infrared channels. A linearized radiative transfer model that applies the

split-window technique to the atmospheric sounder of GOES VISSR is usually employed [79]. The physically based split-window strategy, however, involves starting value assumptions. Geostationary satellites [31] maintain a fixed position relative to Earth, enabling continuous atmospheric monitoring.

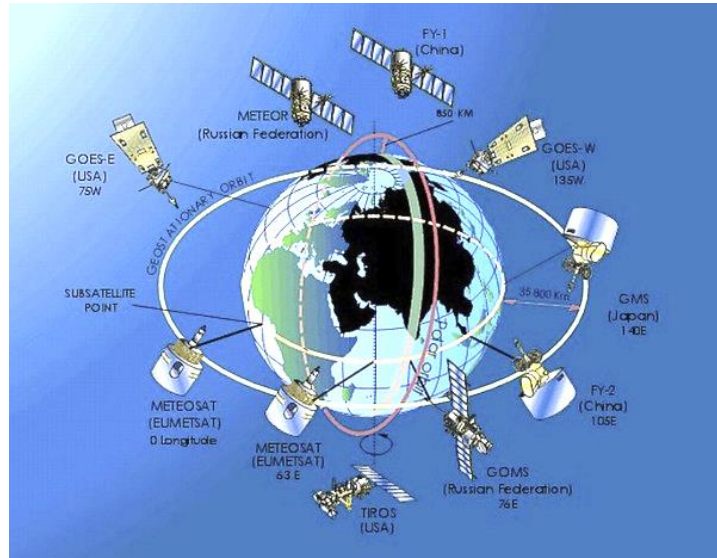


Figure 11. <https://www.sciencedirect.com/topics/earth-and-planetary-sciences/geostationary-satellite>

## Limitations

The water vapor retrieval techniques specified for Geostationary Satellites (GEO Sats) are exclusively applicable under cloud-free atmospheric conditions. This means that the estimation of the PWV column cannot be directly obtained from pixels affected by cloud cover. Nevertheless, there is a strong demand for a comprehensive water vapor dataset devoid of missing data due to the contamination of clouds or other factors, particularly for its utilization in weather and climate prediction models. To address this, numerous interpolation techniques for spatial analysis, like spline and Kriging interpolation, were employed to interpolate missing information from images of the satellites [80]. Achieving high temporal information is crucial to enhance interpolation performance, given the fixed field of view and high temporal resolution of geostationary satellites. However, these spatiotemporal interpolation techniques entail significant computational demands and may be susceptible to data anomalies. An alternative approach proposed by Sobrino et al. involves using the split-window covariance-variance ratio (SWCVR) to calculate IWV content. This method considers the substantial variation between surface temperature and air temperature within a limited observational range. Nonetheless, their research findings suggest that the SWCVR

method is vulnerable to instrumental errors [81,82].

### **2.3.7 SPIRE Satellite Constellation**

In the year 2019, SPIRE launched a constellation of 3U CubeSats into LEO, augmenting the total number of nanosatellites to eight-four. Among these, twenty to thirty satellites are dedicated to the collection of RO data [83]. The GNSS transmissions from Spire's radio occultation satellite constellation contain a wealth of ionosphere-related data. RO serves as a remote sensing technique for monitoring the electron density profile (EDP) of the ionosphere, and SPIRE aims to establish a comprehensive constellation comprising more than 100 satellites concurrently conducting RO measurements. Each Spire satellite presently employs zenith and limb pointing antennas to capture 1 Hz, dual-frequency GNSS phase measurements. These measurements are subsequently processed to generate low-latency estimations of slant TEC. Inversions of the plasma density profile are conducted using GNSS connections with low-elevation angles that pass through the ionospheric layer located beneath the satellite's orbit. Additionally, high-rate 50 Hz phase data is utilized to identify smaller ionospheric features such as gravity waves, sporadic E-layers, and other irregularities. These features are primarily employed on Earth's lower neutrosphere for remote sensing. To ensure clarity and objectivity, technical terms are explained upon their initial use, and unnecessary jargon is avoided. Spire has the capability to continuously receive GNSS signals that extend to the E-region from near-zenith angles. This capability enables the processing of electron density profiles and the acquisition of long TEC data arcs. Upgrades to the receiver technology implemented by Spire enhance the accuracy of differential code biases estimation and enable the collection of high-rate 50 Hz data when scintillation events are detected, similar to the constellation observing system for meteorology, ionosphere & climate (COSMIC-2) mission. However, it's important to note that Spire's primary focus is on determining TEC, and it does not provide information on IWV.

### **2.3.8 Kyutech Spatium Projects**

Kyushu Institute of Technology developed, launched, and operated two satellites, SPATIUM-I (2U) and SPATIUM-II KISTUNE (6U) (see Figure 12), based on commercial-off-the-shelf-components. The two satellites were developed for the scientific study of the atmosphere in the ionospheric region. Ionospheric density, also known as TEC, was determined based on the signal propagation time delay due to ionosphere's plasma. The SPATIUM-I mission was designed

with the primary goal of demonstrating the practicality of creating a global three-dimensional map of the ionosphere. This endeavor was achieved through the deployment the CubeSat mounted with a precise atomic clock [84].

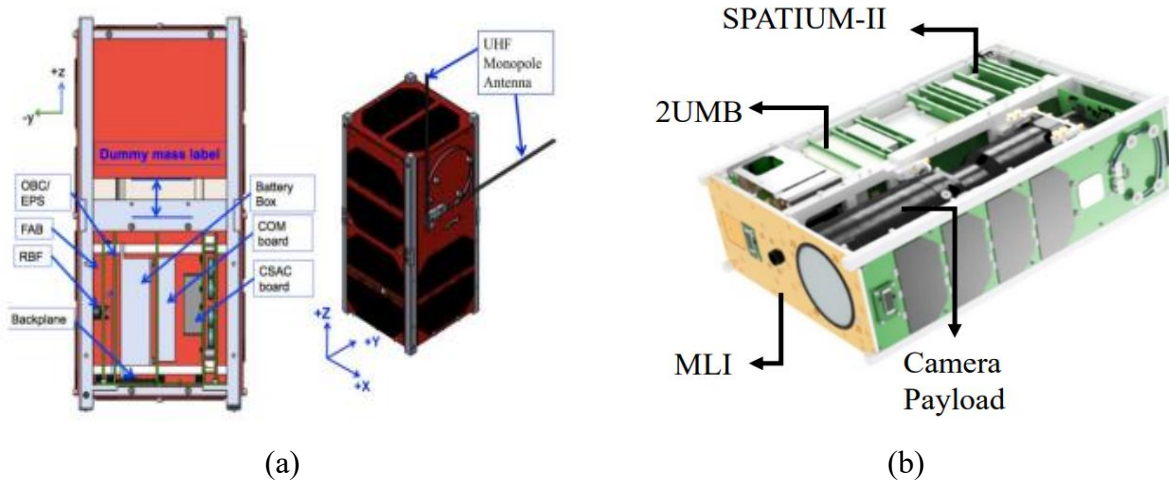


Figure 12. Kyutech SPATIUM satellites (a) SPATIUM-I (b) KISTUNE carry SPATIUM-II payload

On October 6th, 2018, the SPATIUM-I satellite was released from the International Space Station (ISS). SPATIUM mission successfully attained the following predefined objectives:

- a. Utilization of chip scale atomic clock (CSAC) onboard the satellite to provide a highly accurate clock signal for measuring radio wave propagation delay.
- b. Demonstrating transmission with SS modulation at 467 MHz using CSAC as the clock source.
- c. Conducting an onboard transmission and reception at 401 MHz.
- d. Demodulation of the SS signal at Kyutech GS.
- e. Achieving time synchronization among several GSs through the use of CSAC clocks and GPS.
- f. Reading the carrier wave phases at frequencies of 467 MHz and 401 MHz from the SPATIUM-I satellite.

The Spatium-II mission achieved the successful demodulation of SS signals on board, enabling precise time delay measurements of electron content [33]. The UHF signal transmission was conducted by ground stations as part of the SPATIUM-II mission. Subsequently, the signal delay time was calculated by KITSUNE's onboard SDR and RPi computer. This calculation allowed for the determination of TEC, which reflects the overall plasma density between the GS and satellite. The SPATIUM-II mission primary objective was to demonstrate the capability to

identify signal delay time with a high precision of 100 ns. However, currently, no Kyutech mission has been implemented to demonstrate the ability to measure atmospheric water vapor.

### **2.3.9 Others: Surface Meteorology, Radio Sonde, Lidar, Microwave Radiometers, Stratospheric Ballons**

#### **a. Surface Meteorological Sites**

Surface meteorological locations primarily gather temperature, pressure, and humidity readings [12]. However, surface meteorological findings, as highlighted by Braun [85], do not comprehensively capture the entirety of the atmospheric water vapor boundary layer, as they are closely tied to interactions between the atmosphere and the Earth's surface. Data collection from surface meteorology are collected at least once a day, sometimes more frequently, and their spatial coverage is uneven.

#### **b. Radiosondes**

A radiosonde is an instrument designed to monitor meteorological variables throughout the vertical profile of the atmosphere and transmit the collected information to a terrestrial-based processing and receiving station. Over an extended period [30,85], networks of radiosonde instruments served as main in-situ monitoring stations for WV data. Radiosondes allow for the acquisition of various climate and weather indicators, such as pressure, temperature, and relative humidity. These instruments routinely measure the variations in temperature, pressure, and humidity as they ascend via balloon from the Earth's surface to altitudes of approximately 30 kilometers. Radiosondes are regarded as the standard of accuracy in meteorology, often capable of providing IWV measurements with a precision of just a few millimeters. Equation (9) is employed to calculate the value of the IWV column:

$$IW = \frac{1}{g} \int_{p_2}^{p_1} x dp \quad 9$$

The IW represents column of IWV column in millimeters within a specific layer. The atmospheric pressures at the top and bottom demarcations of each layer are denoted as  $p_2$  and  $p_1$ , respectively, with units in pascals. The mixing ratio, represented by  $x$  and measured in grams per kilogram can be determined using Equation (10):



$$x = \frac{0.622 \cdot E}{p - E} \quad 10$$

In Equation (10), the pressure of the atmosphere  $p$ , while the pressure of vapor ( $E$ ) and can be calculated as  $E = rh \cdot E_s(T)$ , where  $rh$  represents the atmospheric relative humidity as a percentage and it is a parameter available in data files of radiosondes. Additionally,  $E_s$  signifies the pressure of the vapor in the saturation phase, and it is dependent on the temperature ( $^{\circ}\text{C}$ ) [67].

Radiosondes are typically launched twice daily, which imposes limitations on their temporal resolution. This restricted temporal resolution hinders the ability to capture critical meteorological events like the formation of the layer of convective demarcation and the passage of warm and cold fronts. Additionally, radiosondes collect only one data point per height measurement, leading to potential inaccuracies in the measured relative humidity profiles. On average, radiosonde data is associated with an uncertainty of approximately 5% [86]. Notably, Vaisala RS2-80MB radiosondes have been observed to exhibit IWV errors as high as 0.6 cm, with 0.45 cm and 0.15 cm attributed to pressure and humidity sensor inaccuracies, respectively [87]. Radiosondes are constrained in their utility due to several factors, including their high operational costs, susceptibility to dry bias, time lag in data transmission, potential calibration errors, declining sensor performance under cold and dry conditions, and limited coverage, particularly in overseas and Southern Hemisphere regions.

### c. Microwave radiometric measurements

The determination of IWV along the line of sight of a terrestrial-based WV radiometer (WVR) hinges on the monitoring of brightness temperatures associated with water vapor at two distinct spectral bands. One of the spectral frequency bands exhibits sensitivity to WV, while the other is responsive to liquid water, enabling the differentiation of these two components. Vertical profiles of WV can subsequently be inferred through the application of the optimal estimation technique, leveraging the observed water vapor brightness temperature spectrum [16]. Notably, observations conducted with water vapor radiometers offer excellent time resolution. However, instruments designed for ground-level water vapor detection often lack spatial resolution. In contrast, WVRs with downward-looking configurations from orbit provide high spatial resolution but suffer from reduced time resolution.

The TP/WVP-3000 employs radiometric microwave technology to conduct sequential

scans at twelve microwave frequencies, measuring brightness temperatures at each frequency. This encompasses five frequencies within the K-band, ranging from 22 to 30GHz, strategically positioned on the periphery of line of absorption of WV at the 22 GHz. Moreover, there are seven frequencies within the V-band, spanning from 51.3 to 58.8 GHz, strategically positioned adjacent to the 60.0 GHz molecular oxygen complex. Every channel possesses a bandwidth of 300 MHz [88]. The combined analysis of the IR sensor's data on cloud-base temperature and the retrieved temperature profile facilitates an estimation of the height of the cloud base, which encompasses ice, mixed clouds or warm liquid. Relative humidity estimations at various altitudes are achieved through the integration of temperature and water vapor content (WVC) data.

For calibration, the 22-30 GHz channels undergo automated tipping processes to achieve a calibration precision of 0.3 K RMS, whereas the calibration of 51-59 GHz spectrums to a precision of 0.5 K RMS using nitrogen liquid as the target. The radiometer undergoes regular calibration using liquid nitrogen, typically at monthly intervals and whenever it is relocated. The complete scanning process involving all twelve channels necessitates approximately 23 seconds to complete. However, this study observed a negligible 92-second disparity in duration across the profiles under examination. Also, the radiometer's radome experiences a decrease in accuracy when confronted with the presence of liquid water and heavy precipitation, a characteristic shared with other microwave radiometers. Consequently, retrievals cannot be effectively conducted under such meteorological conditions. During rainy events, the microwave radiometer's operational performance is compromised.

#### **d. Rahman Lidar Measurements**

LiDAR sensors may operate satellite-, air-borne, or ground-based on aircraft and satellites. The fundamental principle underlying atmospheric Lidar measurements involves the emission of signal using dual closely spaced frequency bands. One of bands is sensitive to the presence of WV, while the other remains unaffected by it. Through the analysis signals shifted by Raman originating from both nitrogen and WV, Lidar data can be utilized to estimate the water vapor mixing ratio. This approach is employed because nitrogen is known to be consistently proportional to dry air.

Relative humidity profiles can be derived through the integration of Raman-lidar technology, which has been developed for the profiling of both temperature and moisture [13]. This approach involves the concurrent monitoring of temperature and WV ratio of mixing utilising

two distinct Raman-lidar channels which are the pure rotational and the WV channels of Raman lidar. The theoretical framework for deriving relative humidity profiles from Raman-lidar data is elucidated through a set of lidar equations. Lidar measurements are feasible when the laser beam encounters no obstruction from cloud cover. The amalgamation of traditional radiosonde observations with state-of-the-art lidar technology represents a significant enhancement in the quality of observed tropospheric humidity datasets

The Raman lidar system, utilized for temperature and humidity measurements, is anticipated to furnish relative humidity profiles with a relative error of approximately 10%. This system offers a vertical resolution spanning from the 100-meter boundary layer to altitudes ranging from 500 to 1000 meters within the free troposphere. The temporal resolution varies, with measurements available every 10 minutes within the boundary layer and extending to 1 hr within the free troposphere. These measurements are feasible up to heights of 5000 to 7000 meters during daylight hours and encompassing the entire troposphere during nighttime observations [13]. While both differential absorption lidar and Raman lidar possess the capacity to determine absolute humidity and water-vapor-to-dry-air mixing ratios, the accuracy of lidar-based measurements is hindered when estimating tropospheric relative humidity profiles. This limitation arises from the necessity of concurrently measuring both temperature and water vapor.

#### e. Sun Photometry [89]

Sun photometry is a remote sensing method utilized to measure various characteristics of the atmosphere, including the concentration of atmospheric water vapor. This method relies on the principle of spectroscopy to analyze the sunlight passing through the troposphere. Here's an overview of the sun photometry method for atmospheric water vapor measurement:

##### **Principle of Sun Photometry:**

- Solar Radiation: solar arrays are emitted by the Sun across a broad range of wavelengths, including visible and NIR light.
- Atmospheric Interaction: As sunlight passes through the Earth's atmosphere, it interacts with atmospheric constituents, including water vapor molecules.
- Absorption and Scattering: Water vapor molecules absorb specific wavelengths of solar radiation in the NIR and infrared regions. This absorption is due to the presence of water vapor's molecular vibration and rotation bands.

- **Transmittance and Radiance:** Sunlight that reaches the Earth's surface has undergone absorption and scattering by atmospheric constituents. The amount of sunlight transmitted through the atmosphere depends on its wavelength, with certain wavelengths being more affected by water vapor absorption than others.

#### **Sun Photometer Instrumentation:**

- **Sun Photometer:** A sun photometer is a specialized instrument designed to measure the intensity of sunlight at various wavelengths. It typically consists of a telescope, optical filters, and detectors.
- **Optical Filters:** Sun photometers use specific optical filters that isolate the wavelengths of interest for water vapor measurement. These filters allow only the desired spectral bands to pass through.
- **Detectors:** Detectors in the sun photometer measure the intensity of sunlight within the selected spectral bands. These measurements are often converted into radiance values.

#### **Measurement Procedure:**

- **Solar Observation:** The sun photometer is pointed at the sun, and measurements are taken when the sun is at its highest point in the sky. This ensures that sunlight passes through the maximum atmospheric path.
- **Spectral Measurements:** The sun photometer measures the intensity of sunlight at multiple wavelengths within the NIR and infrared regions. These measurements are collected as the sunlight passes through the atmosphere.
- **Data Analysis:** The recorded radiance values are analyzed to determine the quantity of WV in the atmospheric column. The analysis involves comparing the observed radiance with reference spectra and applying retrieval algorithms to derive the water vapor content.

#### **Advantages of Sun Photometry for Water Vapor Measurement:**

- Sun photometry provides column-integrated water vapor measurements, giving insights into the WV vertical distribution.
- It is a non-intrusive and remote sensing technique that can be used for atmospheric profiling over various locations.
- Sun photometers are relatively portable and can be deployed in the field for atmospheric research.

### **Limitations**

- Sun photometry measurements are highly dependent on atmospheric conditions, including cloud cover and aerosol concentrations, which can affect the accuracy of retrievals.
- Calibrating and maintaining sun photometers is essential to ensure accurate measurements.
- It provides integrated water vapor content along the instrument's line of sight but does not offer vertical profiles.

In summary, sun photometry is a valuable technique for measuring atmospheric water vapor content by analyzing the absorption features of water vapor molecules in sunlight. This method is used in atmospheric research, climate studies, and environmental monitoring to assess water vapor's impact on radiative processes and weather patterns.

### **f. Balloon-Borne Radiation Measurement for Water Vapor**

Balloon-borne water vapor measurements involve the use of specialized instruments and sensors carried by balloons to collect data related to water vapor in the Earth's atmosphere [90]. These measurements are conducted at various altitudes as the balloon ascends, providing valuable insights into the vertical distribution of water vapor in the atmosphere. Balloons are equipped with instruments such as radiometers and spectrometers designed to detect and quantify radiation associated with water vapor. Measurements are taken at different altitudes, from near the surface to the upper troposphere or stratosphere, depending on research objectives. Instruments detect radiation emitted or absorbed by water vapor molecules, including microwave, infrared, or other electromagnetic radiation. As the balloon ascends, it collects data on radiation levels at multiple altitudes. Data can be transmitted to ground stations or stored onboard. The primary goal is to obtain vertical profiles of water vapor concentration, providing information on how water vapor varies with altitude. These measurements are used in studies of atmospheric moisture distribution, humidity gradients, cloud formation, and other processes influenced by water vapor. Instruments are calibrated and validated to ensure measurement accuracy. Data contribute to our understanding of climate systems, weather patterns, atmospheric dynamics, and improve weather forecasting and climate research. Balloon-borne water vapor measurements play a crucial role in advancing atmospheric science and enhancing our ability to predict weather and understand climate change.

## 2.4 Summary of Atmospheric Water Vapor and TEC Measurement Techniques

Table 2 displays meteorological, geodetic, and planned sensors and methodologies for monitoring atmospheric water vapor concentration. The initial five lines detail methodologies for meteorological water vapor measurement, followed by three lines for geodetic techniques. Finally, a recommended methodology for water vapor sensing is outlined. The primary column uses 'M' to indicate meteorological sensor and measurement techniques, 'G' for geodetic sensors, and 'COTS' for commercial off-the-shelf components. If no criteria are specified for sensing, the sensors or procedures can measure both day and night, irrespective of the conditions of weather. Yellow markers are used to indicate the sensors and methodologies employed in this research.

*Table 2. Comparison of water vapor measurement methods*

Technique	Observing Geometry	Temporal Resolution	Spatial Resolution	Accuracy	Conditions
Surface meteorology	ground	1–60 min	few meters–tens of meters	few mm	affected by environment
Lidar	ground, air, and space	low–high depending on observing geometry	low–high	few mm	cloud-free sky
Microwave radiometers	ground, air, and space	5–15 min	low–high	1–5 mm	rain-free sky
Sun photometer	ground	few times with high solar illumination intensity	High	few mm	direct sunlight and clear sky
VLBI	ground	mins–days (depends on schedule)	very low (few sites)	few mm	none
Polar satellites	space	6–12 h	1–10 km	few mm–1 cm	none
Radio sondes	air	1–4 times a day	low	1–3 mm	none
Imaging spectroradiometers	space	MODIS (1–2 days) MERIS (3 days)	MODIS (250 m–few km), MERIS (300 m)	few mm–1 cm	cloud-free sky
Remotely piloted vehicles and Instrumented aircraft	air	depends on flight duration (few mins–few hrs.)	few meters–tens of meters	few mm	depends on weather
In-SAR	space	6–12 days	high	1–2 mm	none
GNSS satellites (radio occultation)	space	1–60 min	high	1–5 mm	none
GNSS satellites to standard GPS ground receivers	ground	30 s–few mins	tens–hundreds of km	1–5 mm	none

Geostationary satellites	space	Mins-hourly updates	one-tens of km	few mm-few cm	none
--------------------------	-------	---------------------	----------------	---------------	------

## CHAPTER 3

### SATELLITE AND GROUND SYSTEMS DESIGN CONFIGURATION

#### 3.1 Overview

In this chapter, the author discusses the proposed systems design configuration for the ground and space segments that can be utilized to measure atmospheric water vapor. Several commercial off the shelf hardware components that are used to make the satellites mission board are given and how they integrate is explained in detail. On the ground station, design configuration of channels of communications for atmospheric water vapor measurement as well as downlink of mission data are elaborated.

#### 3.2 Proposed System Design Configuration for Measuring TWVC

The system design architecture for each satellite in the ISL network is made utilizing COTS components integrated within the limited power, volume, and size constraints of small satellites (CubeSats). Each satellite in the ISL network has the water vapor mission measurement board, which comprises the Ettus research universal software radio peripheral (USRP) - software defined radio (SDR) model b205 mini-i, the RaspberryPi-4 (RPi-4) model B, GPS module, RF radio frequency (RF) switches board, the amplifier and the antenna. For ground tests only, attenuators and delay pulse generator were utilized.

##### 3.2.1 Satellite Mission Board Hardware

Table 3 below shows the mission hardware and their functions used in this research

*Table 3. List of satellite mission hardware and functions.*

Component	Functions
USRP SDR	<input type="checkbox"/> Transmit data <input type="checkbox"/> Receive data <input type="checkbox"/> RF tuning
Raspberry Pi	<input type="checkbox"/> SS-BPSK signal processing <input type="checkbox"/> Frequency manipulation algorithms <input type="checkbox"/> Data processing



	<input type="checkbox"/> Saving mission data <input type="checkbox"/> Acquire GPS data from GPS module
GPS Module	<input type="checkbox"/> Acquire GPS data from GPS satellites <input type="checkbox"/> Generate 1PPS signal for time stamping <input type="checkbox"/> Generate 10 MHz clock for accuracy timing
Switch	<input type="checkbox"/> Time stamps incoming and outgoing signal <input type="checkbox"/> Switching transmitter and receiver functions
RF Amplifier	<input type="checkbox"/> Amplifies transmitted signal
Delay Pulse Generator	<input type="checkbox"/> Simulate time delay only ground test
Attenuators	<input type="checkbox"/> Attenuate signal. Only for ground tests

### 3.2.1.1 USRP 205mini-i Software Define Radio (SDR) Transceiver

SDR, which incorporates most of the recent technological advancements is becoming the ultimate transmitter and receiver for modern and next generation communication systems [91]. The integration of cognitive and software control intelligence to the radio design enabled SDR anatomy to have a scalable, extensible, reprogrammable, and modular design that support evolution over time and that can be remotely configured based on operator requirements for a particular application. In SDR, the digital domain of the communication system is implemented in software rather than the conventional hardware circuits [43]. The SDR hardware supports software developments environments such graphics processing units (GPUs), field programmable gate arrays (FPGAs), general purpose processors (GPP), and digital signal processors (DSP) to build remote or automated controls that alters the SDR operations. Furthermore, on small satellite, SDR can be implemented in a miniaturized and lightweight way that fits the constraints of limited power, size, and weight of CubeSats.

The detailed architecture of the SDR hardware is shown in Figure 13 (board), Figure 14 (schematic). The typical specifications of the SDR used in this research is given in Table 4. The experiment was conducted using the USRP-SDR b205mini-i as the transceiver. It consists of two main functional partitions: the transmission (TX) and the reception (RX2) paths. The hardware design of the transceiver is divided into three blocks: the RF front-end (AD9364 RFIC), the digital buffer (Spartan6 FPGA), and the USB 3.0 controller [92].

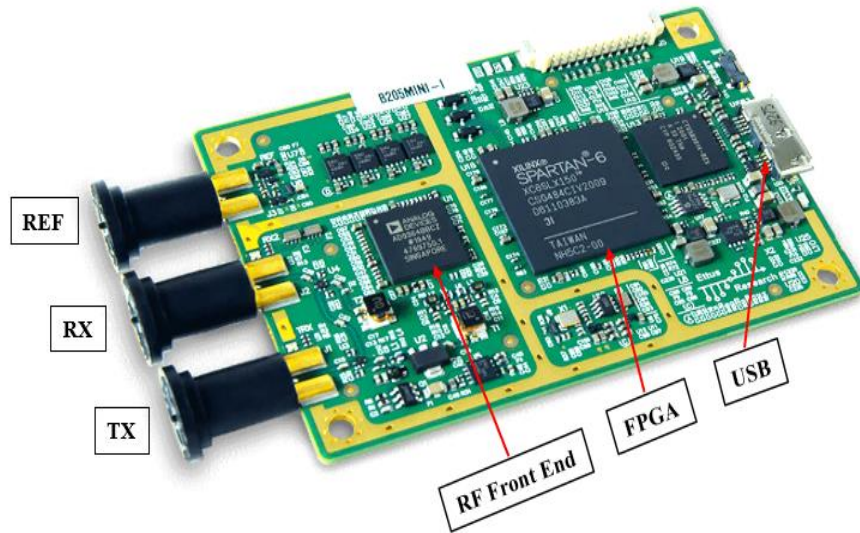


Figure 13. USRP B205 mini-i SDR board

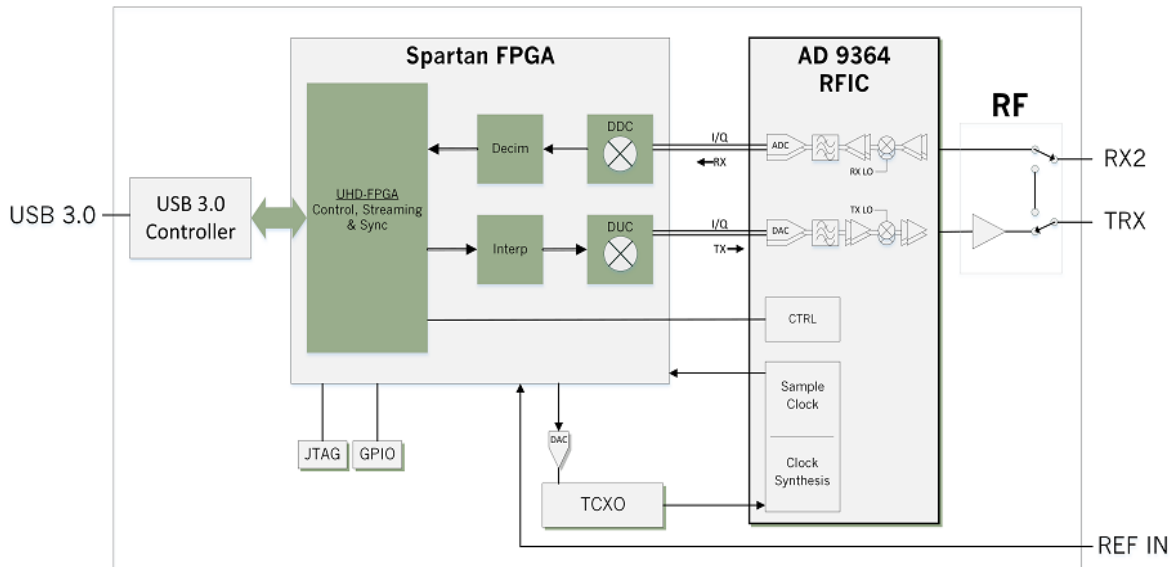


Figure 14. USRP B205mini-I schematic | ETTUS research SDR architecture [92]

Table 4. Details the main specifications of the SDR in both paths.

Parameter	Specification
Radio spectrum	70MHz - 6GHz
Bandwidth	<200kHz -56 MHz
Resolution (ADC/DAC)	12bit
Sample Rate (ADC/DAC)	61.44 Msps
Duplex	Full
Programmable Logic Device	Xilinx Spartan-6
Chipset	AD9364 RFIC

Interface (Speed)	USB 3 (5 gigabit)
Frequency Accuracy	+/-2ppm
Rx Noise Figure	<8 dB
Operating Temperature	-40-75 degrees
Transmit Power	10 dBm

**a. RF Front End**

The RF front-end section, which includes the AD9364 RFIC, is a highly integrated, reconfigurable, and reprogrammable RF agile transceiver designed to handle analog signals with high performance. The SDR parameters of the FR front end such as the frequencies, gains, BW, sampling rate can be configured. Weak radio signals input from the RX2 pin are amplified by the low noise amplifier (LNA) and then the radio frequency is converted by a downconverter consisting of mixer and receiver local oscillator (RX LO). Subsequently, extraneous signals are filtered out using the band-pass filter (BPF), and the data is transformed into a digital signal through the analog-to-digital converter (ADC). The discreet signal stream is transferred to the next digital buffer portion for further processing. Conversely, the transmitted data received from the digital buffer section is translated into an analog signal by the digital-to-analog converter (DAC). Subsequently, the data is upconverted using a mixer and a transmitter local oscillator (TX LO), amplified by the power amplifier, and then output from the TX pin.

**b. Data Buffer**

The data buffer portion which is the Xilinx Spartan-6 XC6SLX150 field programmable gate array (FPGA) is a block that temporarily stores data received (or transmitted) from the AD9364. It performs processing such as decimation, interpolation, and frequency conversion by numerical calculation of the digital down conversion (DDC) and digital up conversion (DUC). These processes reduce the burden on the processor (in this case RPi) responsible for SDR signal processing.

**c. USB Controller**

The USB controller part exchanges data flowing from the data buffer part with raspberry pi microcomputer.

### 3.2.1.1.1 USRP 205mini-i SDR Output Power

The SDR Output Power was measured using a Rhodes and Schwarz Power Sensor NRP18T with DC to 18 GHz frequency range as well as -35dBm to +20dBm level range. SS- transmission were executed from RPi's GNU Radio, transmitted through the Tx terminal of the SDR, measured with the power meter sensor and recorded with the R& S Power Viewer software v11.3 installed in another PC as shown in the Figure 15. By varying the gain of the SDR Tx, the maximum output power obtained from the SDR is 16 dBm as shown in Figure 16.

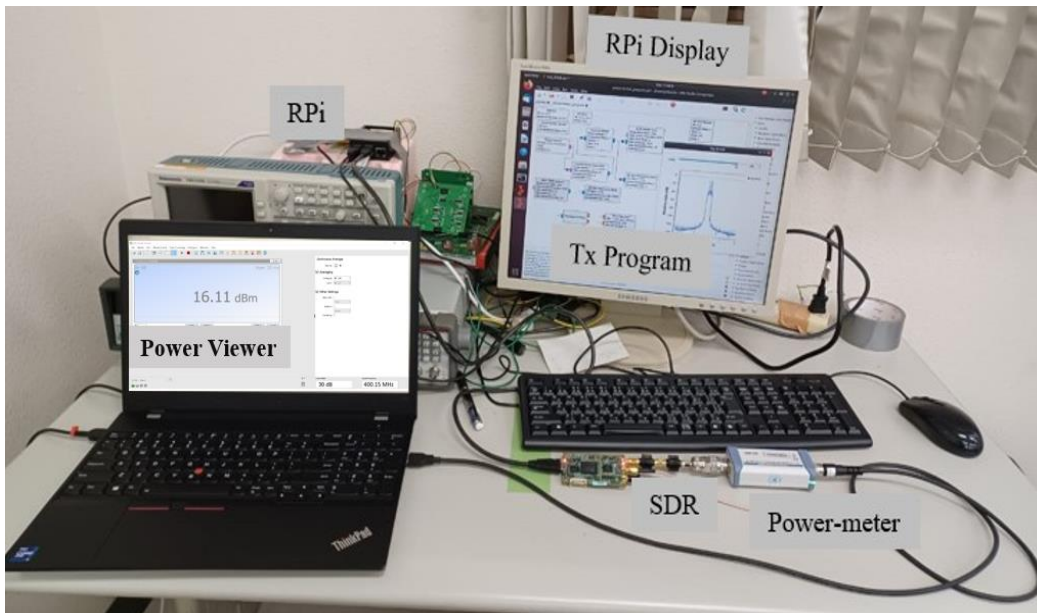
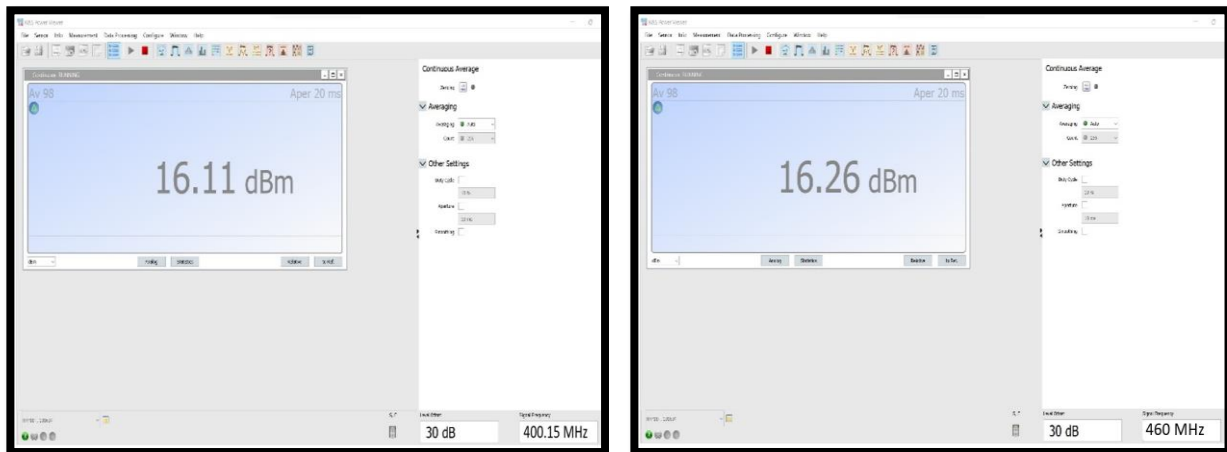


Figure 15. Power meter measurement test for SDR output power



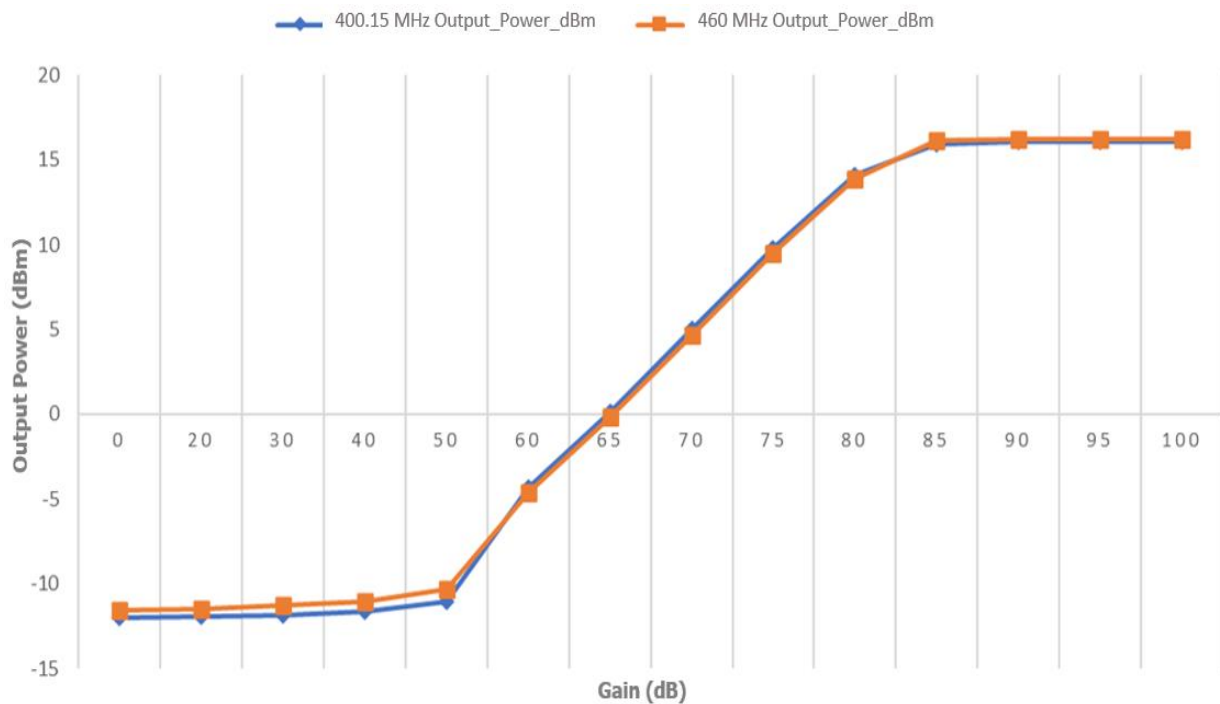
(a) Maximum Output Power @400.15 MHz (b) Maximum Output Power @460 MHz

Figure 16. (USRP B205 mini-i maximum output power)

Power meter readings were collected at various gain values of the receivers in order to retrieve the maximum gain with the maximum performance, as well as to understand the saturation points of the USRP SDRB 205 mini-i. As a result, the following powers and corresponding gains were acquired as represented in the Table 5 below. The graph in Figure 17 shows that saturation is reached a gain of around 87 dB. Beyond 87 dB, the performance of the SDR degrades.

*Table 5: SDR output power vs corresponding gains*

Freq (MHz)	Gain (dB)	0	20	30	40	50	60	65	70	75	80	85	90
400.15	Output Power (dBm)	-11.98	-11.95	-11.84	-11.60	-11.06	-4.31	0.14	5.02	9.78	14.13	15.94	16.11
460	Output Power (dBm)	-11.54	-11.51	-11.24	-11.08	-10.30	-4.62	-0.18	4.69	9.46	13.92	16.15	16.26



*Figure 17. USRP output power vs gain curve*

### 3.2.1.2 Raspberry Pi and Software's

The SDR is manipulated and controlled by the GNURadio Companion, an open-source platform running on the Raspberry Pi as a processing computer. and Raspberry Pi-4 model B as the processor that controls the SDR transceiver operations as shown in Figure 18. The Quad core Cortex-A72, 64-bit edition, 4GB RAM, RPi-4 microcomputer was used. USRP hard drives (UHD), GNUOctave and GNURadio Companion (GRC) are installed in UBUNTU Linux version 20.04

LTS operating system environment. The USRP UHD is an open-source software driver and API that is freely available. It operates on a general-purpose processor (GPP) and is responsible for communication with and control of all USRP SDR devices. UHD facilitates cross-platform support for multiple industry standard development frameworks, including radio frequency network on chip (RFNoC), LabView, MATLAB, GNUOctave and GNURadio.

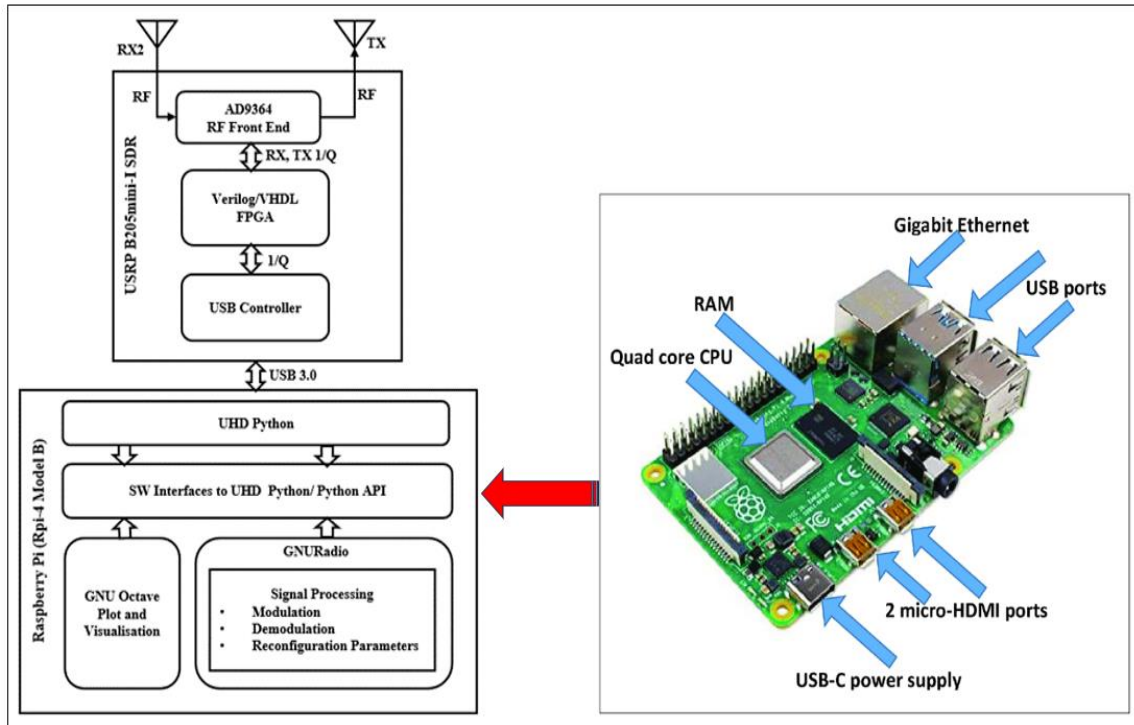


Figure 18. Raspberry Pi-4 model B configuration with SDR

UHD GPP driver and firmware code is scripted in Python or C/C++ whereas the FPGA code is developed in Verilog or very high-speed integrated circuit (VHSIC) hardware description language (VHDL). GNURadio is an open-source signal processing platform based on Python and or C/C++ that provides the necessary tools to implement software radios and it is licensed under the GNU general public license (GPLv3 or later) [93]. For this project, GNURadio Release 3.8.0 was utilized. To stream, plot and visualize the flow of information within the GNURadio using external software in 2D/3D in real time a powerful mathematics and command based oriented, GNUOctave software can be utilized.

### 3.2.1.3 GPS System

Orion B16 GPS module manufactured by SkyTraq company [94] is mounted on each

station satellite in the ISL network to provide the location and time data, 10 MHz lock, and inject 1PPS signal of the incoming and outgoing signals through the RF switch. The module was selected based on its flight heritage, tracking sensitivity of -165dBm, time-frequency hypothesis testing of 16 million per second and 2.0 CEP accuracy. Figure 19 shows the module and the display of the location, time and 1pps signals obtained during the test.

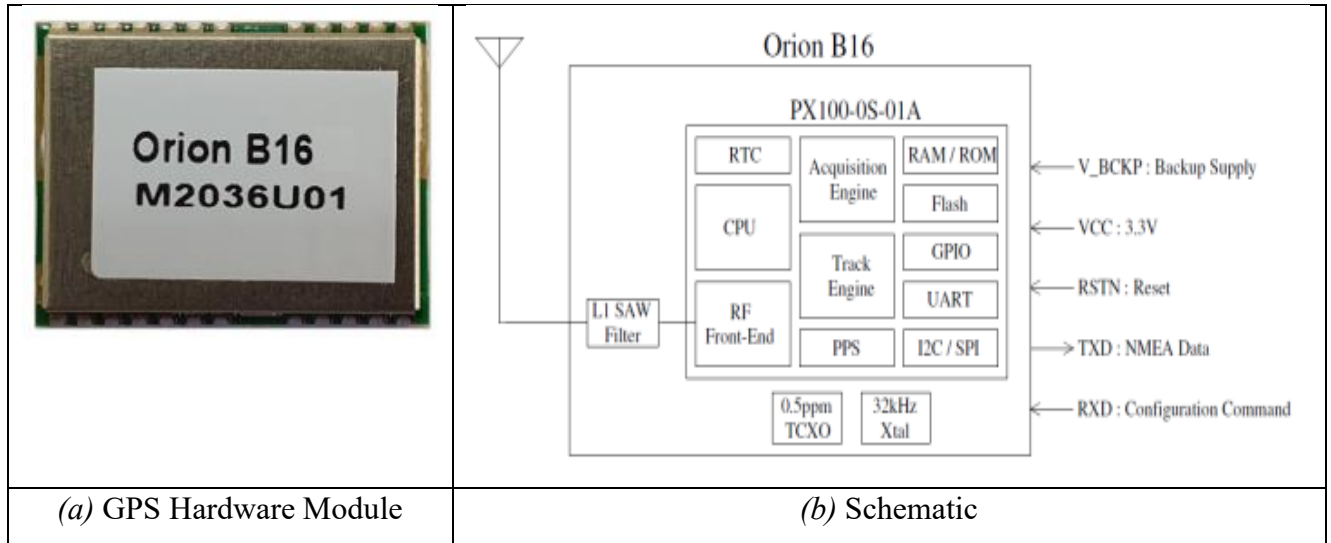


Figure 19. GPS module Orion B16

The data was saved with .nmea file and the data is sent through ASCII characters every 1 second. The RPi receives data from GPS on UART with Baud Rate 9600. During mission execution data from GPS is saved simultaneously with data from SDR to map timing of signal reception with UTC. The saved data combined with SS signal during transmission in ISL networks. Results of GPS test is discussed in Chapter 4.

### 3.2.1.4 RF Switch Mechanism

The RF switch synchronized to the time signal from the GPS is used to timestamp the incoming and outgoing signals by cutting off the signal once per second in sync with the time signal from the GPS. Incoming and outgoing signals passes through the RF cables via the UFL and MMCX connectors on the board. In either way 1 PPS time stamps from GPS module are superimposed on the signals for time detection. Jumper wires are used to interface internal and external components through the 50-pin connector on the back plane board. Figure 20 shows the hardware design and configuration of the RF switch [39].

### RF Switch Circuit

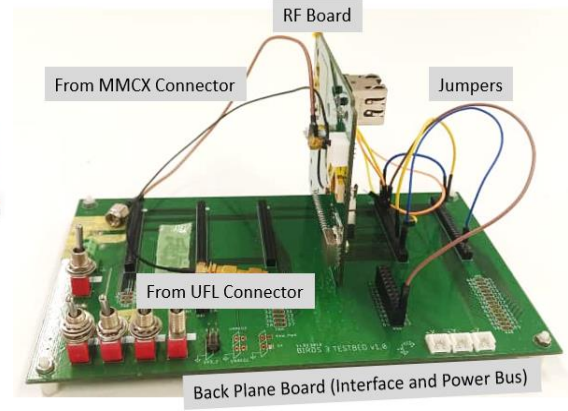
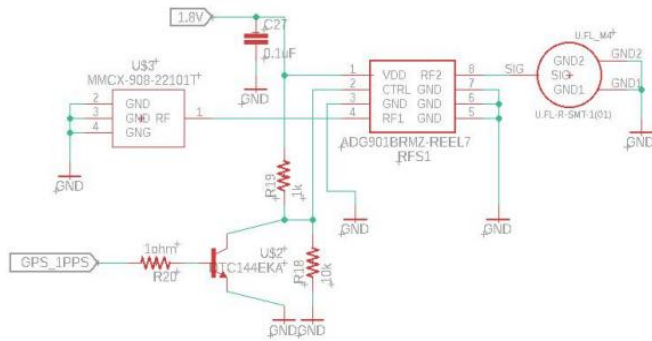


Figure 20. RF switch schematic and board (credit: Inherited from KITSUNE satellite)

### 3.2.1.5 RF Amplifier and Delay Pulse Generator

The RF amplifier has not been used in the tests. Decisions will be made when the actual satellite project starts and when the satellite size is decided. At this stage a proposal of having a 30dB RF +amplifier [95,96] qualified for small satellites has been made. Consideration of frequency, input and output power, power consumption, gain, size, mass and receiver loss are critical when selecting a power amplifier.

Since there was no influence of TWVC or TEC in this research, a delay pulse generator was used to simulate the delays due to water vapor and total electron content. The delay pulse generator is only used for ground test but it will not be employed in the actual satellite configuration. Below is the Stanford Research Systems Inc. model DG535 four channel delay/pulse delay pulse generator that was used in this research.

	<ul style="list-style-type: none"> <li>✓ Four delay channels</li> <li>✓ 5 ps delay resolution</li> <li>✓ Two pulse channels</li> <li>✓ Delays up to 1000 seconds</li> <li>✓ Adjustable amplitude &amp; offset</li> <li>✓ Standard GPIB interface</li> <li>✓ Optional <math>\pm 32</math> V output</li> </ul>
<p>(a) Physical Hardware</p>	<p>(b) Specifications [97]</p>

Figure 21. Delay pulse generator and specifications



### 3.2.2 Satellite Design Configuration

The system design architecture for each satellite in the ISL network is made using COTS components. The use of small standard satellites has been chosen for the satellite design because of their fast development time and low cost. The design configuration is divided into two parts, the satellite bus and the TWVC mission portions, as illustrated in Figure 22 below.

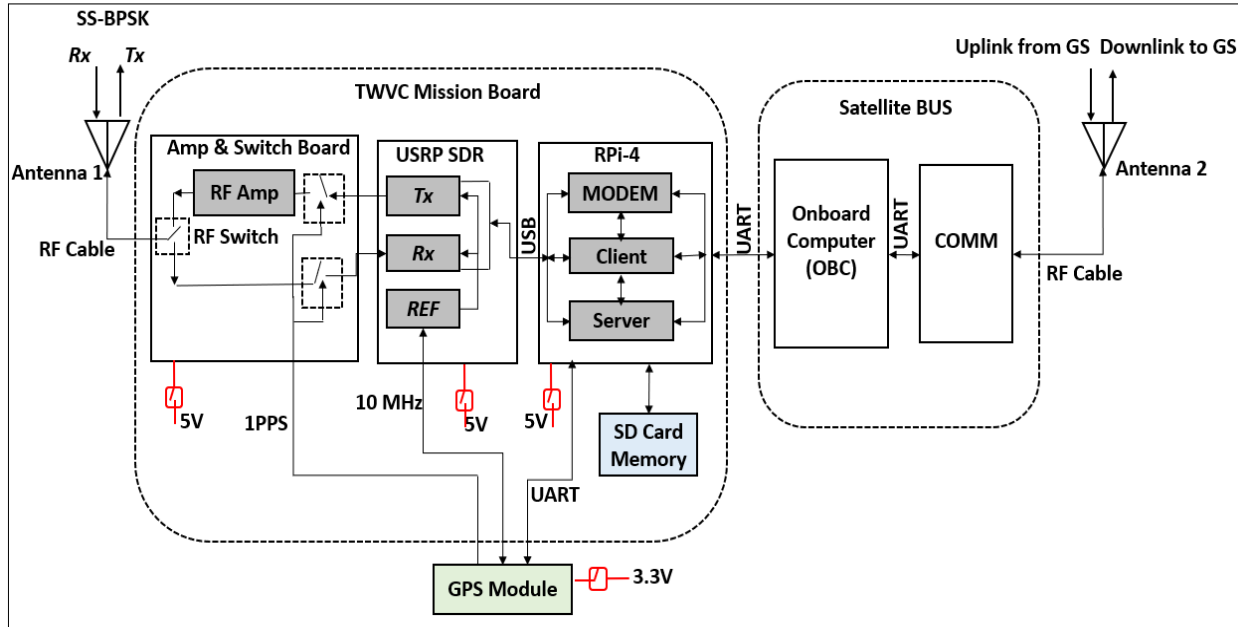


Figure 22. System design configuration block diagram

The satellite bus can be a generic one. The interface between the mission payload and the satellite bus is simply made of power lines (5 V and 3.3 V) and a digital data line universal asynchronous receiver/transmitter (UART). The satellite bus turns on the mission payload based on either the command uplink from the ground station or through reserved commands in the satellite's onboard computer. The mission data will be downlinked to the GS via the satellite bus. The water vapor mission measurement board is composed of the universal software radio peripheral (USRP) SDR model B205 mini-i, the RPi 4 model B, the amplifier and RF switches board, a GPS module, and the antenna (Antenna 1).

Antenna 1 serves as the primary channel of communications. This channel is only used to transmit (Tx) and receive (Rx) SS ranging signals. Meteorological dual frequency bands ( $f_1 = 400.15$  MHz and  $f_2 = 460.00$  MHz) with a frequency gap of 59.85 MHz are reconfigured and used for SS transmission and reception. The SDR transceiver is used to transmit and receive the SS signal. To realize mission success in orbit, especially when the distances between the satellites

is large, an RF amplifier is required to amplify the transmitted signal. The RPi 4 conducts digital signal processing on the mission data and is used to control the SDR parameters using GNU Radio software (v3.8.2.0). A GPS module is mounted on each satellite and at the ground stations. The GPS module provides the location, time, a 10 MHz clock, and a one pulse per second (1PPS) signal. The location and time data are carried along with the SS signals. The 10 MHz clock eliminates the SDR's clock and instrument errors at both the transmitting and receiving SDRs. The 1PPS time reference markers are superimposed on to the incoming and outgoing signals through the RF switches.

When the GPS modules at both the receiving and the transmitting ends are synchronized, signal propagation time delay in the ISL network can be derived based on the 1PPS time markers. Finally, TWVC mission data are deduced from the signal time delay. When the SDR is in reception and transmission modes, the power consumption for this mission subsystem is estimated as 2.81 W and 8.50 W, respectively. Having one SDR to perform both the Rx and Tx of SS signals at different frequencies, not only saves satellite power but also mass and volume occupied by the mission subsystem compared to systems with multiple radio devices performing the same function.

### **3.2.3 Mission Execution Sequency**

Figure 23 sequence diagram elaborates on the mission execution steps. As indicated on the sequence diagram for mission execution, the following steps are executed during the mission operation.

1. Scheduled uplink command signals are sent from ta network of GS using ground station to satellite (GaS) network to turn on the mission payloads of the satellites. The satellite onboard computer (OBC) has two digital inputs/outputs (DIO), which enable turning ON and OFF RPi and SDR hardware through a 5 V power line. The booting processing of SDR and RPi was observed to take approximately 1 min each.
2. The RPi runs GNURadio software to transmit and receive data. The frequency reconfiguration software that manipulates transmission and receiving frequency modes of the SDR is also housed inside the RPi. Data processing and calculation of TWVC data is done inside the RPi. RPi receives and save the GPS data. The GPS data is filtered through a python program to capture only time and position data. The GPS module operates using 3.3 V of power and is also enabled through DIO from the OBC.

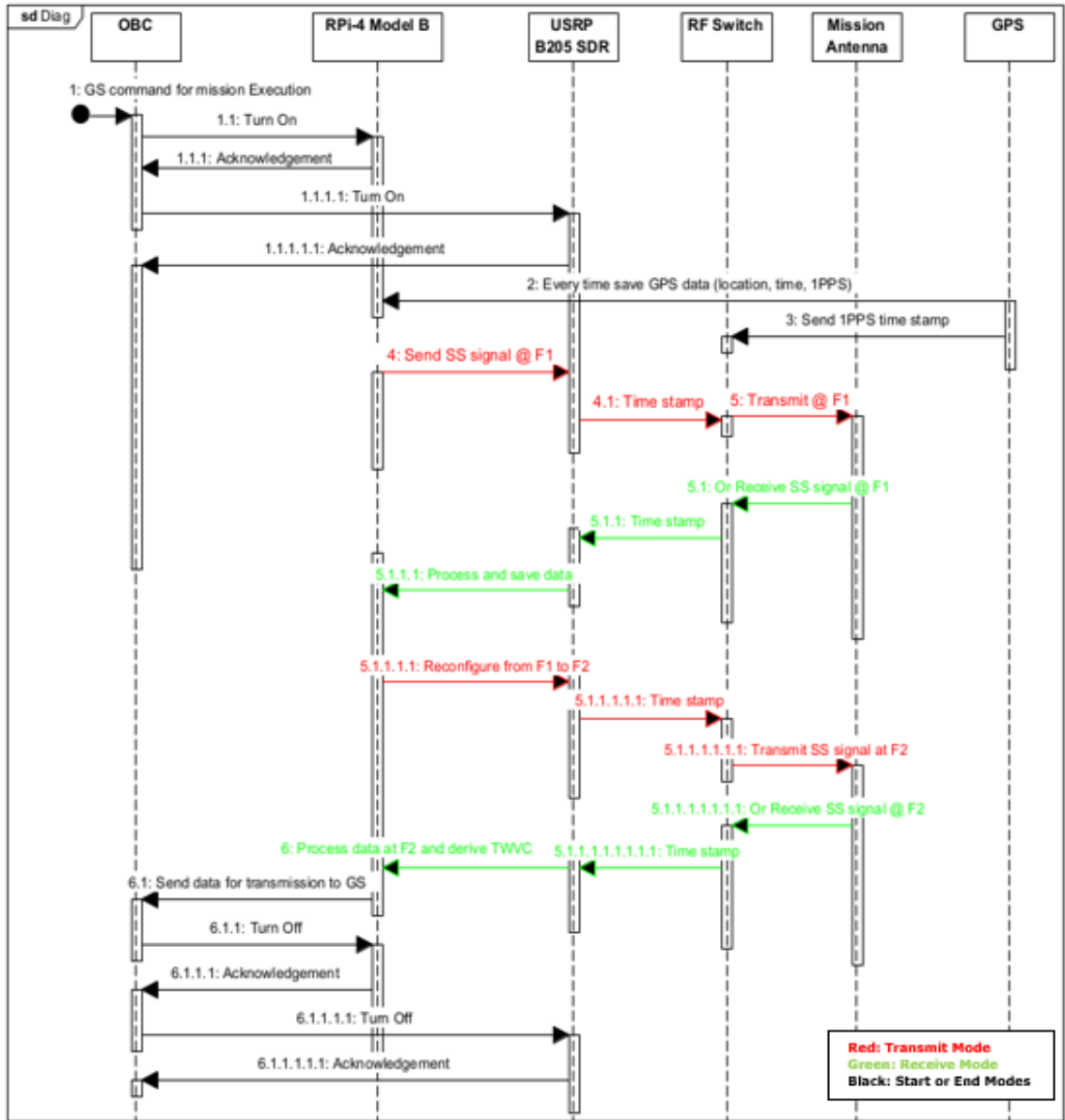


Figure 23. Mission execution scenario.

3. In transmission mode, SS UHF signals are transmitted at frequency  $f_1$  MHz via the primary channel.
4. In receiving mode, the SS transmitted packets are received at frequency  $f_1$  MHz at the antenna. The received SS signals will have time delayed data due to TWVC and TEC. Each data frame of the received signal is superimposed with 1PPS GPS signal required to facilitate time delay measurement useful in determining the TWVC and TEC. The propagation delay is deduced by synchronizing the received and transmitted clock signals.

5. The signal (In-phase and quadrature (IQ) samples) at the SDR is demodulated in RPi using GNURadio software and saved as wave file and text data.
6. The saved WAV file data is processed onboard the satellite. Analysis of the saved .wav file includes extracting the relative position of the UTC 1PPS signal and the beginning of the packet to calculate the reception time of the signal with a time resolution of (1/sampling frequency) of the received signal.
7. SDR is reconfigured in at least a second interval to alter the frequency parameter from  $f_1$  MHz to  $f_2$  MHz.
8. The process (1) to (6) is repeated
9.  $f_1$  and  $f_2$  data are processed in RPi to distinguish TWVC and TEC.
10. TWVC data is finally deduced. The processed data is transferred to the OBC. During satellite pass at a GS, the data is downlinked to the nearest ground station in the GS network for analysis.
11. The data is disseminated and added to atmosphere's geophysical databases for climate and weather prediction modelling.

### 3.2.4 Mission Success Criteria

The mission execution onboard the satellites shall fulfill the following mission success criteria in Table. 6.

*Table 6. Mission success criteria*

Mission Success Criteria	
Current Success Requirements	Next Success requirements
1. Demonstration of ISL communication network with at least two satellites.	1. Demonstrate ISL with more than two satellites at temporal and spatial resolutions of 5-15min and 20-4600 km, respectively.
2. Achieve frequency translation between two satellites using dual bands	2. Demonstrate frequency translation to multiple satellites with multiple frequencies
3. Achieve mission at one mega sample per second (1MSPS)	3. Achieve mission > three mega sample per second (3 MSPS)
4. Deduce point mapping of TWVC data from TEC data.	4. 3D mapping of TWVC and TEC
5. Single orbital plane	5. Multiple orbital planes

### 3.3 Proposed Ground Station Design Configuration

The ground station was proposed for future work but has not been implemented in this research. SPATIUM satellites utilized an approximate similar configuration. The only difference is that in this research a multi-channel SDR is required at the GS. Elucidated in the diagram in Figure 24, the primary channel configuration is used to execute the TWVC mission, and the secondary channel is for satellite bus uplink and downlink.

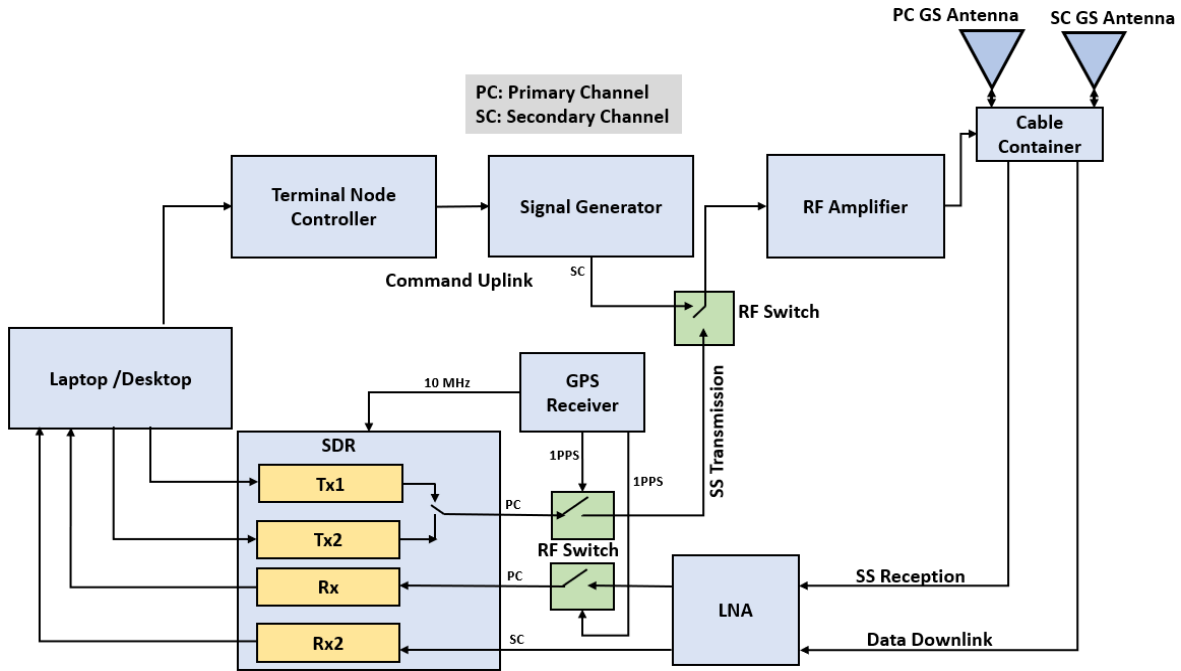


Figure 24. Ground station setup

The ground station laptop/desktop computer contains satellite operation software to uplink commands and download data. The computer also contains the software to transmit SS signals or to receive and process the SS signals for analysis.

#### 3.3.1 Primary Channel Configuration

In the uplink phase, the SS-BPSK signals are transmitted by the SDR transceiver. The SDR can transmit at two frequencies (Tx<sub>1</sub> and Tx<sub>2</sub>) The GPS 1PPS timestamp is superimposed on the SS signals and will be utilized as a benchmark for the received signal to identify the signal shift. The signal is sampled at the time of the rise of 1PPS on the GS side, and on the satellite side, it is sampled at the start of 1PPS. RF switched are also used to superimposed the 1PPS signals. During downlink phase, SS data is received at the antenna, amplified by the LNA, time stamped by the

GPS, demodulated by the SDR Rx, acquired and processed at the GS laptop and finally TWVC is calculated. The time difference between the received and transmitted SS signals gives the propagation time delay caused by TWVC.

### 3.3.2 Secondary Channel Configuration

This setup is generic. In the uplink case, the data is formatted and assembled by the terminal node controller (TNC) for efficient transmission. A signal generator (SG) is used to transmit the uplink commands via the antenna. RF power amplifier is used to amplify the transmitted signal. In the downlink case, the GS retrieves processed mission data from the satellites at the antenna, amplified by the LNA, demodulated with SDR Rx2 using SDR Sharp software and laptop sound card. The data is analyzed and disseminated for space weather meteorological uses.

### 3.3.3 GS Data Budget Computation

Usually, for each day of satellite operations, only 3 to 4 satellite passes have high elevation angles above +30° degrees. The following assumptions were made in estimating the data budget at each GS in a network as shown in Table 7.

#### Assumptions

1. Two satellites in ISL
2. UHF GS
3. Four or fewer satellites pass a day
4. Elevation angles of +20° degrees.
5. Each GS has 90% operation efficiency.
6. Successful uplinks in 5-8 minutes of the 10 minutes of the mission duration (50 to 80 % duty cycle).
7. The data rate of +4.8 kbps.

*Table 7. Data budget*

Mission Period (min)	Frequency Bands	Bitrate [Kbps]	Total Bits [Mb]	Total Bits @90% margin	Average Data Size [Mb]	Passes

5	UHF	4.8	1.44	0.98	0.60	4
6			1.73	1.56		4
7			2.02	1.81		3
8			2.30	2.07		3

Considering the above listed assumption, it is estimated that in four passes, at least 0.6 megabytes of data are downloaded daily at each ground station using UHF frequency. The more the number of ground stations in the network, the more data that can be downlinked.

## CHAPTER 4

### INTERSATELLITE LINK RANGING AND CONSTELLATION MANAGEMENT

#### 4.1 Overview

In this chapter, state of art intersatellite link (ISL) communication networks are discussed. In this research an improved version of ISL network based on SDR technology in a configuration of two satellites is implemented. The SS coding scheme utilized in the ISL network is explained. The ISL addressed issues includes effective management of large constellation of satellites, satellite deployment, communication, long-term maintenance, and ensuring the accuracy and reliability of mission measurement data. Furthermore, frequency manipulation algorithms are proposed to ensure exchange of data between satellites in the ISL network, accuracy of mission data, and to distinguish TWVC from TEC. Furthermore, this section gives some comparison of the proposed frequency manipulation methods (modified XML-RPC and TCP/IP) with existing methods, discussing advantages, drawbacks, and potential scenarios where each approach is most suitable.

#### 4.2 Intersatellite Link Ranging

Intersatellite Link (ISL) communication is a critical component of modern satellite operations, facilitating the seamless exchange of data among satellites deployed in different or same orbital trajectories [98,99]. Its pivotal role in satellite missions transcends multifarious domains, encompassing scientific studies, terrestrial surveillance, navigational undertakings, and a spectrum of other applications. The contemporary era has witnessed significant advancements in intersatellite communication networks, with notable applications in missions aimed at the determination of atmospheric water vapor and total electron content.

Figure 25 illustrates the graphs with current statistics of deployed ISL satellites in orbit over the last two decades. Since 2000 until 2019 every few satellite constellations with ISL ranging were lunched. From 2020 until present, there was a more than 10-fold rapid increase on the number of ISL satellites. Starlink and OneWeb are the dominating constellation of satellites; however, their missions are typically for internet of things (IoT), internet coverage, broadcasting, telecommunications and for Earth observation missions. The satellite constellations are usually



implemented with satellites of masses above 100 kg, mainly between 201 kg to 300 kg.

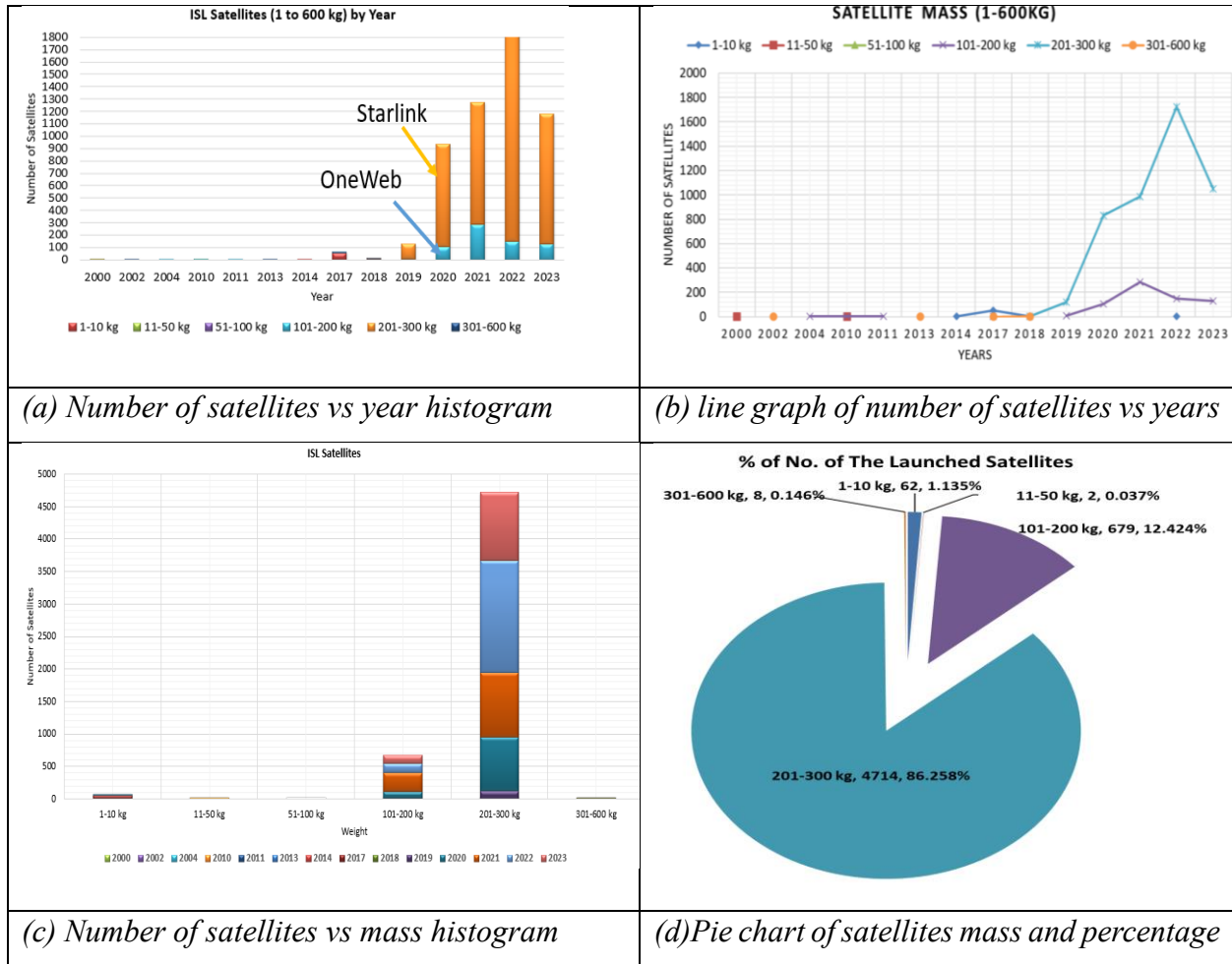


Figure 25. ISL deployment statistics.

Table 8 shows some of the satellite mission that used ISL communication. SNAP-1, PRISMA and EDSN satellites utilized UHF frequency bands but for different mission purposes to TWVC. For related studies, GRACE, QB-50 and GRACE-FO satellite constellations has been implemented using S-Band ISL frequencies. However, these satellites did not investigate the variation of atmospheric water vapor.

Table 8. Intersatellite missions between 2000 and 2023

Mission	No. of SAT	Mass	ISL Band	Range (km)	Mission purpose	Lunch Year	Ref
SNAP-1	2	6.5/49	UHF	2	Tech Demo	2000,	[100]
GRACE	2	480	S	220	Earth's Magnetic field	2002	[100]

PRISMA	4	145,50	UHF	10 m - 5 km	Formation Flying	2010 success	[101]
CanX 4&5	2	5	S	5	PFF demo	2014, success	[102]
EDSN	8	2	UHF	20	SmallSat Networks	2015, fail	[103,104]
QB-50	50	2,3	S	-	Thermosphere Exploration	2016	[105]
Diamond	3	6	S	-	ISL	2017,	[102]
PROBA-3	2	320, 180	S	144m	Formation flying	2017	[106]
S-NET	4	9	S	100	ISL	2018	[102]
CPOD	2	3	S	25	Rendezvous	2020	[102]
eLISA	3	tbd	UHF		Optical/Laser ISL	2028	[100]
MAGNAS	28	210, 5	UHF	-	Geomagnetic Field	tbd	[100]
GRACE- FO	2	600	K/Ka	220	Gravity and Climate Experiment	2018	[107]

State of art technology which can and other which has been applied for weather and climate studies includes the free space optical/ laser communication (FSOC), radio occultation methods, frequency manipulation techniques, swam formation flying, and software defined radio based ISL technology.

### **1. Frequency Manipulation Techniques: GNSS satellites and the GRACE-FO Mission**

Frequency manipulation of GNSS signals has been employed to measure the atmospheric WV delay, which is then used to derive IWV and PWV. However, the GNSS high frequencies are less prone to the influence of TEC and TWVC, since GNSS satellites are typically designed for navigation. The GRACE-FO (gravity recovery and climate

experiment follow-on) mission utilizes this method to determine changes in Earth's water distribution, including changes in atmospheric water vapor content [108]. However, GRACE-FO (two satellites) was not primarily designed for measuring water vapor content in the atmosphere, but it can indirectly provide some information related to water vapor content and its effects on Earth's mass distribution [107]. The frequency manipulation in GRACE-FO microwave K-bands between 24.0 to 24.3 GHz relates to the Doppler shift of microwave signals transmitted between the two satellites. As the satellites move through the Earth's gravitational field, the distance between them changes due to variations in gravity. This causes doppler shift to the microwave frequency which can be measured. The limitations are the GRACE-FO measurements are sensitive to changes in Earth's mass distribution caused by a variety of factors, including changes in groundwater, ice sheets, and ocean circulation. Disentangling the specific effects of water vapor content from these other factors can be challenging. Furthermore, GRACE-FO data has a relatively coarse temporal and spatial resolution. It provides monthly averages and large-scale measurements, which may not capture fine-scale variations in atmospheric water vapor content. GRACE-FO measurements primarily reflect changes in water vapor content within the entire atmospheric column. It does not provide vertical profiles of water vapor at different altitudes, which are valuable for various applications. Therefore, while GRACE-FO offers precise measurements of changes in Earth's gravitational field, accurately quantifying the specific contribution of water vapor content to these changes remains a complex and challenging task.

## **2. Swarm Mission Formation Flying ISL**

The three Swarm satellites are placed in a formation with different altitudes and orbital characteristics [109]. ISL technology allows these satellites to communicate with each other and coordinate their positions precisely. This formation flying is crucial for TEC measurements, as it enables simultaneous observations at different altitudes and positions. To measure TEC, the Swarm satellites use dual-frequency GNSS receivers to acquire GNSS (such as GPS and Galileo) signals as they pass through the ionosphere [110]. Each Swarm satellite is equipped with GNSS receivers capable of receiving signals from GNSS satellites. These GNSS receivers also use ISL technology to share precise timing and

positioning information between the three satellites. By simultaneously observing GNSS signals from different positions in space (the three Swarm satellites), it is possible to calculate TEC values with high accuracy. The ISL communication ensures that the GNSS receivers on the Swarm satellites are synchronized and can precisely time the arrival of GNSS signals. The TEC data collected by the Swarm satellites are transmitted to ground stations on Earth via the ISL communication system. This data is then processed and used to create TEC maps and profiles, providing valuable information about the ionospheric electron density. However, the Swarm formation flying technique suffers the limitation of GNSS receivers. Maintaining the precise formation of three satellites in orbit requires continuous monitoring and adjustments. Deviations in their relative positions and timing can occur due to various factors, including gravitational perturbations, scintillations in the Earth's gravitational field and solar radiation pressure. These deviations necessitate frequent orbit maintenance maneuvers, which consume onboard fuel and limit the mission's operational lifetime. The Swarm formation configuration restricts the spatial coverage of the mission. While it provides simultaneous measurements at different altitudes and positions, it may not cover all regions of interest uniformly. This limitation can impact the mission's ability to provide comprehensive data for scientific studies. Also, precise time synchronization is essential for data fusion and accurate scientific measurements. Maintaining precise time synchronization among the Swarm satellites can be challenging, particularly as they orbit the Earth at different altitudes and velocities. Any timing errors can affect the quality of data collected and the accuracy of scientific results.

### **3. Radio Occultation (RO): COSMIC-2 Mission and the GNSS satellites**

RO involves GNSS satellites transmitting signals from high orbital altitudes, with LEO satellites receiving and analyzing the signals to obtain profiles of signal refractions, which can be employed to derive WVC. The COSMIC-2 mission is a satellite-based program designed for a wide range of scientific observations, including the derivation of the parameters of the atmospheric parameters including WV [111]. The COSMIC-2 mission, comprising a constellation of six LEO satellites equipped with GNSS receivers, in different orbital planes, employs RO to determine atmospheric water vapor profiles. The LEO satellites in the COSMIC-2 constellation moves between a GNSS satellite and the

Earth's limb (the boundary between space and the atmosphere). As the GNSS signal passes through the atmosphere at this critical angle, it undergoes bending or refraction which can be precisely calculated. Atmospheric WV affects this refraction GNSS signals. By analyzing the refraction angles of the GNSS signals, COSMIC-2 derive information about temperature, pressure, and crucially, water vapor content at different altitudes. However, for the COSMIC-2 mission there are regions where ISL-based RO measurements are not feasible due to the relative positions of the satellites and GNSS satellites. The regions include Polar regions where the density of GNSS satellites in view can be lower [112], leading to fewer occultation events. Also, in the equatorial belt [113], the inclination of LEO (Low Earth Orbit) satellites like those in the COSMIC-2 constellation may limit occultation events with GNSS satellites that are primarily distributed at higher latitudes. The relative geometry may result in fewer RO measurements. Furthermore, over large bodies of water, the density of GNSS signals can be lower than over land, particularly in remote oceanic areas [114]. This can reduce the number of occultations and limit the coverage of RO data in these regions. Moreover, there are specific periods during a satellite's orbit when it enters the solar or lunar exclusion zones. During these times, GNSS signals may not be available for occultation measurements, impacting data collection. Those are the challenges of using ISL based RO with GNSS satellites.

#### **4. Optical Communication (Free-Space Optical Communication, FSOC): Aeolus Mission**

Optical communication can be used for ISL communication. There are no missions where it has been used specifically for water vapor derivation. The European Space Agency's (ESA) " AEOLUS " mission employed FSOC to measure atmospheric wind profiles by analyzing the backscattered laser signals, enabling the determination of water vapor concentrations at different altitudes [115,116] but not in an ISL network. AEOLUS carries a high-power laser instrument called the Atmospheric Laser Doppler Instrument (ALADIN) that emits laser pulses into the atmosphere. However, using ISL optical communication is subject to various atmospheric disturbances, such as turbulence and scattering, which can affect the quality of the received signals. Also, precise alignment of the laser beam with the receiving station is crucial for efficient data transfer. Maintaining

this alignment during satellite movement and under changing atmospheric conditions can be challenging. The efficiency of the intersatellite link's optical components and the need to minimize signal degradation during long-distance transmission are of significant concerns. Using ISL optical communication for missions like AEOLUS is challenging because AEOLUS traverse the Earth using sun-synchronous polar orbit, which means it has varying line-of-sight angles to ground stations during its orbit. This dynamic orbital behavior requires adaptive tracking and communication strategies. On the ground, receiving and processing the data from AEOLUS is a complex task. Ground stations need advanced equipment and data processing capabilities to handle the unique characteristics of laser-based communication. And finally, developing and maintaining a robust intersatellite communication system based on this optics technology can be costly. Striking a balance between mission requirements and budget constraints is an ongoing challenge.

Another mission that uses the Laser communication systems is the Laser Geodynamics Satellite (LAGEOS) [117]. In this mission Laser is used to determine TEC by measuring the delay and phase variations of laser signals as they traverse the ionosphere. The Laser Geodynamics Satellite (LAGEOS) and LAGEOS-2 missions incorporate retroreflectors for laser ranging, enabling measurements of TEC and aiding in geodesy and Earth's gravitational field studies. However, same challenges as the FSOC have also been experiences in the LAGEOS missions.

## **5. SDR Technology: Proposed ISL Mechanism for TWVC and TEC Measurements**

While SDR technology has been used in various satellite missions for communication and data processing, the specific application of SDR for water vapor content measurement is not a prominent feature of any major satellite mission [43,91,118]. Thus, currently there is no widely known or widely used satellites that primarily employed SDR frequency manipulation techniques specifically for the measurement of TWVC. In this research SDR ISL mechanism with frequency manipulation has been proposed. This technique is robust in that it combines typical critical components of frequency manipulation, Laser, RO and formation flying to make a more reliable ISL network of a satellite constellation. SDR has been opted and demonstrated as most viable based on the following aspects:

- i. Versatility: Using SDR the digital signal processing component of communication was implemented in software instead of specific hardware. This significantly reduced the mass and volume of the satellites used in this proposed method.
- ii. Flexibility and Reconfigurability: The flexibility and reconfigurability of SDR has been adopted to manipulate the SDR frequencies remotely. This also helped in the automation of frequency manipulation remotely and smooth frequency shifting without physical tuning of the hardware.
- iii. Wider Spectrum: Since SDR frequencies spans between 70 MHz 6 GHz, only one SDR was used to demonstrate the frequency manipulation of the two frequencies (400.15 MHz and 460 MHz) instead of having multiple radio hardware's doing the same work. This effectively reduced the mass, power, volume and complexity of the system.
- iv. Cost-Efficiency: Low-cost SDR platforms, based on off-the-shelf components, significantly reduce hardware costs compared to specialized hardware implementations. This affordability was particularly beneficial for this research prototyping, and practical ground demonstrations.
- v. Reprogrammable and upgradable modular architecture: SDR systems used can be updated and upgraded through GNU Radio software changes, eliminating the need for hardware replacements. This extends the operational lifetime and adaptability of the system.

#### **4.2.1 Implemented ISL network with SS- BPSK Coding Scheme**

Figure 26 shows a simplified test bed configuration used to demonstrate ISL network for SS transmission, 1PPS time stamping, and frequency reconfiguration between two satellite payloads. The ISL network operates as a half-duplex system. The satellites operate in two modes for the transmission and reception of SS signals. In Figure 26, Sat A is in transmission mode and Sat B is in reception mode. In addition to the system design configuration in Figure 22, a delay pulse generator was incorporated at the receiving payload to simulate propagation delay ( $\delta T$ ) due to the TWVC and TEC in orbit. As a result, the system functionality of deducing atmospheric water vapor and total electron content delay was demonstrated as explained in this chapter. Additionally, 30 dB attenuators were used instead of power amplifiers to decrease the transmitted signal power

in order to prevent receiving SDR damage or interference from other communication networks. A personal computer (PC) was utilized on one end of the network to serve as the generic satellite bus system for monitoring and acquiring processed data.

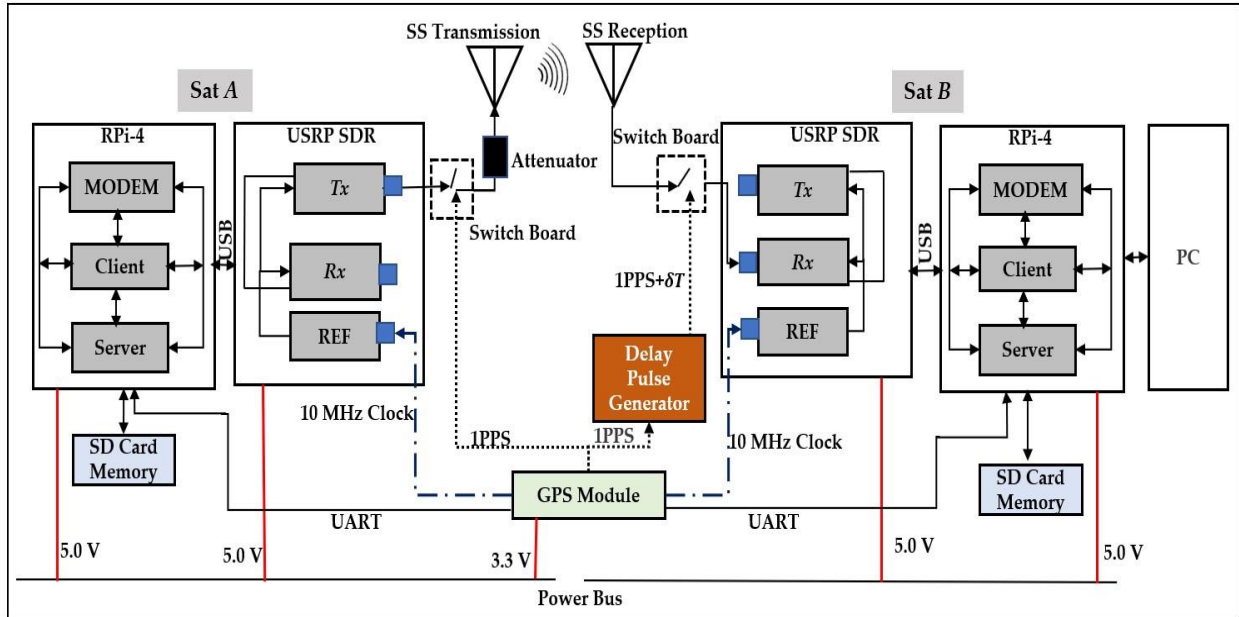


Figure 26. ISL network test bed.

#### 4.2.1.1 SS-BPSK Transmitter

The software for SS-BPSK transmission was implemented on each satellite in the ISL network utilizing GNU Radio and Python programming language [93,119]. The SS signal carries the time and location data of one satellite to another which is needed when computing propagation time delay due to the influence of water vapor and total electron content. Information was transmitted from Sat A (SS-BPSK transmitter) to Sat B (SS-BPSK receiver) in the ISL network. As illustrated in Figure 27, the SS-BPSK transmitter is where the SS data packets are transmitted from the vector source block over a wider bandwidth at a bit-rate of 250 bits per second, with 1 bit having 250 chips, and 1 chip recurring at every 16  $\mu$ s. The SS signal is composed of the header, satellite ID, GPS time, and location information as well as the footer. The header and the footer are identifiers which show the beginning and the end of each packet of data conveyed in the communication network. For simulation purposes, the transmitted information was composed of header information: F; satellite identification (Sat ID): 01; GPS data of time (s): 04; latitude ( $^{\circ}$ ): 33.53513942; longitude ( $^{\circ}$ ): 130.50418427; altitude (m): 46; and footer information: A. The positive polarity of the latitude and longitude represent north and east positions of the GPS's



geodetic coordinates, respectively.

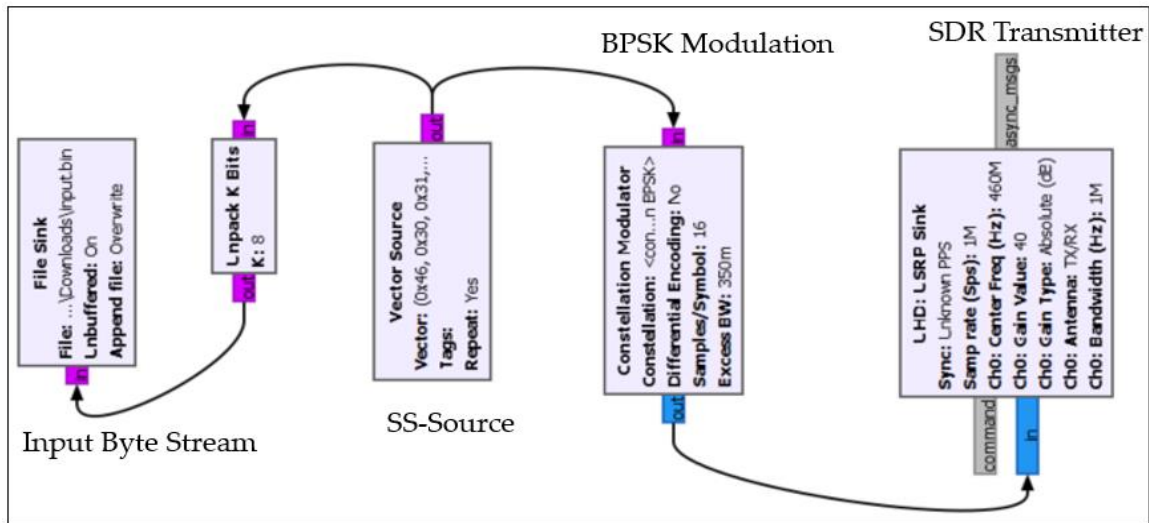


Figure 27. SS-BPSK transmitter at Sat A.

Likewise, this would indicate the south and west coordinates of the GPS latitude and longitude position data in the case of negative polarity, respectively. The precision the longitude and latitude data were all obtained with  $\pm 1.11$  mm location accuracy. The packet format of the GPS data is described in Table 9 below.

Table 9. SS signal data format

Header	Sat ID	Time (s)	latitude (°)	longitude (°)	Altitude (m)	Footer	
F	01	04	33.53513942	130.50418427	46	A	00
1 byte	2 bytes	2 bytes	11 bytes	12 bytes	2 bytes	1.25 byte	

The transmitted 250 bits of information received represent header information (1 byte), Sat ID (2 bytes), time (2 bytes), latitude data (11 bytes), longitude (12 bytes), altitude (2 bytes) and footer (1.25 byte). The data in text was converted to hexadecimal data (0x46, 0x30, 0x31, 0x30, 0x34, 0x33, 0x33, 0x2E, 0x35, 0x33, 0x35, 0x31, 0x33, 0x39, 0x34, 0x32, 0x31, 0x33, 0x30, 0x2E, 0x35, 0x30, 0x34, 0x31, 0x38, 0x34, 0x32, 0x37, 0x34, 0x36, 0x41) that was transmitted in binary form. The SS source software was implemented to add two more bits (00) to the footer in order to have 250 bits of data transmitted in every second. The original SS data was saved using the file sink block at Sat A for comparison with the received data at Sat B. The transmitted sequence with GPS data was then modulated with BPSK modulation using a constellation modulator. The modulated

data was transmitted with SDR through the USRP Hardware Driver (UHD) sink block. For demonstration purposes sample rates of 1 mega sample per second (MSPS) and 500 kilo samples per second (KSPS) and two frequencies (400.15 MHz and 460.00 MHz) were utilized interchangeably through tuning of the digital signal processing parameters.

#### 4.2.1.2 SS-BPSK Receiver

Figure 28 shows the implemented GNU Radio-based SS-BPSK receiver software.

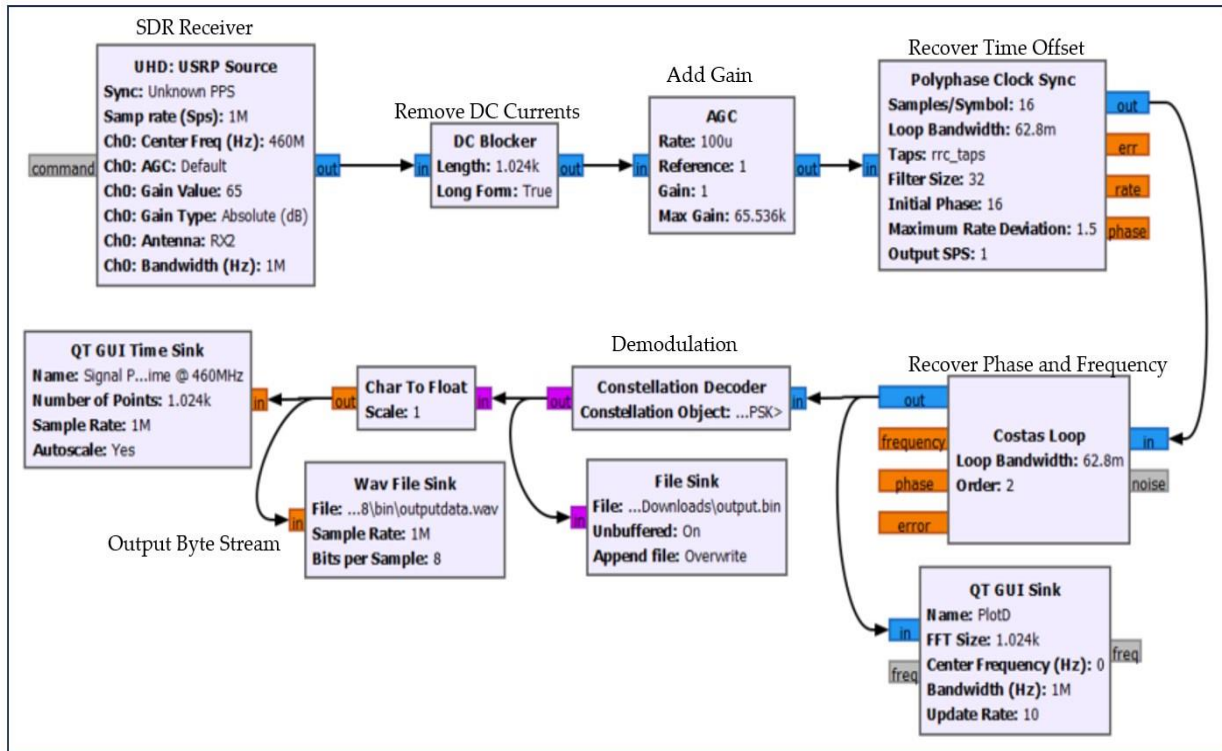


Figure 28. SS-BPSK receiver at Sat B.

The receiver recovered the signal through the UHD: USRP source block. The DC blocker then eliminated the transceivers' DC offset noise from the signal. After that, the signal went through a high-performance automatic gain control (AGC) unit which regulated the increase in signal amplitude from the original to the amplified state. Synchronization of the transmitter and receiver time offsets was carried out at the polyphase clock sync block. The Costas loop corrected the phase and frequency offset as well as recovering the carrier. Figure 29 is the recovered transmitted data in binary form. At the receiver the two bits (00) added to the footer by software for efficient transmission were eliminated.

Address	00	01	02	03	04	05	06	07	08	09	0A	0B	0C	0D	0E	0F
00000000	01	00	01	10	00	11	00	00	00	11	00	01	00	11	00	00
00000010	00	11	01	00	00	11	00	11	00	11	00	11	00	10	11	10
00000020	00	11	01	01	00	11	00	11	00	11	01	01	00	11	00	01
00000030	00	11	00	11	00	11	10	01	00	11	01	00	00	11	00	10
00000040	00	11	00	01	00	11	00	11	00	11	00	00	00	10	11	10
00000050	00	11	01	01	00	11	00	00	00	11	01	00	00	11	00	01
00000060	00	11	10	00	00	11	01	00	00	11	00	10	00	11	01	11
00000070	00	11	01	00	00	11	01	10	01	00	00	01	00			

Header Information: 01 00 01 10 (from address 00000000)

Footer Information: 01 00 00 01 00 (from address 00000070)

Received Information: (indicated by a bracket on the right side of the data rows)

Figure 29. Recovered SS-transmitted GPS data at Sat B.

By using a decoding software [120] to transform the binary data to the original information, the received binary data conformed to the transmitted SS signal data (F, 01, 04, 33.53513942,130.50418427, 46, A) as shown in Figure 30.

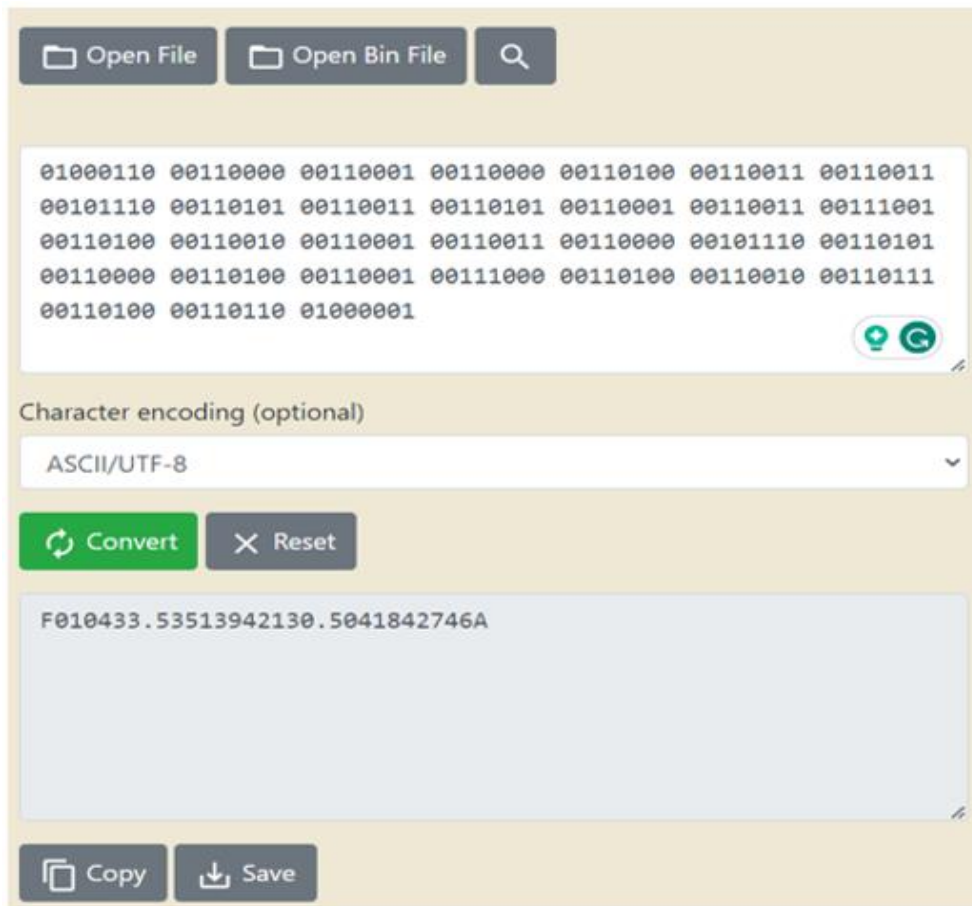


Figure 30. Decoded SS-transmitted GPS data at Sat B.

The implemented system could recover the transmitted signal from Sat A to Sat B and vice versa at both 400.15 MHz and 460.00 MHz in both cases, with and without signal delay. This demonstrated the feasibility of ISL communication where each satellite can transmit or receive location and time data to or from other satellites in the network. In reception mode the satellites could decode and understand the location data of other satellites. As a result, the ISL network requirement was proven

#### 4.2.1.2.1 SS Frequency Detection at the Receiver

At the receiver, the SS-BPSK signal spread over a wider bandwidth of frequencies was received at both 460 MHz and 400.15 MHz in wireless ISL network. Figure 31 (a) and (b) show the spectrums of the signals received at the SDRs in ISL networks.

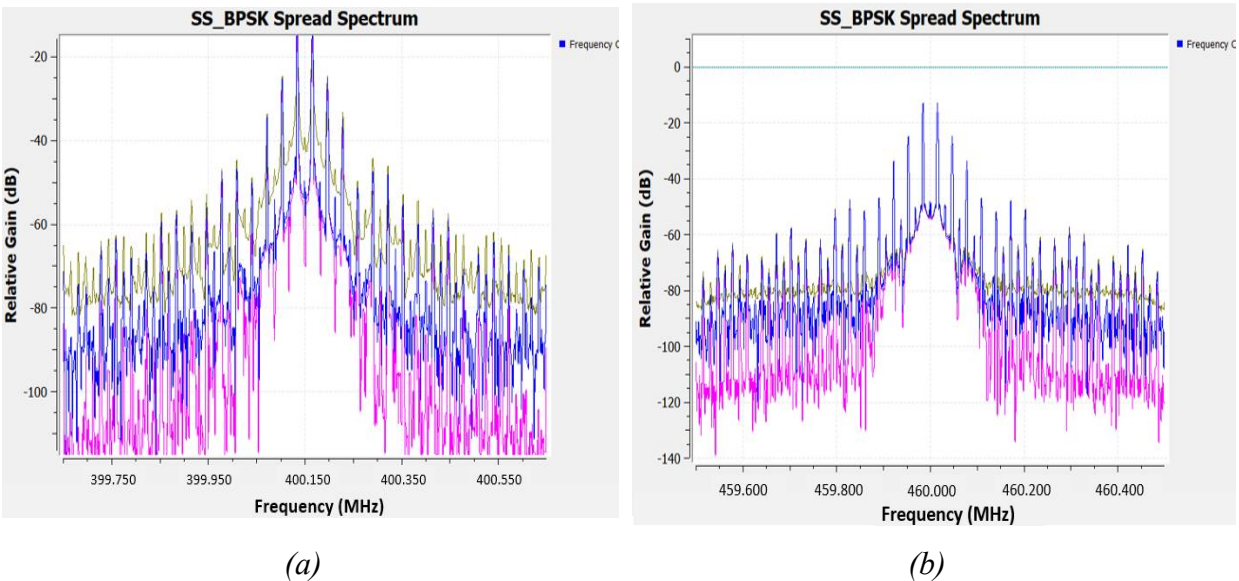


Figure 31. (a) Frequency spectrum at 400.15 MHz: brown: upper bound, pink: lower bound, blue: average spectrum; (b) Frequency spectrum at 460 MHz: brown: upper bound, pink: lower bound, blue: average spectrum

Spread spectrum signal structures that spread a normally narrowband information signal over a wideband of frequencies were observed. The USRP SDR gains were adjusted between 40 dBi and 76 dBi for the SDR receiver and between 40 dBi and 90 dBi for the transmitter. To avoid damaging the SDR, maximum power received at the receiver was maintained below 0 dBm as recommended by the SDR transceiver datasheet.

#### 4.2.1.2.2 SS BPSK Received Signal Constellations

The constellation of SS-BPSK (Figure 32) was recovered at the receiver after correction of time, frequency, and phase offsets.

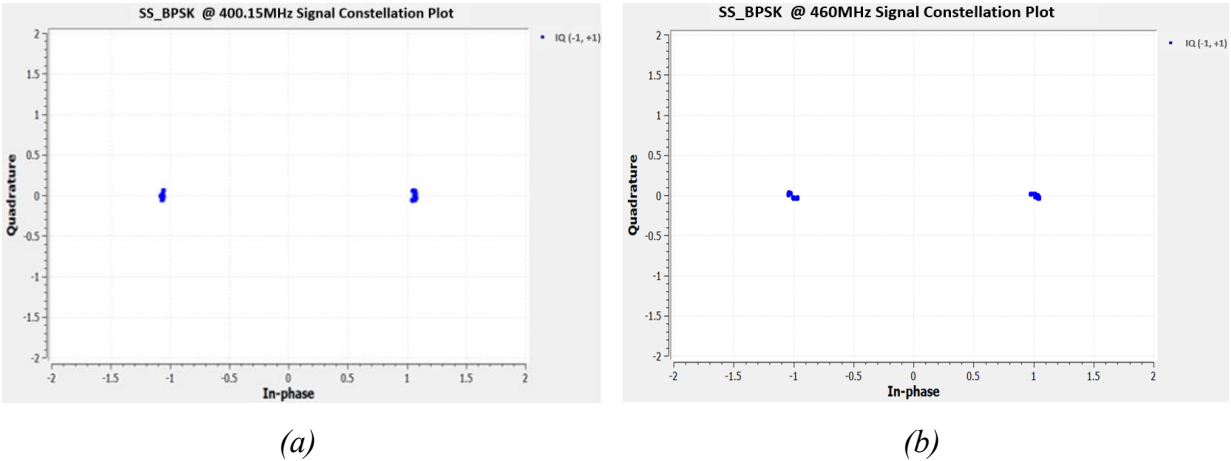
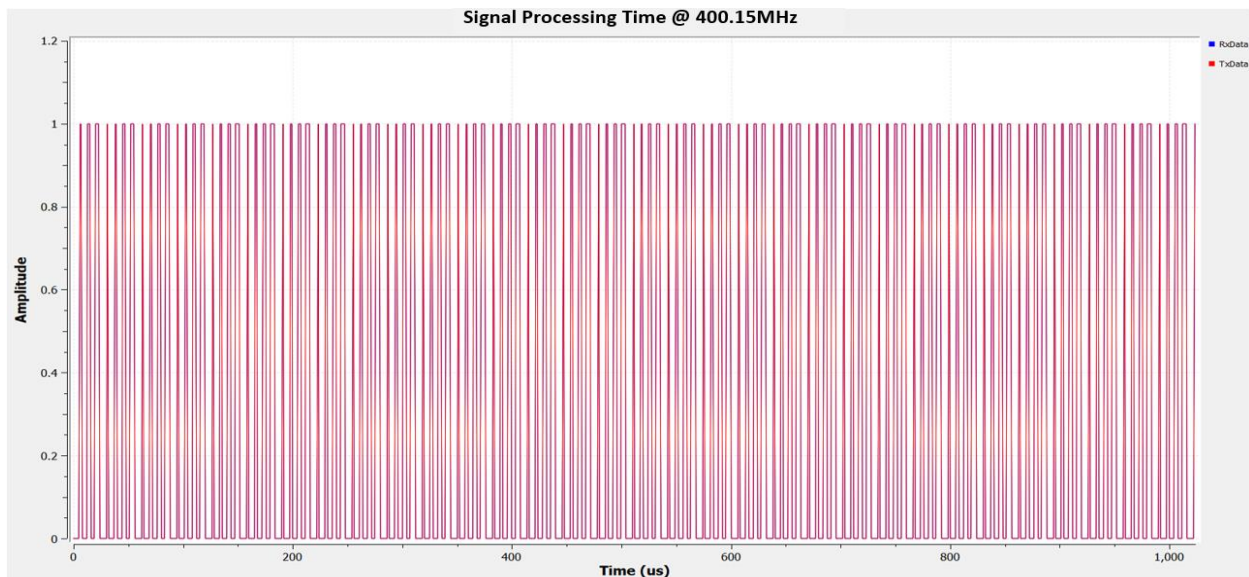


Figure 32. (a) Constellation at 400.15 MHz; (b) Constellation at 460 MHz.

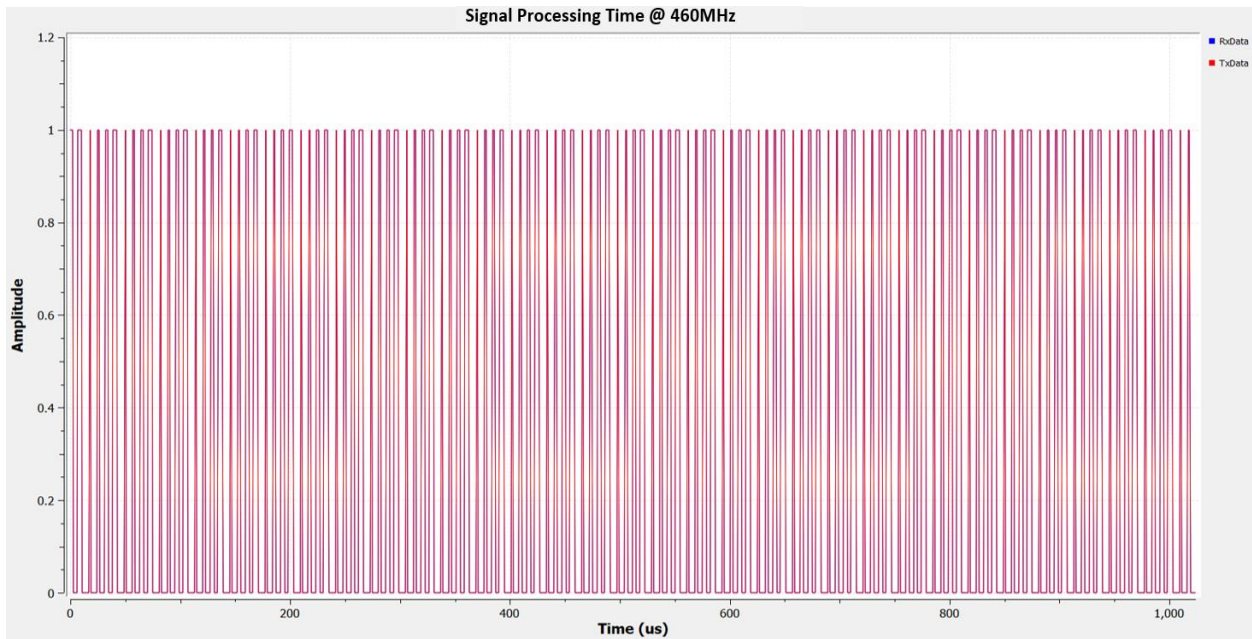
The inphase and quadrature (IQ) BPSK binary symbols -1 and 1, with 180 degrees of phase difference were observed for both 400.15 MHz and 460 MHz frequencies

#### 4.2.1.2.3 SS BPSK Time Oscilloscopes

The transmitted and the received data sets collected at the transmitter and receiver were matched in the time domain. The time domain oscillographs in Figure 33 (a) and (b) show the perfect match of signal processing in 1s (1000 $\mu$ s).



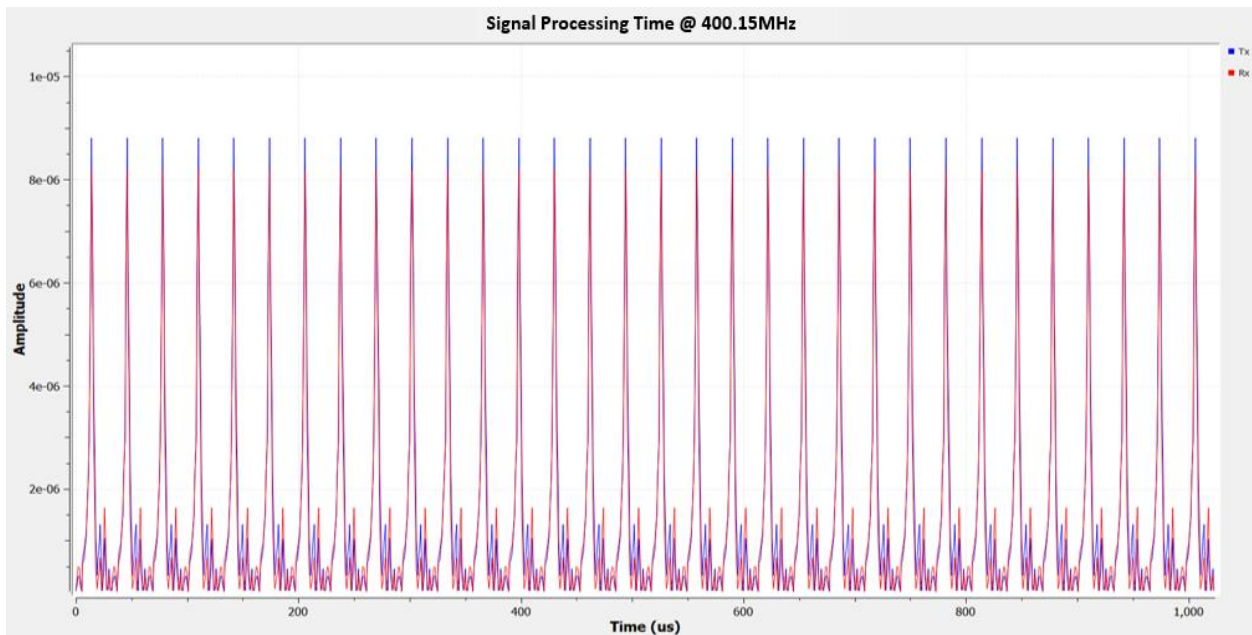
(a)



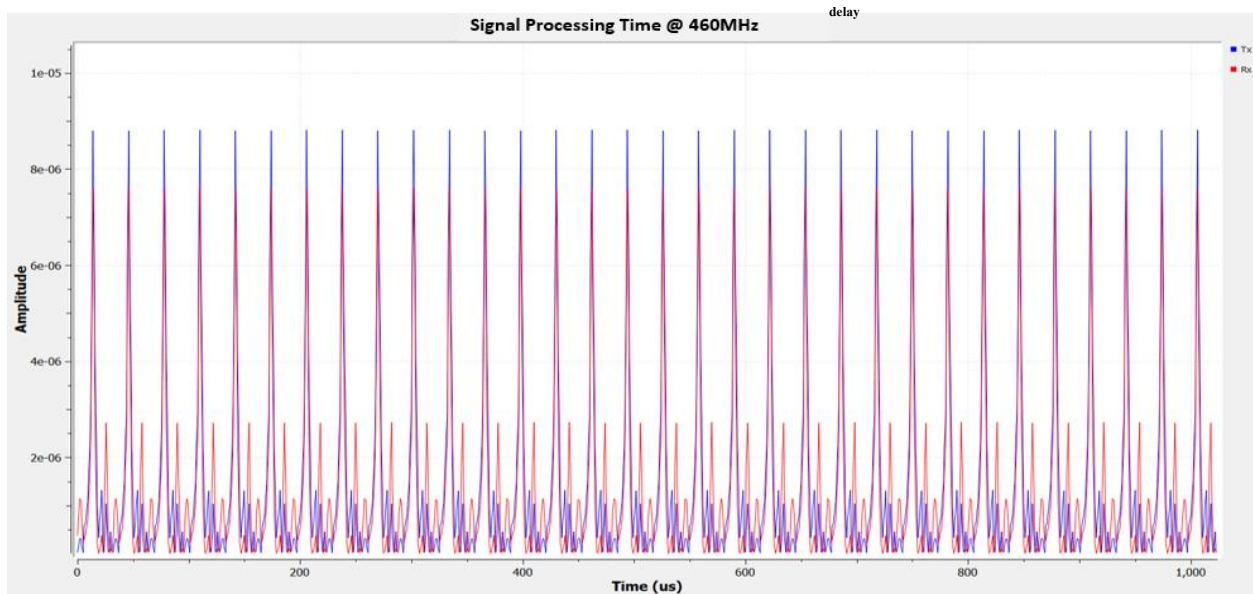
(b)

Figure 33. (a) Time domain oscillograph at 400.15 MHz (b) Time domain oscillograph at 460 MHz

In the same loopback test, signal processing delay was investigated by correlating the transmitted and received signals. A correlation estimation was implemented to correlate the data parameters. Data collected for a period of 1 s was captured and compared as indicated in Figure 34 (a) and (b).



(a)



(b)

Figure 34. (a) Correlated data graph at 400.15 MHz (b) Correlated data graph at 460 MHz

The test results showed that the transmitted data perfectly correlated with the received signals as expected.

### 4.3 Management of ISL Satellite Constellation

Currently the precise number of satellites to be launched is not yet decided. However, analysis of the likely challenges and potential solutions for constellation management in terms of satellites deployment, coordinating satellite movements, communication, and long-term maintenance has been done. The information below provides the challenges and potential solutions of implementing a constellation of small satellites with ISL network. The issues to deal with satellite deployment, communication and long-term maintenance are also given.

- **Challenge 1: Launching and deployment of a satellite constellation**

- Complexity in maintaining orbits and adequate spacing in satellites (collision avoidance) in the ISL

**Potential Solution**

- Precise launch and deployment techniques are essential to ensure correct initial configuration.
- Optimization of number of orbital planes to minimize the number of launches.
- Depending on the sizes of the satellites, implementing propulsion systems and

advanced deployment mechanisms may be useful for orbit maintenance and separation of satellites in a constellation.

- **Challenge 2: Communication Interference and Reliability**

- If performed verification and validation tests were insufficient, maintaining communication reliability and avoiding interference may be difficult.

**Potential Solution**

- Perform sufficient verification and validation communication test to check interference between the satellites in a constellation.
- Proper frequency planning, robust and advance modulation schemes and communication protocols must be implemented. In this paper, spread spectrum technique which allows frequency sharing has been proposed.
- Proper link budget analysis is critical to ensure there is sufficient system link margin.

- **Challenge 3: Long term maintenance**

- Ensuring an operation lifetime of the satellite's functionality and health.
- Minimizing the cost of replacing satellites.

**Potential Solution**

- Continuous monitoring of the satellite health by downlinking housekeeping data is of paramount important.
- Implementing remote diagnostic software which allows updating and upgrading of systems can be considered. In this paper we proposed the use of SDR as our transceiver for the mission because SDR is extensible, modular, upgradable and can be update over time remotely.
- The satellites design must be durable and robust to uncertainties including space environment
- Optimize the satellite lifetime in orbit and the cost associated to ensure the lifetime.

- **Challenge 4: Data Processing and Distribution**

- Large data collection, storing, processing, and distribution from a constellation of satellites

**Potential Solution**

- Onboard processing is required such that only water vapor data is transferred for



downlink to the ground station. This is what we are doing in this proposed system as explained in section 2 and 3 of this paper.

- Use of high-power processing microcontrollers also helps but consideration of power consumptions must be taken into account
- Use high data rate communication systems like S, C or X bands for data downlink.

- **Challenge 5: Synchronization**

- Achieving precise synchronization between satellites to ensure coordinated operations

- **Potential Solution**

- This paper has proposed the use of atomic clocks such as GPS or CSAC clock to account for any jittering, clock errors and unnecessary delays which affects the measurement result.
- Implement the Polyphase time synchronization and Costas loop which accounts for time synchronization and phase recover. These were implemented in this research as explained.

**Plans to manage the large constellation are also given below as follows:**

**1. Centralized Ground Control Stations:**

Centralized ground control stations shall manage and monitor the constellation, overseeing activities like orbit adjustments, health monitoring, and payload operations.

**2. Autonomous Operations:**

Advanced automation and autonomous systems would be essential for routine operations, such as collision avoidance maneuvers and satellite repositioning.

**3. Orbital Design and Distribution:**

Satellites within the constellation would be distributed across different orbital planes, altitudes, and inclinations to optimize coverage and avoid collisions.

Considering the future scalability of the proposed technique, strategies for maintaining accuracy and reliability of measurements as the number of satellites in the constellation increases were also evaluated. Maintaining accuracy and reliability as the constellation size augments is a crucial challenge in scalable satellite systems. Here are several strategies to ensure accuracy and reliability while scaling up the proposed technique:

1. To consider an incremental deployment approach, i.e., adding satellites in stages,

validate, fine-tune the system's performance, accuracy and reliability as the constellation grows.

2. To continuously test and simulate the behavior and performance of the constellation under various scenarios
3. To enhance the scalable software architecture design that can accommodate the increasing number of satellites without compromising performance.
4. To implement robust monitoring and diagnostics capabilities that identifies issues or deviations in real-time and enable swift corrective actions
5. To implement distributed and redundant systems so that no single point of failure can compromise the accuracy of the measurements. Also, critical functions shall be distributed across multiple satellites to increase fault tolerance and reliability.
6. To stay updated on regulatory requirements and spectrum allocations so that the increasing number of satellites can operate within legal frameworks.

Backup and redundancy measures are critical to ensuring the continuity of data collection and transmission in intersatellite communication networks, especially in the face of disruptions or interference. Given the potential for disruption or interference in communication networks, several backup or redundancy measures have been considered to ensure data collection and transmission remain uninterrupted and these includes:

1. Onboard data storage on SD cards and flash memories has been implemented in the system. If communication is disrupted, still data is stored in the flash memories and can be transmitted once link is established. Regular ground testing and simulation exercises of data collection (from the SD cards and flash memories) and transmission to assess the effectiveness of backup and redundancy measures under various disruption scenarios such as loss of sight were conducted.
2. Mesh network topology of inter satellites link where satellites can communicate directly with multiple neighboring satellites to collect water vapor and TEC data was implemented. This provides alternative communication measurements paths in case of a disruption in the primary link.
3. Phase, time and frequency offsets recovery has been implemented to ensure successful decoding of receiving signals

In the near future we intend to further implement the following measures to ensure data

collection and transmission remain uninterrupted:

1. Deploy redundant satellites within the constellation that can take over the responsibilities of a failed satellite. This ensures that data collection and transmission can continue even if one satellite experiences issues.
2. Implement dynamic routing algorithms that can reroute data through different paths in real-time, adapting to changing communication conditions.
3. Use multiple ground stations located in different geographic locations to communicate with the constellation, providing redundancy in ground-based communication.

Plan to integrate the acquired data into global atmospheric databases for climate and weather prediction models, through collaboration or coordination with existing research initiatives will be required. Participating and contributing to ongoing research initiatives, adherence to accepted standards and data sharing agreements, are necessary for integrating obtained data into global atmospheric databases for climate and weather prediction models. The 3D mapped data of TWVC shall be aligned with standardized formats, units and metadata acknowledged by the atmospheric research community. Additionally, partnership with organizations that specialize in collecting and distributing atmospheric data will be considered. To guarantee seamless integration of the acquired data with existing global atmospheric databases, data quality control shall be conducted by institutions that specializes with data evaluation and validation. Institutions, and researchers in-volved in atmospheric modelling and research shall be privileged with open access to the acquired data. Finally, the institute shall do workshops and forums that bring together researchers, modelers, and data providers to discuss integration challenges, strategies, and opportunities.

## CHAPTER 5

### WATER VAPOR MEASUREMENT CONCEPT, FREQUENCY MANIPULATION AND MISSION DETERMINATION BASED ON TIME DELAY EVALUATIONS

#### 5.1 Overview

In this chapter, the physical properties of TWVC and TEC that influences RF signals and the theoretical evaluations on how atmospheric water vapor can be deduced is explained in detail. Additionally, the procedures to determine the mission execution, time detection and selection of frequency bands are summarized. Furthermore, this section gives some comparison of the proposed frequency manipulation methods (modified XML-RPC and TCP/IP) with existing methods, discussing advantages, drawbacks, and potential scenarios where each approach is most suitable. and finally link budget analysis is given.

#### 5.2 Physical Properties of TWVC and TEC that Influences RF Signals [121,122]

Atmospheric water vapor and total electron density can affect radio waves due to their impact on the propagation of electromagnetic waves.

TWVC affects radio signal propagation through refraction, reflections, absorption, dispersion, scattering, and phase shifts. The specific physical properties of water vapor that affect radio signal propagation include:

- Vapor density: The concentration of water vapor in the atmosphere is a crucial factor. Areas with higher vapor density will exhibit more significant effects on radio wave propagation.
- Specific humidity: Specific humidity refers to the mass of water vapor in a unit volume of air. Higher specific humidity means more water vapor is available to interact with radio waves.
- Frequency: The impact of water vapor on radio waves varies with frequency. Higher frequencies are more affected than lower frequencies due to their interaction with water molecules.

The graphs in Figure 35 [121], illustrate variation of TWVC with temperature and vapor density. Water vapor in the atmosphere can cause refraction of radio waves. Refraction occurs when the speed of a radio wave changes as it passes from one medium (e.g., air) to another (e.g., air with a

different water vapor content).

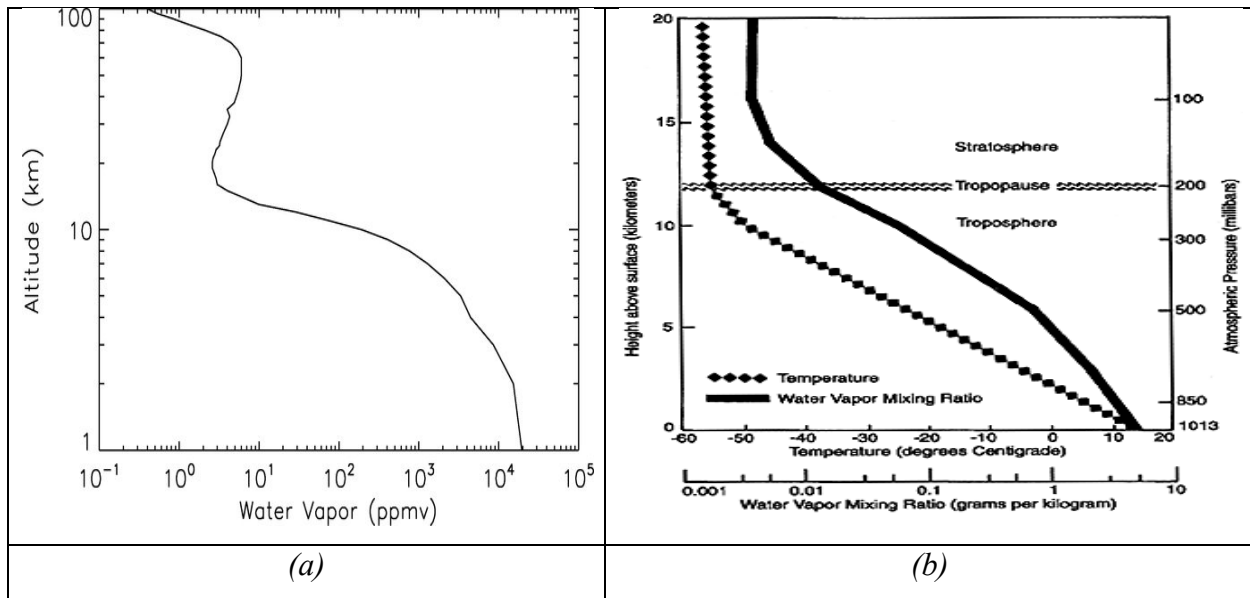


Figure 35 (a) Altitude vs vapor density (b) TWVC variation of altitude vs temperature [121]

This change in speed causes the radio wave to change its direction. The amount of refraction depends on the temperature, pressure, and water vapor concentration at different altitudes in the atmosphere. TWVC signal reflections are considered negligible since water molecules are not efficient reflector of electromagnetic waves. Also, water vapor can absorb specific frequencies of electromagnetic radiation, particularly in the microwave and millimeter-wave bands. This absorption weakens radio signals at those frequencies. Water vapor molecules can absorb energy from radio waves, leading to signal attenuation. The absorption characteristics depend on the frequency of the radio wave and the specific rotational and vibrational energy levels of water molecules. Moreover, water vapor can cause dispersion of radio waves, leading to different frequencies within a signal arriving at the receiver at different times. This can lead to signal distortion and make it challenging to decode or demodulate the received signal. The dispersion properties of water vapor are determined by its refractive index, which varies with frequency. Water vapor can also scatter radio waves, especially at higher frequencies. Scattering is a phenomenon where small water vapor droplets in clouds can deflect radio waves in various directions, reducing the strength of the received signal. Water vapor can introduce phase shifts in radio waves as they pass through different layers of the atmosphere with varying water vapor content. This phase shift can affect the coherence and quality of the received signal. Using UHF frequencies for ISL communication, only refraction is dominant as absorption, scattering, phase

shift and dispersion can only significantly affect high frequency waves of the orders of microwave and millimeter-wave bands.

Total Electron Content (TEC) is a critical parameter in radio signal propagation, particularly in the context of ionospheric effects. TEC is a measure of the total number of free electrons in a column of the Earth's ionosphere, and it plays a significant role in the propagation of radio signals, especially in the HF (High Frequency), VHF (Very High Frequency), and UHF (Ultra High Frequency) bands. The most fundamental property of TEC is the electron density, which represents the number of free electrons in a given volume of the ionosphere. The ionosphere consists of different layers, such as the D, E, and F layers, each with varying electron densities. These layers can influence how radio waves interact with the ionosphere. The ion composition in the ionosphere affects TEC. The ionosphere contains various ions, including oxygen ions ( $O^+$ ), nitrogen ions ( $N^+$ ), and molecular ions ( $O_2^+$  and  $N_2^+$ ), in addition to free electrons. The presence and abundance of these ions can influence the interactions between radio waves and the ionosphere. Figure 36 shows the variation of electron density with altitude and the resultant delayed wave in the troposphere and ionosphere.

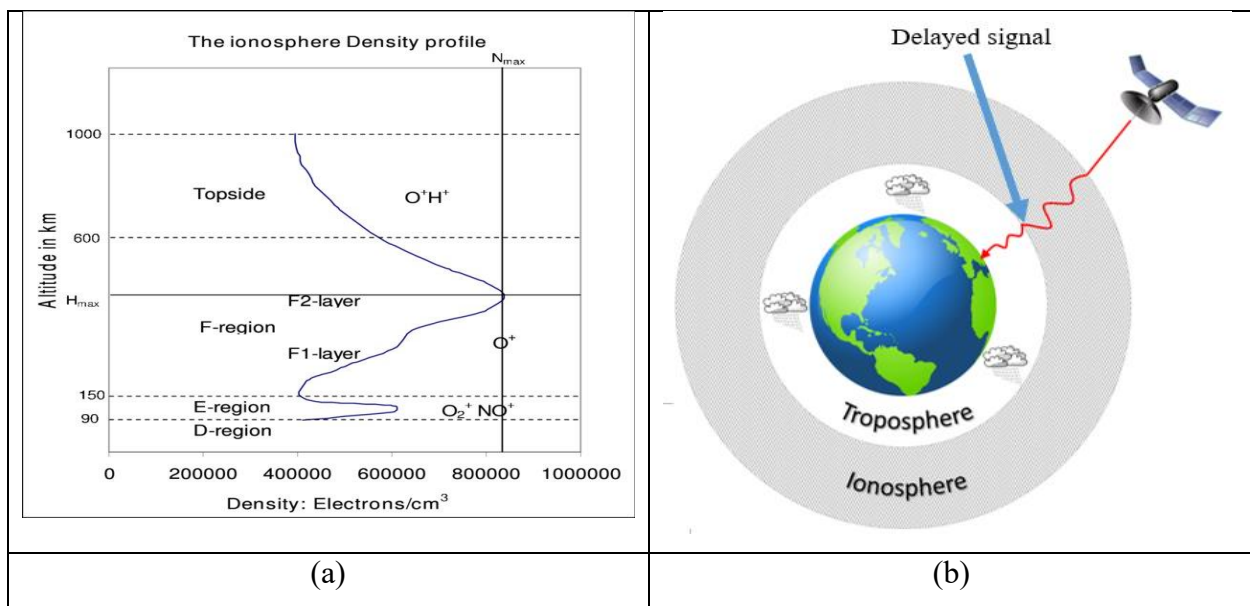


Figure 36. (a) TEC variations of altitude vs electron density. (b) Delayed wave in tropo-ionosphere region [122]

TEC exhibits both seasonal and diurnal variations. Seasonal changes are influenced by factors like solar activity and the Earth's tilt. Diurnal variations are associated with the day-night cycle. These variations can affect the behavior of the ionosphere and, consequently, radio wave

propagation. Solar activity, such as solar flares, sunspots, and the solar cycle, can significantly impact TEC. High solar activity can increase electron densities in the ionosphere, enhancing radio signal propagation in the HF and VHF bands, while low solar activity can reduce TEC, leading to less favorable propagation conditions. Geomagnetic storms, triggered by solar activity, can disturb the Earth's magnetic field and affect the behavior of the ionosphere, including TEC. During magnetic storms, TEC can experience fluctuations, leading to signal degradation. Anomalies in the ionosphere, such as ionospheric irregularities and plasma instabilities, can lead to spatial and temporal variations in TEC. These anomalies can create regions of enhanced or reduced electron density, impacting radio wave propagation. And finally, the Earth's magnetic field interacts with the charged particles in the ionosphere. The strength and orientation of the magnetic field can influence the motion and behavior of electrons in the ionosphere, affecting TEC. Under normal ionospheric conditions, 40 MHz is the highest-frequency radio wave that can be reflected from the ionosphere, therefore signal reflections are considered negligible compared to refractions.

### 5.3 Theoretical Deduction of Atmospheric Water Vapor

Figure 37 shows how the atmospheric water vapor and total electron content can be deduced considering the communication of two satellites Sat A and Sat B in the ISL network. In orbit, the satellites are in motion, so their positions and time change every second. Each satellite carries a GPS module which calculates position and time data. The position of a satellite relative to another satellite is known as the pseudo-range ( $L_p$ ). Signal propagation in space is primarily influenced by TWVC and TEC. Atmospheric water vapor content and total electron densities are dominant in the troposphere and the ionosphere, respectively. Signal deviation  $\alpha^\circ = 40.3 \left(\frac{m^3}{s^2}\right) \times 10^{16}(/m^3)/f^2$  due to multipath fading, and other atmospheric factors has been computed to be less than  $3^\circ$ , when considering 400.15 MHz and 460 MHz UHF ISL bands. Therefore, to detect the atmospheric water vapor, sounding is conducted near Earth using satellite constellation. Both Sat A and Sat B have the capability to transmit and receive ranging signals.

Knowing the satellites' location in the Earth-fixed coordinate system (ECEF) x, y, and z and the signal propagation time delay  $\delta T$  (s), TWVC and TEC can be estimated. Assuming Sat A is in transmission mode (Tx) while Sat B is in reception mode (Rx), the combined signal propagation delay due to the troposphere's and ionosphere's influence at each position along the

ISL path is obtained by comparing the transmitted and received signals. If the bit starting times or time stamp positions of the Tx and Rx signals can be detected, then the time delay can be calculated as described in Figure 38.

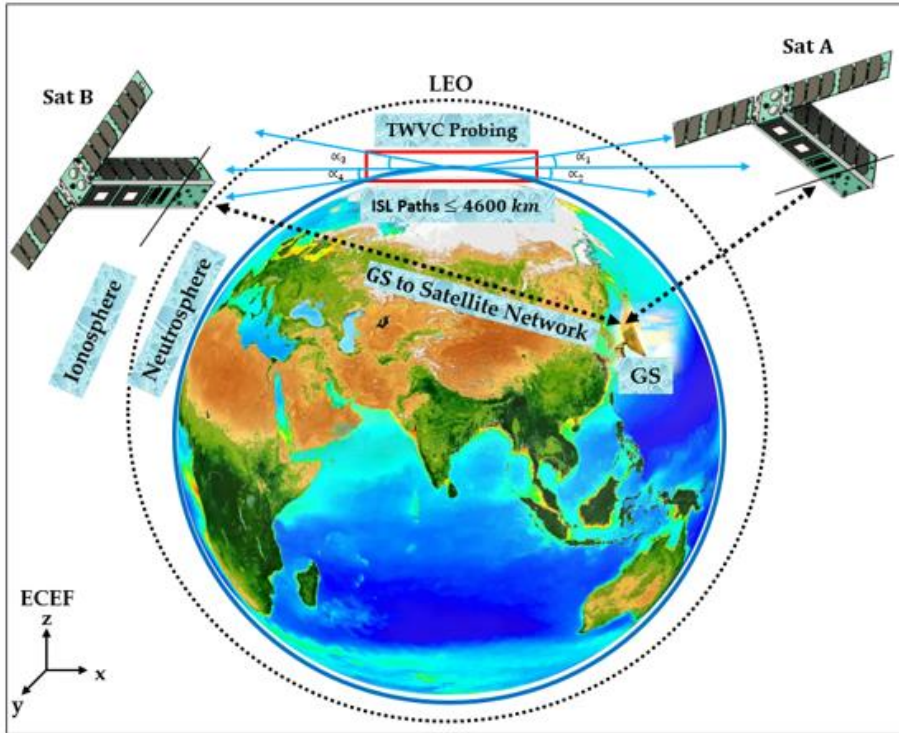


Figure 37. TWVC probing with the ISL network.

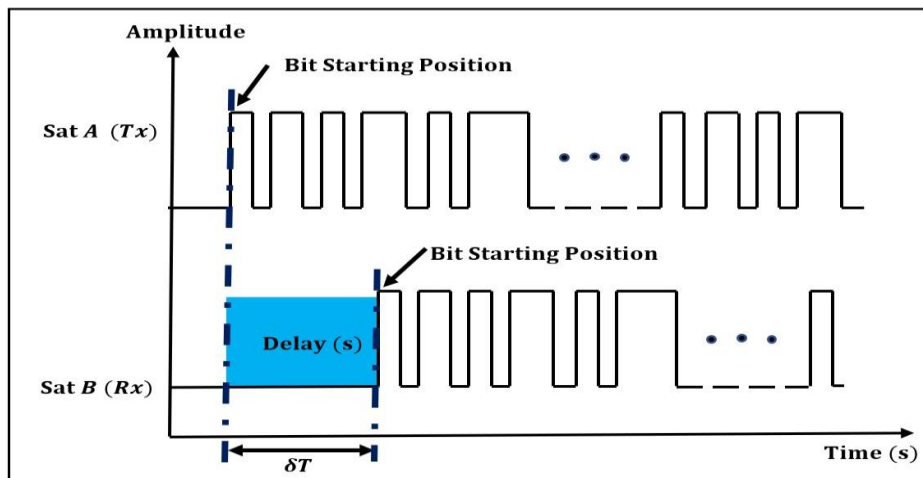


Figure 38. Time delay deductions

In a more holistic approach, when the frequency of communication is  $f_1$  (MHz), the time delay ( $\delta T_1$ ) of the signal propagation is obtained based on all channel effects. These include the influence of integrated electron density and integrated total WV density along the signal path from



Sat A and Sat B and vice versa at their positions in orbit denoted by A and B in the integrals, respectively. Mathematically,  $\delta T_1$  is deduced as follows:

$$\delta T_1 = \frac{L_{\rho_1}}{c} + \frac{a}{f_1^2} \int_A^B \eta_{e_1}(l) dl + \frac{1}{\Pi} \int_A^B \eta_{TWVC_1}(l) dl + \Delta t_{Rx} - \Delta t_{Tx} + \epsilon_{0_1} \quad 11$$

where  $L_{\rho_1}$  is the true range (m),  $c = 3.0 \times 10^8 \text{ ms}^{-1}$  is the speed of light,  $\Delta t_{Rx}$  (s) is the Sat B clock receiver offset,  $\Delta t_{Tx}$  (s) is the Sat A transmitter clock offset, and  $\epsilon_{0_1}$  (s) is the error in the range due to various other sources such as satellite instrument delays and relativistic clock corrections. The term  $dl$  represents the path integral differential,  $a = 40.3/c \approx 1.34 \times 10^{-7} \text{ m}^2/\text{s}$  is a constant for TEC determination [123], and  $\Pi$  [67,124,125] is an experimentally determined constant depending on air temperature. The term  $\eta_{TWVC_1}$  ( $\text{kg}/\text{m}^3$ ) is the water vapor density and its integral represents integrated total water vapor content along the ray path [67]. The total water vapor delay (s) primarily due to the tropospheric influence is deduced along the signal path based on integrated TWVC and  $\Pi$ . The term  $\eta_{e_1}$  ( $\text{electrons}/\text{m}^3$ ) is the total ionospheric electron density and its integral is TEC. The clock offsets are eliminated by using a precise clock as the clock source for both the transmitting and the receiving SDRs. The relativistic corrections and other known instrumented delays are compensated in the time delay detection software. The influence of multipath fading was neglected due to the smaller angle of deviation of less than  $3^\circ$ . Therefore, Equation (11) transforms to:

$$\delta T_1 = \frac{L_{\rho_1}}{c} + \frac{a}{f_1^2} \int_A^B \eta_{e_1}(l) dl + \frac{1}{\Pi} \int_A^B \eta_{TWVC_1}(l) dl \quad 12$$

The true range ( $L_\rho$ ) of each satellite relative to another satellite in the ISL network is computed from the altitude (m), latitude ( $^\circ$ ), and longitude ( $^\circ$ ) geodetic coordinates provided through the GPS module. When frequency is reconfigured to  $f_2$  (MHz), time delay  $\delta T_2$  is calculated as illustrated in Equation (13), where the satellite positions change from A to A' and from B to B', respectively.

$$\delta T_2 = \frac{L_{\rho_2}}{c} + \frac{a}{f_2^2} \int_{A'}^{B'} \eta_{e_2}(l) dl + \frac{1}{\Pi} \int_{A'}^{B'} \eta_{TWVC_2}(l) dl \quad 13$$

It is important to note that frequency translation is not achieved instantly when the satellites are in motion. As a result, the water vapor content and electron density are determined based on signal propagation time delay between two positions (A to A') and (B to B') of each satellite in the ISL network using two different frequencies. Thus, to derive TWVC and TEC, the two-time delays ( $\delta T_1$  and  $\delta T_2$ ) are compared as illustrated in Equation (14):

$$\delta T_1 - \delta T_2 = \frac{1}{c}(L_{\rho_1} - L_{\rho_2}) + a \left( \frac{1}{f_1^B} \int_A^B \eta_{e_1}(l) dl - \frac{1}{f_2^{B'}} \int_{A'}^{B'} \eta_{e_2}(l) dl \right) + \frac{1}{H} \left( \int_A^B \eta_{TWVC_1}(l) dl - \int_{A'}^{B'} \eta_{TWVC_2}(l) dl \right) \quad 14$$

In the closest range, when considering a constellation of thousands of satellites in different LEO orbital planes and directions, the difference between  $L_{\rho_1}$  and  $L_{\rho_2}$  is assumed to be at least 15 km. Assuming that the TWVC and TEC at the two positions of each satellite are the same, with TEC varying inversely to the square of the frequencies, this implies:

$$\int_A^B \eta_{TWVC_1}(l) dl \approx \int_{A'}^{B'} \eta_{TWVC_2}(l) dl = \int \eta_{TWVC}(l) dl, \text{ and} \quad 15$$

$$\int_A^B \eta_{e_1}(l) dl \approx \int_{A'}^{B'} \eta_{e_2}(l) dl = \int \eta_e(l) dl \quad 16$$

Substituting (5) and (6) into (4), TEC can be deduced as follows:

$$a \left( \frac{1}{f_1^2} - \frac{1}{f_2^2} \right) \int \eta_e(l) dl = (\delta T_1 - \delta T_2) - \frac{1}{c}(L_{\rho_1} - L_{\rho_2}) \quad 17$$

$$\text{TEC} = \int \eta_e(l) dl = \frac{(\delta T_1 - \delta T_2) - \frac{1}{c}(L_{\rho_1} - L_{\rho_2})}{a \left( \frac{1}{f_1^2} - \frac{1}{f_2^2} \right)} \quad 18$$

However, the assumptions in (15) and (16) introduce an error in the measurement accuracy. This error is assumed to become negligible when the frequency transition can be achieved in 1 s or less. Also, by averaging measurements from multiple frequencies, the introduced error is anticipated to be very negligible. This is the other reason why multiple frequencies and frequency reconfiguration has been considered as a way of improving the mission measurement accuracy aside from distinguishing TWVC from TEC. When TEC variations become known, total water vapor content, TWVC, is computed from Equation (12) as follows:

$$\text{TWVC} = \int \eta_{TWVC}(l) dl = \Pi \left( \delta T_1 - \frac{L_{\rho_1}}{c} - \frac{a}{f_1^2} \int \eta_{e_1}(l) dl \right) \quad 19$$

The key steps in this method are described as follows:

- Measuring the signal time delay by utilizing two frequencies between the satellites.
- Distinguishing the signal time delay due to TEC and TWVC by comparing the two frequency measurements.
- Collecting all the measurement data of TEC and TWVC within a time period
- In the case of satellites in multiples orbital planes, obtain a 3D distribution of TEC and TWVC.
- Determining the most probable set of distribution that agrees with the measurement data

of TEC and TWVC.

- Deducing only TWVC contribution by removing TEC values.

In line with Kyushu Institute of Technology satellite development projects, a constellation of more than 1000 satellites in low Earth orbit are expected to be launched for scientific studies of the atmosphere including for this mission to determine TWVC. These studies will be a continuation of the SPATIUM-I and SPATIUM-II missions which were demonstrated in orbit. The ISL communication network shall achieve a separation distance of 15 km to 4600 km and a temporal resolution of 5 to 15 min.

### 5.3.1 Procedure to Determine the ISL Frequency Bands

The frequency bands for the water vapor mission are limited to the available meteorological UHF communication frequencies in the international telecommunication union (ITU) region 3 where Kyutech in Japan is located [126,127]. To probe atmospheric water vapor in near-Earth regions using the ISL network, two available options (available band pairs) of frequencies are listed as shown in Table 10. From the available options, only one frequency from each of the two pairs can be selected. Considering the mission requirements, lower frequency bands give better estimations of TWVC and TEC.

*Table 10. Frequency selection table*

Bands	Band 1 ( $f_1$ MHz)	Band 2 ( $f_2$ MHz)	Maximum Frequency Gap
Available band pairs	400.15-401	460-470	69.85
Selected bands	400.15	460	59.85

The reason being that lower bands are influenced much more than higher bands. As a result, two low frequency bands  $f_1 = 400.15$  MHz and  $f_2 = 460.00$  MHz have been selected from each of the two available pairs. These two frequencies are known and automatically detected by each satellite in the ISL network. Furthermore, the two frequencies have a relatively smaller frequency gap making it feasible to implement with a single antenna that could be tuned to operate at both frequencies while either transmitting or receiving SS signals. Implementation of one antenna to perform both the transmission and reception of the SS signal is proposed to reduce complexity of the design configuration as well as to save on the occupied volume and mass of the satellite. Also, this frequency gap is wide enough to determine and differentiate variation of the TEC from the TWVC data.

### 5.3.2 Procedure to Determine the Time Delay

To detect the time delay, the satellites in the ISL network require SS signals and 1PPS time stamp references for both the outgoing (Tx) and incoming (Rx) signals. On the receiving side, data transmitted at both frequencies ( $f_1$  and  $f_2$ ) is saved as text or recorded wave files. The files are analyzed onboard the satellite to detect the delay following the procedure indicated in Figure 39 below.

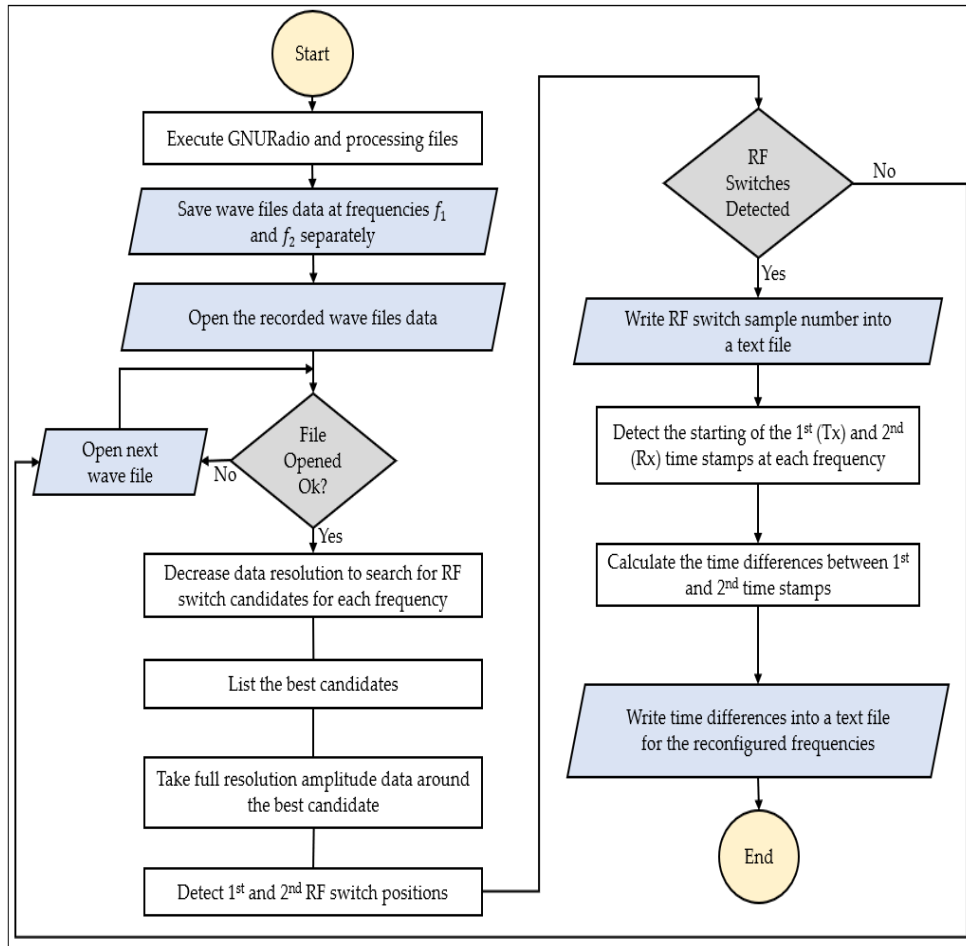


Figure 39. Mission execution scenario

## 5.4 Frequency Reconfiguration in the ISL Network

### 5.4.1 Feasibility of Frequency Manipulation

The communication parameters like frequency, sample rate, bandwidth as well as internal SDR transmitter and receiver gains are controlled using the GNU Radio software (v3.8.2.0). To manipulate these parameters during runtime, there is a need to access the inphase and quadrature

(IQ) data stream inside GNU Radio Python and/or C++ blocks. Various frequency reconfiguration techniques are used in satellite communications to optimize performance, increase measurement accuracy, and ensure reliable communication under different conditions. Frequency reconfiguration algorithms used in satellite communications include dynamic spectrum access (DSA) [128], cognitive radio-based frequency reconfiguration [129], frequency-hopping spread spectrum (FHSS) [130], adaptive beamforming and frequency steering [131], and adaptive modulation and coding (AMC) [132]. DSA algorithms allow satellites to adjust their frequency utilization dynamically depending on the availability of spectra in their operational environment. They are nevertheless quite sophisticated in terms of real-time spectrum detection, frequency reconfiguration procedures, and decision making. This complexity augments the likelihood of algorithmic errors. Utilizing cognitive radio approaches, it is possible to identify underutilized or unused frequency bands and opportunistically switch to them. Nonetheless, their spectrum detection, decision making, and reconfiguration impose delays, rendering them unsuitable for real-time applications or crucial communication scenarios.

Moreover, FHSS frequency reconfiguration algorithms provide benefits in terms of security, interference avoidance, and fading resilience, they also present issues in terms of complexity, synchronization, latency, and possible constraints in data rates and bandwidth efficiency. The advantages of adaptive beamforming and frequency-steering frequency reconfiguration algorithms include improved signal quality, reduced interference, and dynamic adaptation; however, maintaining the accurate calibration and alignment of antenna rays are essential for efficient beamforming and steering. Any misalignment significantly degrades performance. AMC frequency reconfiguration methods enhance communication efficiency by dynamically altering the modulation scheme and error-correction coding dependent on the effectiveness of the communication channel. On the other hand, certain AMC algorithms rely on feedback from the receiver to precisely determine the optimal modulation and coding parameters, and this potentially adds communication overhead.

In order to improve performance and reconfiguration speed in real time, ensure reliability, reduce complexity, ensure interoperability in systems and programming languages, and to lower network overhead two algorithms based on server and client architecture were proposed and implemented. These techniques are robust and they achieve the software-based manipulation of SDR and communication parameters in a remote setup of satellites in the ISL network. The first

technique is a modified extensible markup language-remote procedure call (modified XMLRPC) and the second one is the TCP/IP method as shown in Figure 40. In previous versions of the GNU Radio software from 3.7 and below, the XMLRPC algorithm has been implemented to support this function in a server and client setup [48,133]. However, the latest version of GNU Radio from 3.8 and above are incompatible with the traditional XMLRPC client blocks.

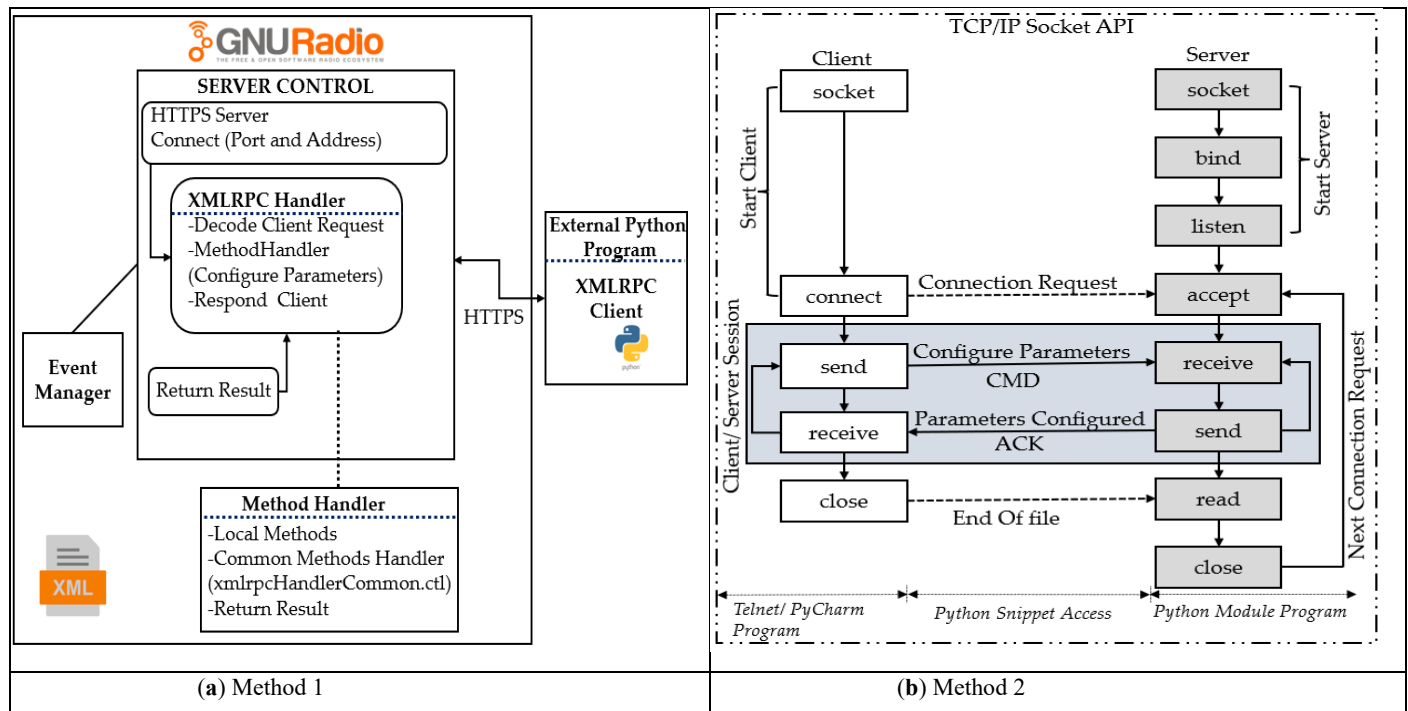


Figure 40. Frequency manipulation flow diagrams: (a) XML-RPC algorithm architecture; (b) TCP/IP algorithm architecture.

This study demonstrated an innovation of two techniques that were implemented to grant access to interact with the IQ data stream of GNU Radio Python and C++ modules upon starting, in the middle or at the end of mission execution. SDR frequency manipulation is facilitated by the dynamic and static nature of GNURadio parameters. Figure 41 below shows an example of a UHD: USRP Source block in which dynamic and static parameters are highlighted. Dynamic parameters, such as the center frequency, automatic gain control, sample rate, antenna type, and bandwidth, are indicated with an underline, whereas static parameters, such as the clock source, number of channels, et cetera, are not. Static parameters are fixed and cannot be remotely accessed, whereas dynamic parameters are accessible, changeable, and can be altered during runtime. The dynamic parameters are implemented with call-back or set functions that are called whenever a variable is updated. In GNURadio, USRP 205 mini-i is commanded through UHD: USRP sink and source

blocks on the transmission and receiving terminals. In this study, frequency parameters were remotely tuned; hence, they were made dynamic.

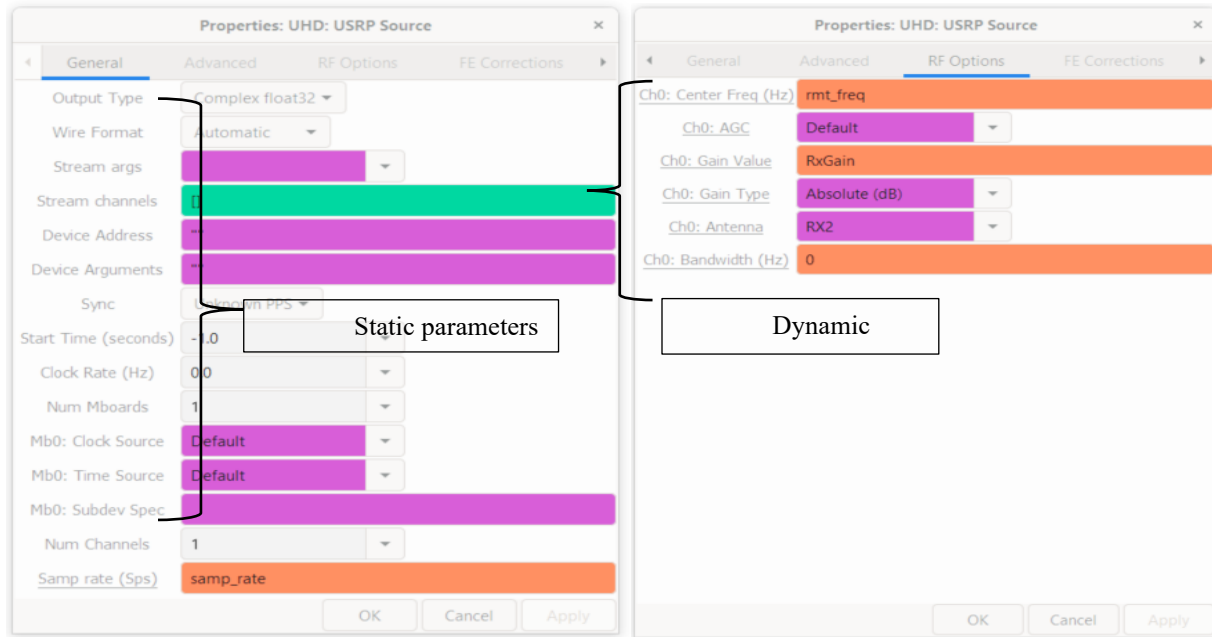


Figure 41. Static and dynamic parameters

#### 5.4.2 Procedure of Modified XML-RPC Algorithm

The algorithm makes procedure calls through the hypertext transfer protocol secure (HTTPS) in a server-client relationship as given in Figure 40 (a). Unlike the traditional client blocks which were typically implemented inside GNU Radio blocks, we modified the concept and implemented an external Python-based client program which is compatible with the latest versions of GNU Radio. The XML-RPC client sends the set messages to the respective XML-RPC server through a reconfiguration command. Acceptance of connection by the server program enables the client's commands to alter SDR parameters inside the GNU Radio. The server facilitates access to an external client-requesting program. This is done through variable call-back functions in the flow graph and procedures that enable tuning of the SDR parameters. The server architecture contains handlers in which the tuning functions and variables are stored. The event manager in the server controls the operation of events or functions requested by the client program. The returned value of the functions is then sent to the client via a secure HTTPS protocol with XML encoding. The encrypted HTTPS uses secure sockets and transport layer security for data integrity and protection.

### 5.4.3 Procedure of the TCP/IP Algorithm

The proposed TCP/IP reconfiguration method also operates in a client-server setup to manipulate SDR parameters. The server program uses a Python module block, and the client program is implemented with an external Python integrated development environment (IDE) such as PyCharm or a Telnet client program [118]. For this program, a Python snippets module was implemented to give the client access to the server program and enable tuning of the SDR GNU Radio parameters. The snippet is executed as a thread that passes self-arguments to access variables from the main GNU Radio flowgraph [118]. Similar to the XMLRPC method, the reconfiguration with TCP/IP method is also feasible at the beginning, during, and at the end of mission execution. The flow graph in Figure 40 (b) describes the TCP/IP architecture and operation procedure.

### 5.4.4 Frequency Manipulation Results and Analysis

Figure 42 demonstrates the frequency translation from the 400.15 MHz to 460.00 MHz peaks and vice versa between Sat A and Sat B.

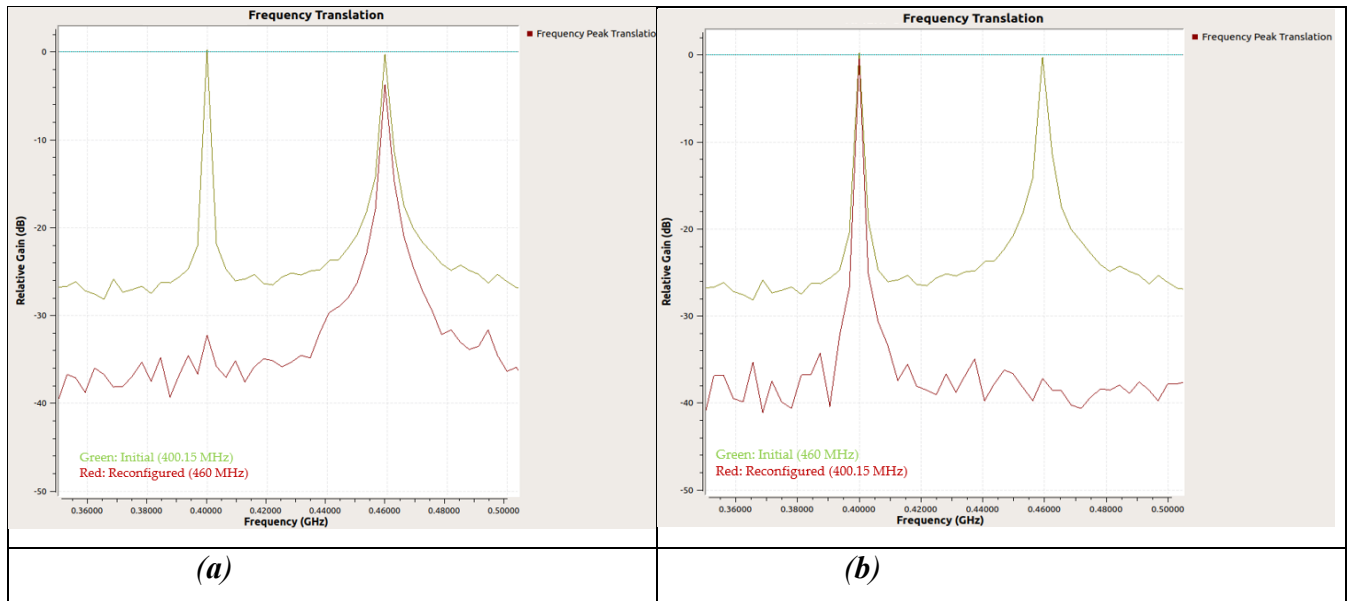


Figure 42. Demonstration of frequency manipulation: (a) 460.00 MHz to 400.15 MHz; (b) 400.15 MHz to 460.00 MHz.

SS peaks were selected and filter in-order to visualize shifting of frequency peaks. The SDR gains were tuned to attain the transceivers' maximum output power. Initially, the frequency of communication between satellite A and B was set at 400.15 MHz. A new frequency of 460.00 MHz was set at Sat A and SS signals were transmitted to Sat B. Sat B automatically detected the new





confirmed that client software could connect with the server programs, and parameters inside the GNURadio could be accessed and tuned as shown in Figure 44.

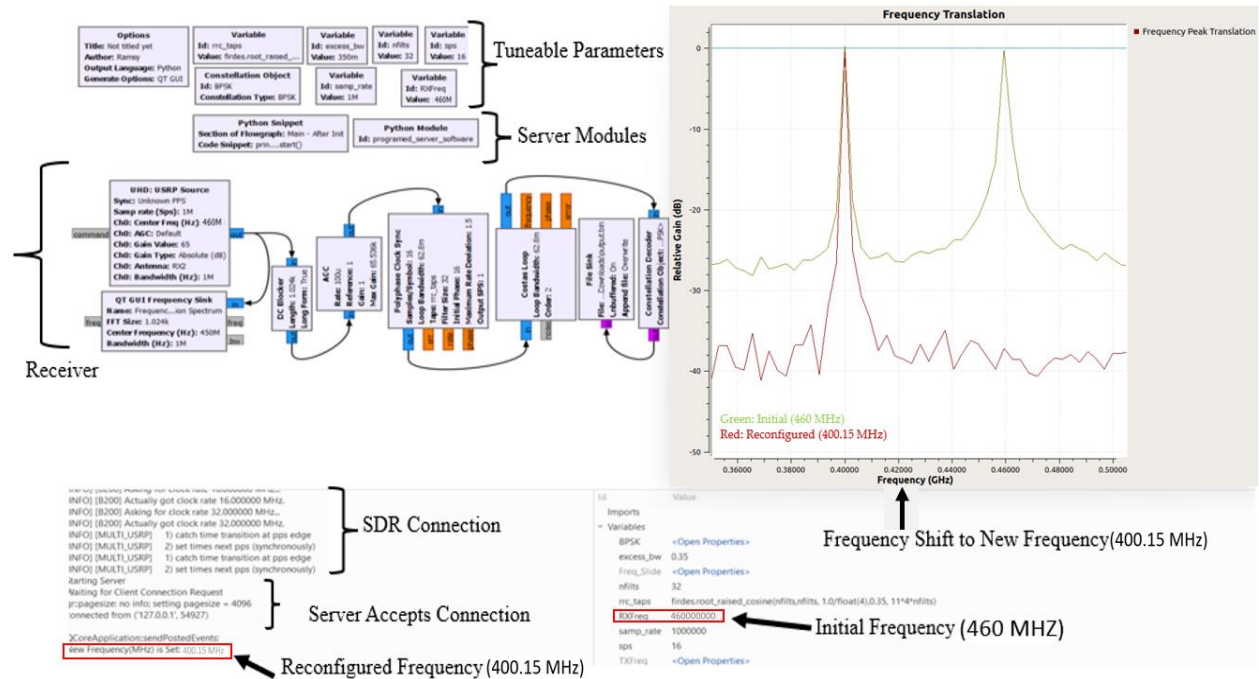


Figure 44. Server-Client connection confirmation inside the GNURadio

Table 11 highlights the comparison between the two methods of frequency reconfiguration.

Table 11. Comparison of XML-RPC and TCP/IP algorithms

Property	XML-RPC Algorithm	TCP/IP Algorithm
Efficiency/speed	Translate frequencies in 1s	Translate frequencies in 1s
Client	Eternal Python program, GNURadio implemented client	External Python program, Telnet Client, GNURadio Python snippets and Python modules
Server	GNURadio implemented server	GNURadio implemented server
Security	Secured with HTTPS and transport layer security	Secured with symmetric and public encryption
Programmable flexibility	flexible	More flexible
Connectivity	HTTPS, IP address and ports	Sockets, IP address, and ports
Reliability	Very reliable	Very reliable

## 5.5 Determination of Location Data

Tests were conducted to verify the location, time and 1PPS data from the GPS modules. The location data is given by the latitude, longitude, and altitude outputs where the time data is given as time in “hr.: mm: ss” following UTC time configuration. The time and location data are collected in \$GPGGA format from the GPS module by the RPi via UART data lines. The GPS this GPS is transmitted as part of SS signals between satellites in the ISL networks. 1PPS signal output was also confirmed. The 1PPS signal are superimposed as time stamps on the incoming and outgoing signals using the RF switches. Figure 45 shows tabular representation of GPS data, and Figure 46 is the comparison of the Foxtrot GPS map and google maps data to confirm the location accuracy.

```
tcp://localhost:2947          NMEA0183>
```

<b>Time:</b> 2023-03-18T04:32:00.000Z		<b>Lat:</b> 33 53' 30.08363" Non: 130 50' 25.01051" E	
<b>Cooked TPV</b>			
GPGSV GPGLL GPRMC GPVTG GPGGA GPGSA			
<b>Sentences</b>			

Ch	PRN	Az	El	S/N
0	1	192	22	0
1	4	216	8	0
2	7	302	46	17
3	8	334	70	19
4	9	248	12	16
5	10	81	8	26
6	16	84	41	34
7	21	181	49	20
8	23	51	2	19
9	26	108	13	25
10	27	38	48	32
11	30	318	13	0

<b>Time:</b> 043200.00	<b>Time:</b> 043200.00
<b>Latitude:</b> 3353.51394 N	<b>Latitude:</b> 3353.51394
<b>Longitude:</b> 13050.41842 E	<b>Longitude:</b> 13050.41842
<b>Speed:</b> 0.213	<b>Altitude:</b> 50.5
<b>Course:</b>	<b>Quality:</b> 1 Sats: 07
<b>Status:</b> A FAA: A	<b>HDOP:</b> 1.36
<b>MagVar:</b>	<b>Geoid:</b> 28.4
<b>RMC</b>	<b>GGA</b>

<b>Mode:</b> A3 Sats: 7 8 10 16 21	<b>UTC:</b>	<b>RMS:</b>
<b>DOP:</b> H=1.36 V=1.64 P=2.13	<b>MAJ:</b>	<b>MIN:</b>
<b>TOFF:</b> 0.145990228	<b>ORI:</b>	<b>LAT:</b>
<b>PPS:</b> -0.001525091	<b>LON:</b>	<b>ALT:</b>
<b>GSA + PPS</b>	<b>GST</b>	

Figure 45. Results of time and location data

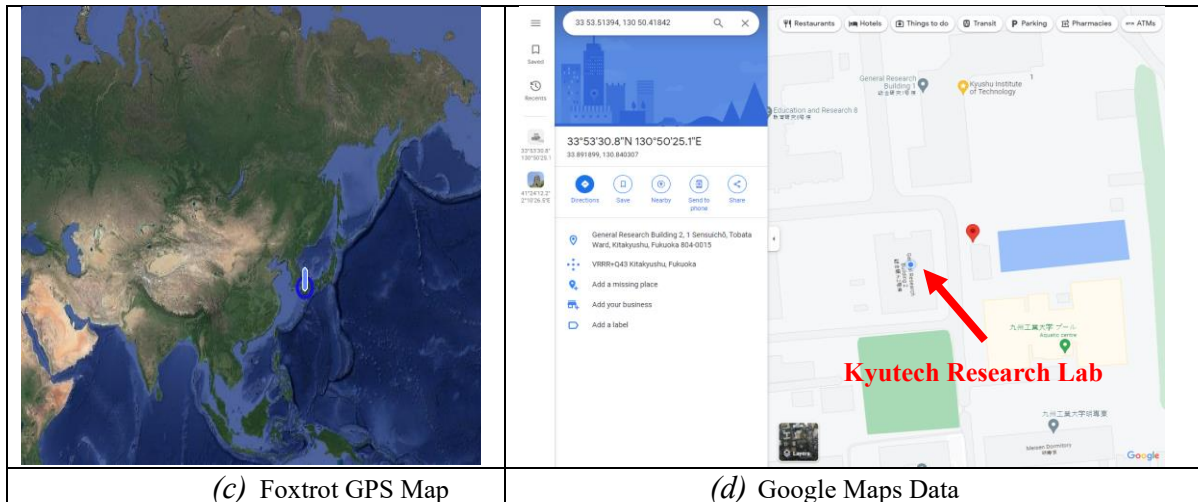


Figure 46. GPS location confirmed by google maps

## 5.6 Time Stamping with 1PPS GPS Signal

The 1PPS GPS reference time stamps from the GPS modules mounted on each satellite were locked to more than 10 satellites and synchronized as shown in Figure 47. On a duty cycle of 1 s, each pulse was detected to be 0.9 s ON and 0.1 s OFF.

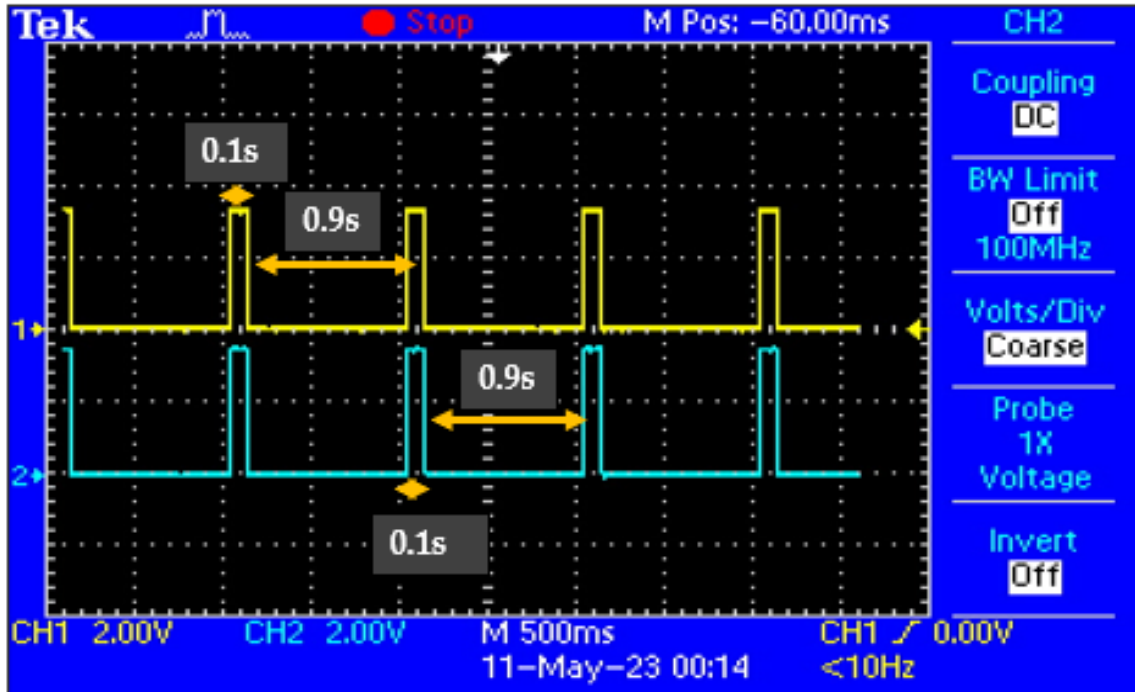


Figure 47. Synchronized 1PPS GPS signal for Tx (yellow) and for Rx (blue).

These 1PPS reference time stamps were marked on both the incoming and the outgoing signals. The saved wave file data shown in Figure 48 was analyzed to visualize and to detect the time stamp and possible signal delay.

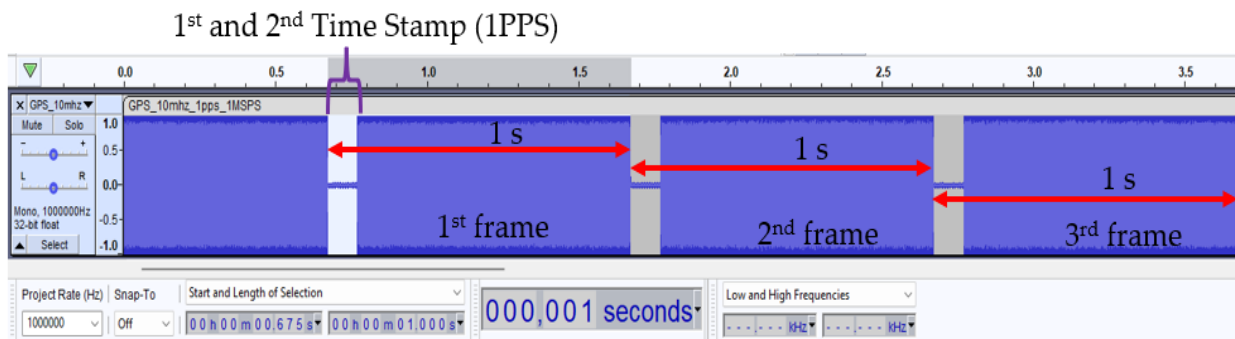


Figure 48. Sample of data at 1 MSPS at 460.00 MHz.

The horizontal and vertical axis represent the time and amplitude of the signal, respectively. Three data frames recorded for 3.675 s were observed with a duty cycle of 1 s (0.9 s ON and 0.1 s

OFF). Since both satellite payloads were stationary and there was no influence of TWVC and TEC, the time stamps of the transmitted and the received signal were superimposed at the same positions. This result signifies that the time stamp function was successful and no delay was detected at both 400.15 MHz and 460.00 MHz frequencies since the signals were free from TWVC and TEC delays.

During the table satellite test, the SDR hardware suffered from a 35  $\mu$ s clock jitter error because its internal clock was not fast enough to support the transfer of data. The clock jittering distorted the signals by flipping the bits, inducing noise data or causing time offset by shifting the positions of the bits. To solve the problem, a 10 MHz GPS clock was integrated to the system to eliminate the effects of clock jittering. After the transmission of SS signal from one satellite (Sat A), three data frames received on the second satellite (Sat B) were analyzed. Figure 49 shows parts of the received data frames when the RF switch was turned ON and OFF.

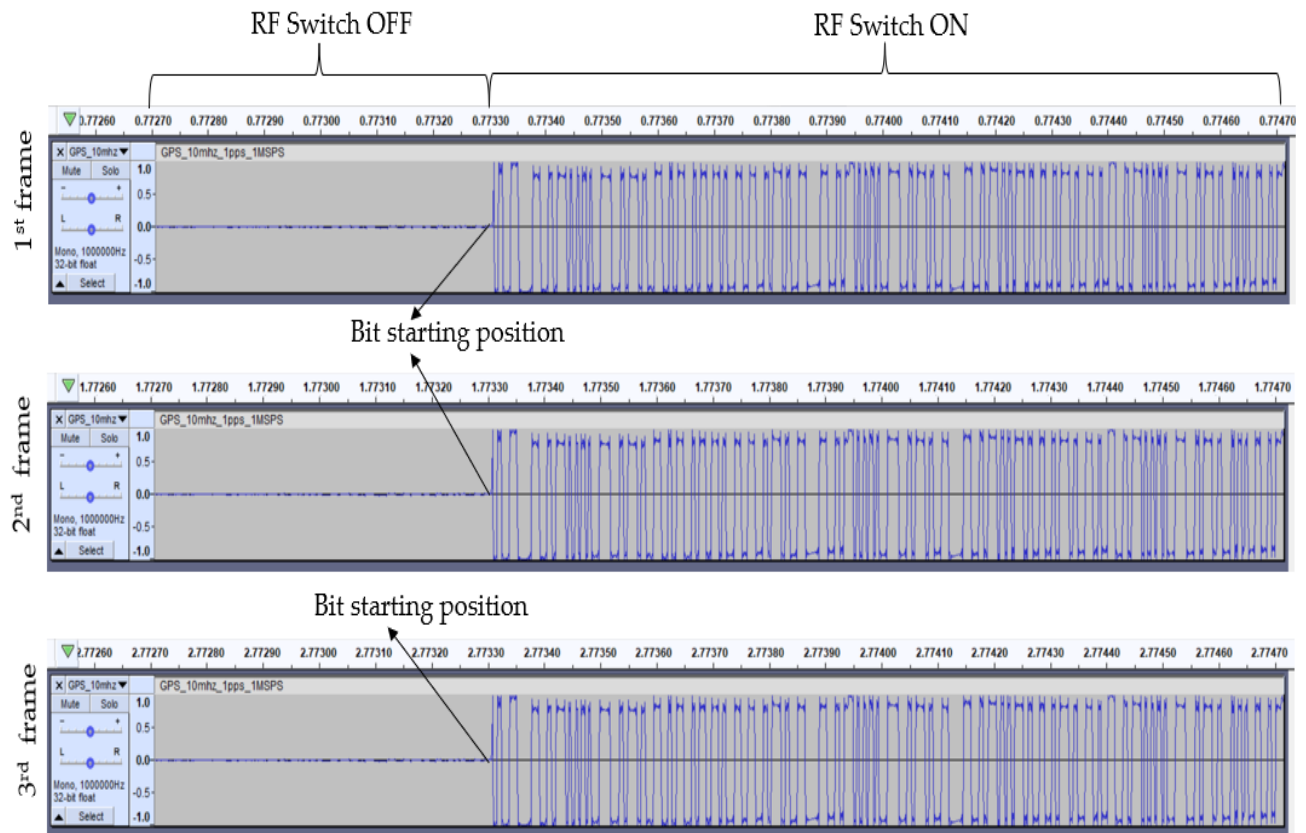


Figure 49. Analysis of data frames from the received signal at 450 MHz and 1 MSPS.

Observations were made on the received data in an interval of every 1 s. The data frames which contain the same information showed that there was no signal distortion due to clock jittering. The positions, patterns, and time for three data frames were analyzed at 0.77330 s,

1.77330 s, and 2.77330 s, respectively. From the analysis, the bit patterns were correctly received without the flipping or shifting of bits, or unwanted noise. Furthermore, the sections of the time stamps when the RF switch is OFF were completely cut off as anticipated. These results demonstrated the efficiency of the system for calculating the TWVC data without distortion of information or incorrect predictions due to clock jittering.

### 5.7 Delayed Time Stamp using Delay Pulse Generator

Since the position of satellites changes continuously in orbit, the signal passes through a different part of the atmosphere and ionosphere each second. Therefore, a new true range and new propagation time delay should be calculated onboard the satellite. If the signal time shift caused by TWVC and TEC can be isolated in each second, TWVC and TEC can be measured from the time delay. In that 1 s, frequency manipulation must be achieved to obtain a high resolution of TWVC from TEC. To simulate the TWVC/TEC time delay (s), a delay pulse generator was connected to the receiving side of each satellite as shown in Figure 26. In this study a time delay of  $\delta T = 0.3$  s was assumed in order to clearly visualize the delay simulation functionality and positions of 1PPS time stamps on both the transmitting and receiving side. This delay was added to a GPS 1PPS signal (yellow) by a delay pulse generator and a delayed pulse (blue) was formed as indicated in Figure 50.

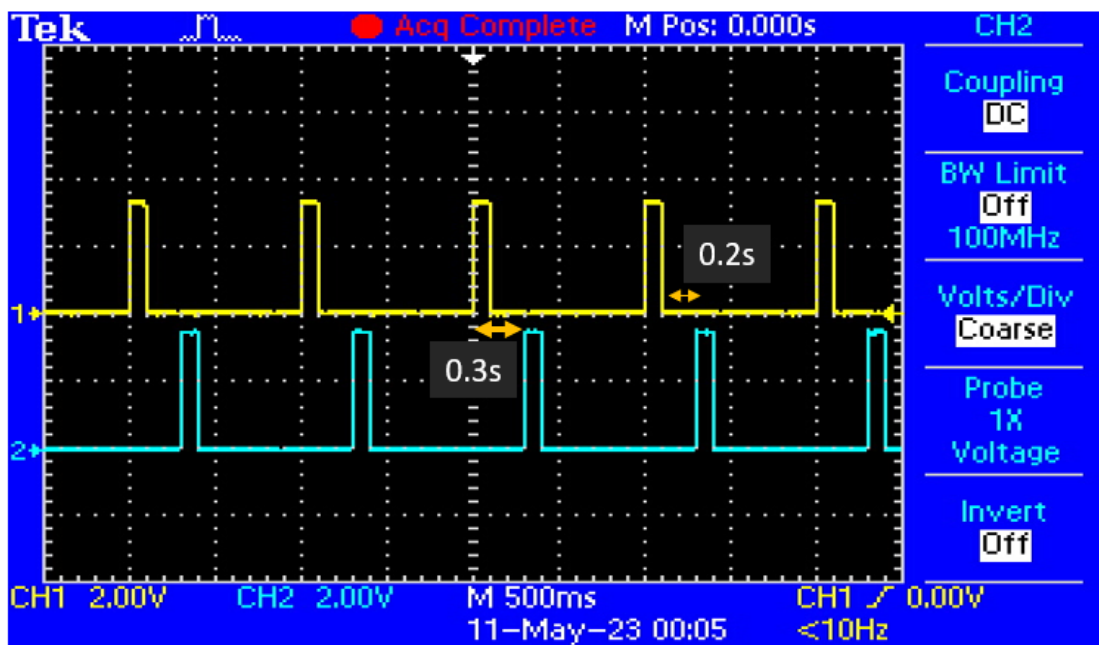


Figure 50. GPS 1PPS pulse (yellow) and a delay pulse (blue) output of delay pulse generator.

As observed on the oscilloscope, the time between the rising or falling edges of the 1PPS pulse and the corresponding delayed pulse was 0.3 s as set on the delay pulse generator. Also, the delay between a rising and a falling edge of the two 1PPS signals,  $d$ , was observed as 0.2 s. When Sat A transmits SS signals to Sat B, the superimposition of these time stamps could be visualized on the received signal as shown in Figure 51.

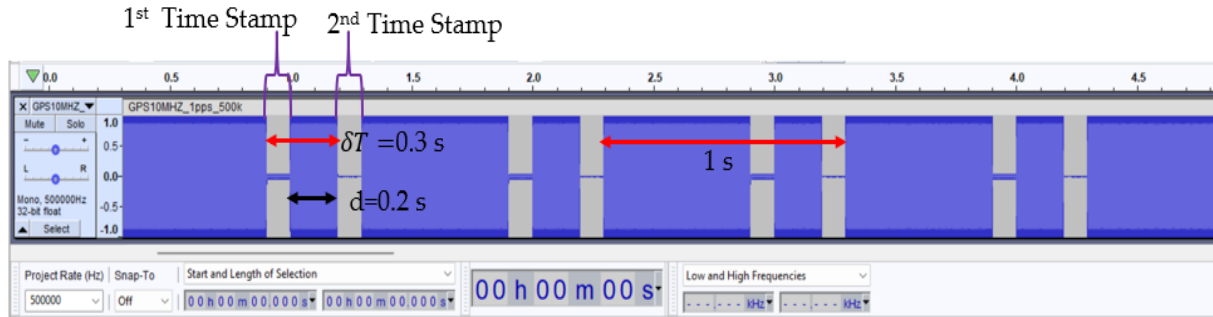


Figure 51. Results of the test with delay pulse generator at 400.15 MHz with large delay.

Four data frames recorded for 4.85 s were observed. This simulation was performed at 400.15 MHz at 500 KSPS. The superimposed fixed time delays of  $\delta T = 0.3$  s and  $d = 0.2$  s, which represent the influence of TWVC and TEC, were observed on the received data frames. To validate the functionality of time delay detection,  $\delta T$  was tuned to 0.13s, sample rate 1 MHz and frequency 460MHz were used as shown in Figure 52.

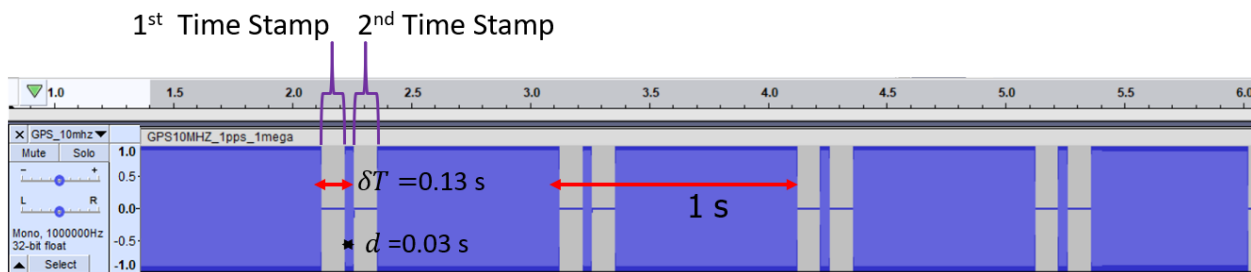


Figure 52. Results of the test with delay pulse generator at 460 MHz with small delay.

Even though the delays provided by the delay pulse generator were fixed irrespective of frequency change, when the delays were tuned up and down at different frequencies the changes in the delay were observed in the data. This proved the efficiency of this system in detecting time delay in orbit where frequency change has an impact on atmospheric geophysical parameters. From the simulation results, the transmitted SS data could also be decoded perfectly. For an in-orbit scenario, since TEC is inversely proportional to the radio frequencies, the 400.15 MHz

frequency is anticipated to give a higher resolution of the measurement values with more delay compared to the 460.00 MHz. TWVC and TEC difference values are then computed with processing algorithms. Finally, TWVC can be deduced following Equations (1) – (9).

### 5.8 ISL Communication Feasibility

To assess the feasibility of the ISL communication network, a link budget has been calculated. Several communication parameters of the ISL network including the SDR output power, SDR transceiver sensitivity, antenna gain, and all losses associated with the communication links were measured. Frequencies of 400.15 MHz and 460.00 MHz were considered in this study. The output transmission power of the SDR transceiver and cable losses were measured as 0.1 W and 0.2 dB, respectively. Sensitivity (dBm) is the minimum power or signal strength that the SDR receiver can detect the transmitted information as having been. The minimum power was obtained by continuously attenuating the transmitted SS signal from Sat A with variable attenuators until the receiver at Sat B could not decode the SS signals. As a way of ensuring the integrity and accuracy of the SDR sensitivity, an RF shield box was utilized as shown in Figure 53. The RF shield provides a typical measurement environment which eliminates the influence of external unwanted noise, interferences, and internal signal reflections that may distort the signal. Moreover, a cable test environment was utilized to determine the optimum and typical sensitivity of the transceiver.

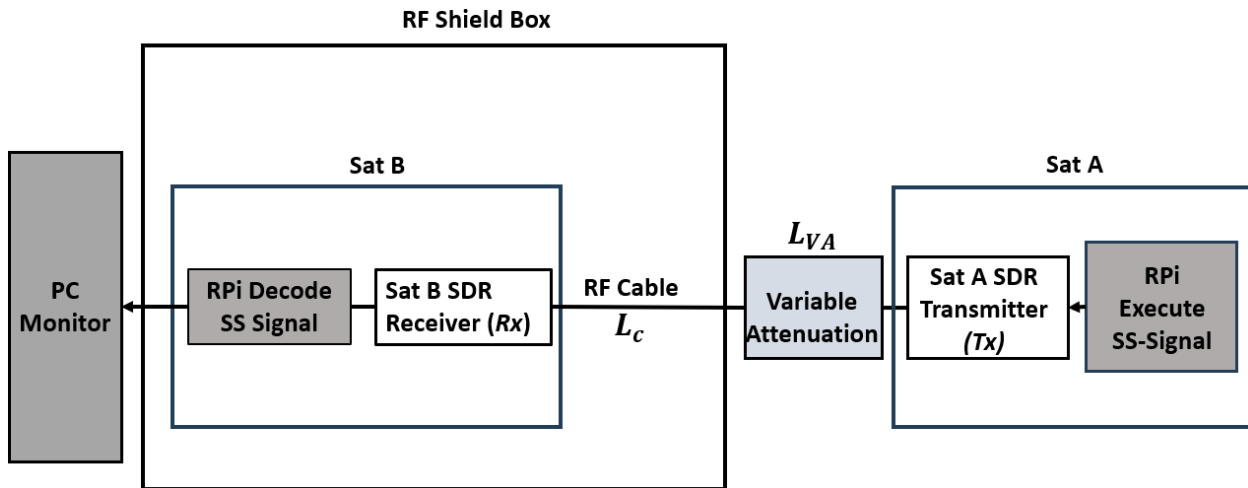


Figure 53. Sensitivity test setup.

The SDR receiver sensitivity value of  $-116$  dBm was obtained based on the following



equation:

$$R_x = T_x - L_{VA} - L_c \quad 20$$

where  $R_x$  (dBm) is the received signal power at Sat B,  $T_x$  (dBm) is the transmitter output power at Sat A,  $L_{VA}$  (dB) is the variable attenuation value, and  $L_c$  (dB) are RF cable losses. Table 12 summarizes the sensitivity test results.

Table 12. Sensitivity test results (o: full packets decoded,  $\Delta$ : partial decoding, x: failed to decode).

$T_x$ (dBm)	$L_{VA}$ (dB)	$L_{VA} + L_c$ (dB)	$R_x$ (dBm)	Success Rate Based on SDR Internal $R_x$ Gain (dB)					
				40	50	60	70	75	76
20	-100	-100.2	-80.2	o					
20	-120	-120.2	-100.2	x	$\Delta$	o			
20	-130	-130.2	-110.2		x	$\Delta$	o		
20	-135	-135.2	-115.2			x	$\Delta$	o	
20	-136	-136.2	-116.2				$\Delta$	$\Delta$	o
20	-137	-137.2	-117.2				x	x	$\Delta$
20	-137	-138.2	-118.2						x

The decoding success rate at Sat B was determined based on the SDR internal receiving gain which was tuned from 40 dB to its maximum value of 76 dB. When the variable attenuation was increased and the signal could not be decoded, the SDR gain values were increased until successful decoding occurred. This process was repeated until the SDR threshold sensitivity of -116.2 dBm was reached at the maximum SDR receiver gain of 76 dBi and the decoding processing was no longer possible. The internal SDR transmitting gain at Sat A was maintained at its maximum value of 89 dB. A maximum separation distance of 4600 km large enough to probe water vapor profiles near Earth was assumed. Since this distance is large, use of a power amplifier was considered. A power amplifier of 30 W that can be used for small satellite sizes was considered [95]. A dipole antenna with theoretical gain of 2.1 dBi was used in the link budget estimations [134]. Other losses including antenna pointing, polarization, and transmission line losses were measured. The obtained link budget showed that the ISL network has a system link margin of -9.2 dB and -10.4 dB at 400.15 MHz and 460.00 MHz, respectively. In order to achieve mission

success, ways of improving this link budget are explained in detail in the discussion section. Table 13 shows the link budget estimation for this mission.

*Table 13. Link budget for ISL network.*

<b>Frequency</b>	<b>MHz</b>	<b>400.15</b>	<b>460.00</b>
<b>Modulation</b>		<b>SS-BPSK</b>	<b>SS-BPSK</b>
<b>Data rate</b>	<b>kbps</b>	<b>0.25</b>	<b>0.25</b>
Satellite A (Transmission)			
Transmitter Output Power	SDR Output	W	0.1
	Amplifier Output	W	30.0
	Total	dBw	14.8
Gain of Transmitting Antenna	dB <sub>i</sub>	2.1	2.1
Transmission Line Loss + Hardware Degradation	dB	3.0	3.0
Equivalent Isotropic Radiated Power (EIRP)	dBw	13.9	13.9
Transmission Path			
Distance between satellites	km	4600	4600
Antenna Pointing Loss	dB	3.0	3.0
Polarization Loss	dB	3.0	3.0
Atmospheric and Ionospheric Losses	dB	1.4	1.4
Free Space Loss	dB	157.7	159.0
Isotropic Signal Level at Spacecraft	dBw	-151.3	-152.5
Satellite B (RX Power Sensitivity)			
Antenna Pointing Loss	dB	3.0	3.0
Gain of Receiving Antenna	dB <sub>i</sub>	2.1	2.1
Transmission Line Loss + Hardware Degradation	dB	3.0	3.0
Received Power at LNA input	dBw	-155.2	-156.4
	dBm	-125.2	-126.4
Required Signal power at the Spacecraft	dBm	-116.0	-116.0
<b>System Link Margin</b>	<b>dB</b>	<b>-9.2</b>	<b>-10.4</b>

## CHAPTER 6

### DISCUSSIONS, CONCLUSION AND FUTURE WORK

#### 6.1 Discussions

All the mission objectives required to deduce the TVWC as a time delay measurement are demonstrated in this study using low-cost commercial off-the-shelf components. Since this study is a continuation of Kyutech SPATIUM satellites, as mentioned in the objectives of SPATIUM-I and SPATIUM-II [24,34,39], the need for the ISL network to enhance 3D mapping of the atmosphere and ionosphere was demonstrated using this system. SPATIUM-I and SPATIUM-II satellites primarily focused on technology demonstrations for the measurement of TEC using a ground-to-satellite communication network. This study deals with both total electron content and atmospheric water vapor measurements using the ISL communication network. Furthermore, the procedure for deducing atmospheric water vapor is presented as a time delay measurement. Kyutech expects to launch a constellation of satellites, which could be more than a thousand satellites, and this makes the desired spatiotemporal resolutions achievable [24]. The ground test results demonstrated that the shortest possible time to reconfigure frequencies and processing has been found to be within 1 s at sampling rates of 1 MSPS and below.

The computed system link margin has a deficiency of at most  $-10.4$  dB when the transmission frequency and separation distance between satellites are 460.00 MHz and 4600 km, respectively. It could be improved by implementing state-of-the-art UHF antennas with high gain. Ochoa et al. [135] proposed the use of a 13 dBi deployable helical antenna with a gain which stows into a volume of approximately 0.5U. In this research a simulation of this antenna was performed as shown in Figure 54. From the simulation the antenna has a directive gain of 13 dBi, efficiency of 98 %, reflection coefficient of  $-8$  dB, voltage standing wave ratio (VSWR) of 3, length of 100 cm and impedance of 150 ohm as anticipated for Helix antennas. By adopting a similar antenna, the system link margin becomes positive and ISL communication network could be established between the satellites. Cross polarized linear arrays such as a Yagi-Uda [136–138] also exhibited superior gains of up to 11.5 dBi at UHF frequencies compared to dipole antennas. Using the Yagi-Uda type of antenna could also be considered a solution for this mission. The use of a directive antennas requires attitude control to point the antenna towards the target [139].

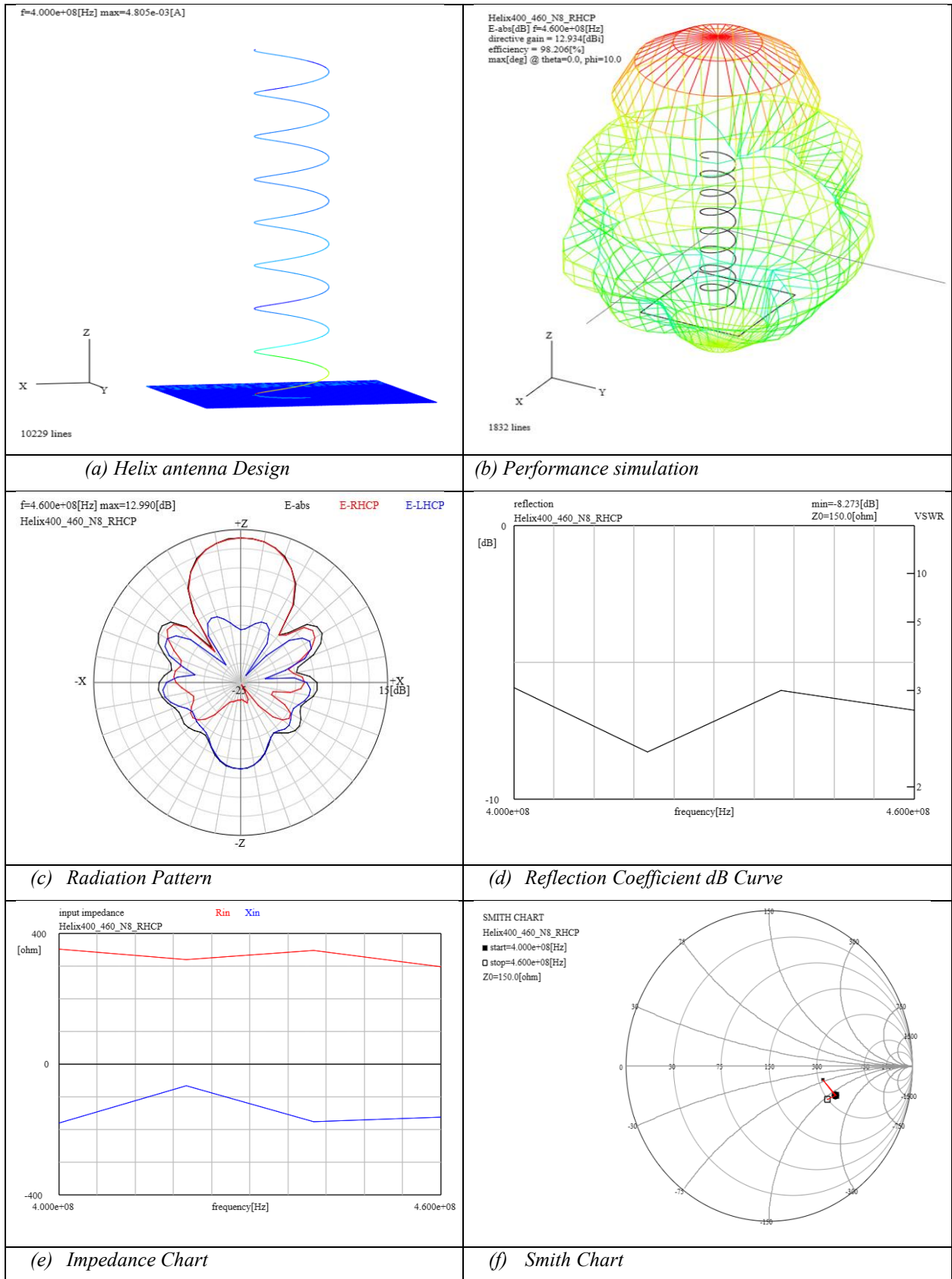


Figure 54. Deployable helix antenna Simulations

Moreover, Abulgasem et al. [137] suggested the utilization of circular polarization in antenna designs for small satellites to eliminate polarization mismatch losses due to antenna misalignment and this guarantees higher link reliability in ISL networks. Furthermore, the TWVC mission subsystem consumes approximately 8.50 W in the transmission mode without a power amplifier. Having a power amplifier [95] integrated into the system could significantly improve the system link margin. On the other hand, this would negatively impact the power budget, mass, and volume of the system depending on the limited resources of a small satellite. As a solution, the use of high-power amplifiers demands either the implementation of supplementary power systems such as deployable solar arrays [140], or an increase in the size of the satellite or a reduction of the mission execution time must to meet the requirements of the limitation factors. If these suggested solutions could be implemented, a positive system link margin will be achieved for the proper ISL communications in orbit.

The GPS used in this research has location accuracy of 2 m. In orbit, the location accuracy may decline due to signal phase shifts which in turn distort the accuracy of the TWVC measurements. Proposition were made to utilize GPS modules with real time kinematics (RTK) correction software's for real time positioning applications preferably the ones that achieves cm or mm accuracy in order to eliminate any distortions. The Table below gives some of the candidates in comparison to ones that have been used on Kyutech satellite projects. Option number 2 (No. 2) has been confirmed and is available on the market.

*Table 14. GPS performance assessments.*

Property	Birds 4	Kitsune	Leopard /Research	No. 1	No. 2	No. 3	No. 4
Mission	Attitude	TEC	Ranging	Flight heritage	Flight heritage	IoT/Rovers	No flight heritage
Brand	MT3329	Fireant	Orion B16	OEM7600	Mosaic-X5	PX1122R	Orion B17
Location Accuracy (m)	2.5-3	10	2	+0.4	+0.1	0.01, 2	1.5
Velocity Accuracy (m/s)	0.5	-	0.1	<0.03	0.03	0.05	0.05

Time accuracy (ns)	100	-	5	<5	<20	12	12
Weight (g)	6	-	1.6	31	6.8	1.7	1.7
Size (mm)	16 x 16 x 6	22 x 17 x 3	12.2 x 16 x 2.9	35 x 55 x 13	31 x 31 x 4	12 x 16 x 3	17 x 22 X 3
Voltage (V) & Current (mA)	3.3, 48	3.3, 45	3.3, 65	3.3,400	3.3, 335	3.3, 50	3.3, 250
Temperature (°C)	-40 to +85	-40 to +85	-40 to +85	-40 to +85	-40 to +85	-40 to +85	-40 to +85
RTK Support	No	No	No	Yes	Yes	Yes	Yes

Some limitations due to the processing power of the RPi were encountered as RPi 4 efficiency declined at sampling rates above 3 MSPS; however, the SPATIUM-II satellite achieved the in-orbit demonstration of SS signal demodulation and time delay detection at 1 MSPS based on the RPi CM3+ module, which has a lower processing power compared to the RPi 4 model B [24,39,46]. Also, during ground tests, it was observed that when multiple processes run in the RPi desktop Ubuntu Linux operating system, communication fluctuations and frequency reconfiguration delays occurred. These can be alleviated using high processing power microprocessors, or implementing software interrupt functions which allow the prioritization of important tasks such as frequency reconfiguration and data processing. Using a lighter OS or running the programs in Ubuntu-based servers could also deliver better performance since all system resources would be dedicated only to server tasks rather than having additional desktop resources [141].

The use of precise atomic clocks such as the CSAC or GPS clock [24,34,40] to alleviate the clock jittering effect on the SDR or other radio transceivers has been demonstrated in SPATIUM-I and SPATIUM-II. In this study, an external 10 MHZ GPS clock has been used to eliminate the jittering error of 35  $\mu$ s that was consistently recurring. As a result, all errors associated with the SDR and instruments' clock jittering were removed, and the bits of information could be perfectly received without noise, shifting or flipping of the information bits.

Furthermore, considering a constellation of more than 1000 satellites, large volumes of data will be captured. In such cases, it is recommended to utilize high-data-rate communication networks such as the S, C, or X bands on the satellite bus for data downlink to the ground [137,142].

## 6.2 Conclusions and Future Work

The mission measurement concept of TWVC is constructed based on radio sensing of the atmosphere. A system design that measures atmospheric water vapor is proposed, the requirements and specifications are determined, and system interfaces and integration are done. A GNU Radio-based transceiver that has the capability of transmitting and receiving SS signal is also implemented. The SS-BPSK has shown good reception and demodulation of SS-transmitted signals with and without delay. All the transmitted data in 1 s intervals are perfectly recovered, and two satellite payloads are utilized to demonstrate the ISL network successfully considering one orbital plane. This research can be further developed to demonstrate the full success criteria of the TWVC mission based on a constellation of more than two satellites in motion and in different orbital planes of the LEO. If that is achieved, 3D mapping of atmospheric water vapor or TEC can be perfectly deduced. Moreover, this paper only considered the ISL network configuration; however, a combination of fixed and mobile ground stations together with ISL networks can also be implemented to ensure a robust system that determines the 3D mapping of TWVC over a wider area. The test results demonstrate the possibility of reconfiguring the frequency onboard the satellite with the proposed algorithms. The determined duration of frequency translation is measured within 1 s as was proposed. The time delay estimation method with the current configuration has also been successful, and it can be recommended as an effective technique for TWVC or TEC calculations from the signal propagation time delay. For future studies, sweeping through much lower available meteorological frequency bands could be considered as a way to improve mission measurement accuracy. This is because lower frequency bands are more influenced by atmospheric geophysical parameters. However, multiple antennas calibrated for the selected frequencies must be implemented. Also, possible phase delays and errors that may occur in orbit due to the positioning accuracy of the GPS or frequency reconfigurations shall be scrutinized as part of the next objectives. Clock jittering is also successfully removed to ensure the incoming and outgoing signals are not distorted with instrument and clock offsets. This improves mission accuracy within 35  $\mu$ s when a 10 MHz atomic clock such GPS clock is used. Low orbital attitude, lower frequency bands, and a constellation of more than 1000 satellites can give this method improved accuracy and high spatiotemporal resolutions compared to conventional techniques. Based on these results, the proposed system demonstrated that it is feasible to conduct atmospheric measurements using the radio signals onboard small satellites.

The acquired data will be incorporated into the global atmospheric databases of geophysical parameters for climate and weather prediction models. Participating and contributing to ongoing research initiatives are necessary for integrating obtained data into global atmospheric databases for climate and weather prediction models, in addition to adherence to the accepted standards and data sharing agreements. The 3D-mapped data of the TWVC will be aligned with standardized formats, units, and metadata acknowledged by the atmospheric research community. Additionally, partnership with organizations that specialize in collecting and distributing atmospheric data will be considered. To guarantee seamless integration of the acquired data with existing global atmospheric databases, data quality control will be conducted by institutions that specialize in data evaluation and validation. Institutions and researchers involved in atmospheric modelling and research will be granted open access to the acquired data. Finally, the institute will hold workshops and forums that bring together researchers, modelers, and data providers to discuss integration challenges, strategies, and opportunities. This research will be implemented in future Kyutech satellite projects involving radio sensing of the atmosphere



## APPENDIXs

### Systems Integration Configuration

#### A. Integration configuration of RPi GNU and USRP SDR

##### Procedure:

1) `sudo apt update && sudo apt upgrade`

2) `lsb_release -a`

```
LSB modules are available.
Distributor ID: Ubuntu
Description: Ubuntu 20.04 LTS
Release: 20.04
Codename: bionic
```

3) `sudo apt-get update`

4) `sudo apt-get dist-upgrade`

5) `sudo add-apt-repository ppa:ettusresearch/uhd`

6) `sudo apt-get update`

7) `sudo apt-get install libuhd-dev libuhd003.010.003 uhd-host`

```
Reading package lists... Done
Building dependency tree
Reading state information... Done
```

8) `uhd_usrp_probe`

```
linux; GNU C++ version 8.2.0; Boost 106501; UHD 4.1.0.4-release
Error: LookupError: KeyError: No devices found for ----->
Empty Device Address
```

9) `sudo /usr/lib/uhd/uhd_images_downloader.py`

```
[INFO] Images download complete.
```

10) `uhd_usrp_probe`

```
linux; GNU C++ version 8.2.0; Boost_106501; UHD_4.1.0.4-release
[WARNING] [B200] EnvironmentError: IOError: Could not find path for image:
usrp b200 fw.hex
Using images directory: <no images directory located>
Set the environment variable 'UHD_IMAGES_DIR' appropriately or follow the below instructions
to download the images package.
Please run:
"/usr/lib/x86_64-linux-gnu/uhd/uhd_images_downloader.py"
Error: LookupError: KeyError: No devices found for ----->
Empty Device Address
```

```
11) ramsy@sdr:/usr/lib/uhd/utis$ sudo cp uhd-usrp.rules /etc/udev/rules.d/
sudo udevadm control --reload-rules
sudo udevadm trigger
```

```
12) uhd_usrp_probe
```

```
[INFO] [UHD] linux; GNU C++ version 8.2.0; Boost 106501; UHD 4.1.0.4-release
[WARNING] [B200] EnvironmentError: IOError: Could not find path for image:
usrp_b200_fw.hex
Using images directory: <no images directory located>
Set the environment variable 'UHD_IMAGES_DIR' appropriately or follow the below instructions
to download the images package.
Please run:
"/usr/lib/x86_64-linux-gnu/uhd/utis/uhd_images_downloader.py"
Error: LookupError: KeyError: No devices found for ---->
Empty Device Address
```

### The Key is here use sudo when you want to check uhd usrp probe

```
13) ramsy@sdr:/usr/share/uhd/images$ sudo uhd usrp probe
```

```
Linux; GNU C++ version 8.2.0; Boost 106501; UHD 4.1.0.4-release
[INFO] [B200] Loading firmware image: /usr/share/uhd/images/usrp_b200_fw.hex...
[INFO] [B200] Detected Device: B205mini
[INFO] [B200] Loading FPGA image: /usr/share/uhd/images/usrp_b205mini_fpga.bin...
[INFO] [B200] Operating over USB 2.
[INFO] [B200] Initialize CODEC control...
[INFO] [B200] Initialize Radio control...
[INFO] [B200] Performing register loopback test...
[INFO] [B200] Register loopback test passed
[INFO] [B200] Setting master clock rate selection to 'automatic'.
[INFO] [B200] Asking for clock rate 16.000000 MHz...
[INFO] [B200] Actually got clock rate 16.000000 MHz.
```

```
14) ramsy@sdr:/usr/share/uhd/images$ sudo apt install gnuradio
```

Open GNU Radio and SDR connected and run a program. It will not work coz of software firmware compatibility error in GNU radio

In GNU Radio Check on this message:

```
Warning: failed to XInitThreads()
linux; GNU C++ version 8.2.0; Boost 106501; UHD_003.010.003.000-0-unknown
```

# Download the zipped file of uhd images on <https://files.ettus.com/binaries/images/> dated 2020/01/22 54MB @ 12:09# with same name UHD\_003.010.003.000-0-unknown when u download it buditsa muzip. Just copy the inside immediate folder outside.

```
15) ramsy@sdr:/usr/share/uhd/images$ cd ..
```

```
16) ramsy@sdr:/usr/share/uhd$ cd ..
```

```
17) ramsy@sdr:/usr/share$ cd uhd
```

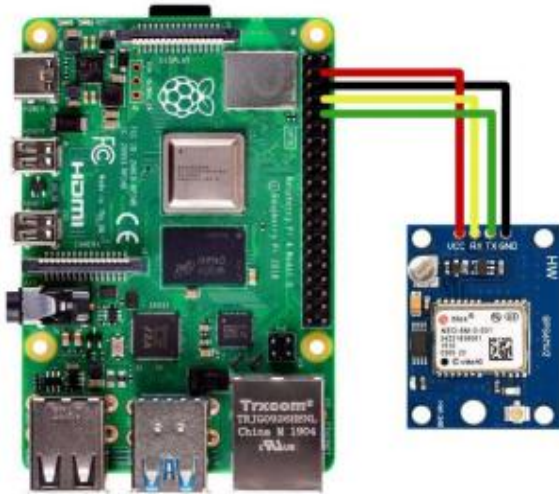
```
18) ramsy@sdr:/usr/share/uhd$ ls
```

```
cal images rfnoe
```

- 19) ramsy@sdr:/usr/share/uhd/images\$ cd ..
- 20) ramsy@sdr:/usr/share/uhd\$ sudo mv images images.org
- 21) ramsy@sdr:/usr/share/uhd\$ ls ~  
Desktop Downloads Music Public top\_block.py Videos  
Documents examples.desktop Pictures Templates usrp\_b205\_test1.gz
- 22) ramsy@sdr:/usr/share/uhd\$ ls ~/Downloads  
uhd-images\_003.010.003.000-rc2 uhd-images\_003.010.003.000-rc2.tar.gz
- 23) ramsy@sdr:/usr/share/uhd\$ ls ~/Downloads/uhd-images\_003.010.003.000-rc2  
share
- 24) ramsy@sdr:/usr/share/uhd\$ ls ~/Downloads/uhd-images\_003.010.003.000-rc2/share  
uhd
- 25) ramsy@sdr:/usr/share/uhd\$ ls ~/Downloads/uhd-images\_003.010.003.000-rc2/share/uhd  
images
- 26) ramsy@sdr:/usr/share/uhd\$ ls ~/Downloads/uhd-images\_003.010.003.000-rc2/share/uhd/images
- 27) ramsy@sdr:/usr/share/uhd\$ sudo cp -r ~/Downloads/uhd-images\_003.010.003.000-rc2/share/uhd/images .
- 28) ramsy@sdr:/usr/share/uhd\$ ls  
cal images images.org rfnoe
- 29) ramsy@sdr:/usr/share/uhd\$
- 30) cd~
- 31) sudo apt install canberra-gtk\*

Open GNU Radio and Run it. It should work

## B. RPi and GPS Integration



The first thing, is to enable the UART line by configuring the boot files (usercfg, ) using the commands below:

1. `sudo nano /boot/firmware/syscfg.txt`

```
File Edit View Search Terminal Help
GNU nano 2.9.3 /boot/firmware/syscfg.txt
# This file is intended to contain system-made configuration changes. User
# configuration changes should be placed in "usercfg.txt". Please refer to the
# README file for a description of the various configuration files on the boot
# partition.
enable_uart=6
dtparam=i2c_arm=on
dtparam=spi=on
include nobtcf.txt
```

This allows enabling of 6 UART lines, i2C and SPI lines on the RPi. Include the nobtcf.txt file which allows configuration of the pins on the RPi.

2. `sudo nano /boot/firmware/nobtcmd.txt`

```
File Edit View Search Terminal Help
GNU nano 2.9.3 /boot/firmware/nobtcmd.txt
set.ifnames=0 dwc_otg.lpm_enable=0 console=ttyAMA0,115200 console=tty1 root=LABEL=writable rootfstype=ext4 elevator=deadline rootwait fixrtc
```

3. `sudo nano /boot/firmware/usercfg.txt`

```
1
ubuntu@ubuntu: ~
V File Edit View Search Terminal Help
GNU nano 2.9.3 /boot/firmware/usercfg.txt
# Place "config.txt" changes (dtparam, dtoverlay, disable_overscan, etc.) in
# this file. Please refer to the README file for a description of the various
# configuration files on the boot partition.
dtoverlay=uart2

dtoverlay=uart3

dtoverlay=uart4

dtoverlay=uart5

dtoverlay=pps-gpio, gpiopin=18
```

Enable UART2 =>RPI-GPIO14-Tx => Rx on GPS

UART 3=> RPi-GPIO15 -Rx=> Tx on GPS

UART4=>GPIO17and UART 5=>GPIO27 are redundance lines

Enable 1PPS to use RPi GPIO 18

Secondly interface the RPi to GPS module (ORION B16) in order to get and store GPS location and time data. The following commands are needed.:

```
sudo apt-get install gpsd gpsd-clients
```

```
sudo apt-get install python3-pip
```

```
sudo pip3 install gps3
```

```
sudo nano /etc/default/gpsd
```

```
sudo systemctl enable gpsd.socket
```

```
sudo pptest /dev/pps0 #confirm 1pps
```

```
sudo gpsmon #obtain GPS data
```

```
sudo cgps #obtain GPS data
```

## 1. Python code to confirm \$GPGGA latitude, longitude, and time data as well as comparing the data with google map.

```
'''
GPS Interfacing with Raspberry Pi using Python
Ramson
'''
import serial          #import serial package
from time import sleep
import webbrowser      #import package for opening link in browser
import sys             #import system package

def GPS_Info():
    global NMEA_buff
    global lat_in_degrees
    global long_in_degrees
    nmea_time = []
    nmea_latitude = []
    nmea_longitude = []
    nmea_time = NMEA_buff[0]          #extract time from GPGGA string
    nmea_latitude = NMEA_buff[1]      #extract latitude from GPGGA string
    nmea_longitude = NMEA_buff[3]     #extract longitude from GPGGA string

    print("NMEA Time: ", nmea_time, '\n')
    print("NMEA Latitude: ", nmea_latitude, "NMEA Longitude: ", nmea_longitude, '\n')

    lat = float(nmea_latitude)        #convert string into float for calculation
    longi = float(nmea_longitude)     #convert string into float for calculation

    lat_in_degrees = convert_to_degrees(lat) #get latitude in degree decimal format
    long_in_degrees = convert_to_degrees(longi) #get longitude in degree decimal format

#convert raw NMEA string into degree decimal format
def convert_to_degrees(raw_value):
    decimal_value = raw_value/100.00
    degrees = int(decimal_value)
    mm_mmmm = (decimal_value - int(decimal_value))*0.6
    position = degrees + mm_mmmm
    position = "%.4f" % (position)
    return position

gpvga_info = "$GPGGA,"
ser = serial.Serial ("/dev/ttyS0")      #Open port with baud rate
```

```

GPGGA_buffer = 0
NMEA_buff = 0
lat_in_degrees = 0
long_in_degrees = 0

try:
    while True:
        received_data = (str)(ser.readline()) #read NMEA string received
        GPGGA_data_available = received_data.find(gpgga_info) #check for NMEA GPGGA string
        if (GPGGA_data_available>0):
            GPGGA_buffer = received_data.split("$GPGGA,")[1] #store data coming after "$GPGGA," string
            NMEA_buff = (GPGGA_buffer.split(",")) #store comma separated data in buffer
            GPS_Info() #get time, latitude, longitude

            print("lat in degrees:", lat_in_degrees," long in degree: ", long_in_degrees, '\n')
            map_link = 'http://maps.google.com/?q=' + lat_in_degrees + ',' + long_in_degrees #create link to plot location on Google map
            print("<<<<<<<<<<<<press ctrl+c to plot location on google maps>>>>>>>>>>>>\n") #press ctrl+c to plot on map and exit
            print("-----\n")

except KeyboardInterrupt:
    webbrowser.open(map_link) #open current position information in google map
    sys.exit(0)

```

## 2. C code to confirm \$GPGGA latitude, longitude, and time data as well as comparing the data with google map.

```
/*
GPS Interfacing with Raspberry Pi using C (Ramson)
Ramson
*/

#include <stdio.h>
#include <string.h>
#include <errno.h>

#include <wiringPi.h>
#include <wiringSerial.h>

int main ()
{
    int serial_port;
    char dat_buff[100],GGA_code[3];
    unsigned char IsitGGAstring=0;
    unsigned char GGA_index=0;
    unsigned char is_GGA_received_completely = 0;

    if((serial_port = serialOpen ("/dev/ttyS0", 9600)) < 0) /* open serial port */
    {
        fprintf(stderr, "Unable to open serial device: %s\n", strerror (errno));
        return 1 ;
    }

    if(wiringPiSetup () == -1) /* initializes wiringPi setup */
    {
        fprintf(stdout, "Unable to start wiringPi: %s\n", strerror (errno));
        return 1 ;
    }

    while(1){

        if(serialDataAvail (serial_port) ) /* check for any data available on serial port */
        {
            dat = serialGetchar(serial_port); /* receive character serially */
            if(dat == '$'){
                IsitGGAstring = 0;
                GGA_index = 0;
            }
            else if(IsitGGAstring ==1){
```



```

    buff[GGA_index++] = dat;
    if(dat=='r')
        is_GGA_received_completely = 1;
    }
else if(GGA_code[0]=='G' && GGA_code[1]=='G' && GGA_code[2]=='A'){
    IsitGGAstring = 1;
    GGA_code[0]= 0;
    GGA_code[1]= 0;
    GGA_code[2]= 0;
    }
else{
    GGA_code[0] = GGA_code[1];
    GGA_code[1] = GGA_code[2];
    GGA_code[2] = dat;
    }
}
if(is_GGA_received_completely==1){
    printf("GGA: %s",buff);
    is_GGA_received_completely = 0;
}
}
return 0;

```

### C. SS-BPSK\_transceiver\_with\_XMLRPC server algorithm

```
#!/usr/bin/env python3
# -*- coding: utf-8 -*-

#
# SPDX-License-Identifier: GPL-3.0
#
# GNU Radio Python Flow Graph
# Title: Not titled yet
# Author: Ramsy
# GNU Radio version: v3.8.2.0-57-gd71cd177

from distutils.version import StrictVersion

if __name__ == '__main__':
    import ctypes
    import sys
    if sys.platform.startswith('linux'):
        try:
            x11 = ctypes.cdll.LoadLibrary('libX11.so')
            x11.XInitThreads()
        except:
            print("Warning: failed to XInitThreads()")

    from PyQt5 import Qt
    from gnuradio import qtgui
    from gnuradio.filter import firdec
    import sip
    from gnuradio import analog
    from gnuradio import blocks
    from gnuradio import channels
    from gnuradio import digital
    from gnuradio import filter
    from gnuradio import gr
    import sys
    import signal
    from argparse import ArgumentParser
    from gnuradio.eng_arg import eng_float, intx
    from gnuradio import eng_notation
    from gnuradio import uhd
    import time
    from gnuradio.qtgui import Range, RangeWidget
    try:
        from xmlrpc.server import SimpleXMLRPCServer
    except ImportError:
        from SimpleXMLRPCServer import SimpleXMLRPCServer
    import threading

    from gnuradio import qtgui

class Thesis_SS_BPSK_XMLRPC_Tuning_Server_Transceiver_Program(gr.top_block, Qt.QWidget):

    def __init__(self):
        gr.top_block.__init__(self, "Not titled yet")
        Qt.QWidget.__init__(self)
        self.setWindowTitle("Not titled yet")
        qtgui.util.check_set_qss()
        try:
            self.setWindowIcon(Qt.QIcon.fromTheme('gnuradio-gre'))
        except:
            pass
        self.top_scroll_layout = Qt.QVBoxLayout()
        self.setLayout(self.top_scroll_layout)
        self.top_scroll = Qt.QScrollArea()
        self.top_scroll.setFrameStyle(Qt.QFrame.NoFrame)
        self.top_scroll_layout.addWidget(self.top_scroll)
        self.top_scroll.setWidgetResizable(True)
        self.top_widget = Qt.QWidget()
        self.top_scroll.setWidget(self.top_widget)
```

```

self.top_layout = Qt.QVBoxLayout(self.top_widget)
self.top_grid_layout = Qt.QGridLayout()
self.top_layout.addLayout(self.top_grid_layout)

self.settings = Qt.QSettings("GNU Radio", "Thesis SS BPSK XMLRPC Tuning Server Transceiver Program")

try:
    if StrictVersion(Qt.qVersion()) < StrictVersion("5.0.0"):
        self.restoreGeometry(self.settings.value("geometry").toByteArray())
    else:
        self.restoreGeometry(self.settings.value("geometry"))
except:
    pass

#####
# Variables
#####
self.sps = sps = 16
self.nfilts = nfilts = 32
self.excess_bw = excess_bw = 0.350
self.time_offset = time_offset = 1
self.samp_rate = samp_rate = 1000000
self.rrc_taps = rrc_taps = firdes.root_raised_cosine(nfilts, nfilts, 1.0/float(sps), excess_bw, 11*sps*nfilts)
self.rmt_freq = rmt_freq = 460000000
self.noise_volt = noise_volt = 0.0001
self.noise_taps = noise_taps = ([1.0, 0.25-0.25j, 0.5+0.10j, 0.3+0.2j])
self.freq_offset = freq_offset = 0
self.eb = eb = 0.22
self.bpsk = bpsk = digital.constellation_bpsk().base()
self.TxGain = TxGain = 40
self.RxGain = RxGain = 65

#####
# Blocks
#####
self.time_offset_range = Range(0.999, 1.001, 0.000100, 1, 200)
self.time_offset_win = RangeWidget(self.time_offset_range, self.set_time_offset, 'Channel Timing Offset', "counter slider", float)
self.top_grid_layout.addWidget(self.time_offset_win)
self.noise_volt_range = Range(0, 1, 0.01, 0.0001, 200)
self.noise_volt_win = RangeWidget(self.noise_volt_range, self.set_noise_volt, 'Channel Noise Voltage', "counter slider", float)
self.top_grid_layout.addWidget(self.noise_volt_win)
self.freq_offset_range = Range(-0.100, 0.100, 0.001, 0, 200)
self.freq_offset_win = RangeWidget(self.freq_offset_range, self.set_freq_offset, 'Channel Freq offset', "counter slider", float)
self.top_grid_layout.addWidget(self.freq_offset_win)
self.xmlrpc_server_0 = SimpleXMLRPCServer(("localhost", 8000), allow_none=True)
self.xmlrpc_server_0.register_instance(self)
self.xmlrpc_server_0_thread = threading.Thread(target=self.xmlrpc_server_0.serve_forever)
self.xmlrpc_server_0_thread.daemon = True
self.xmlrpc_server_0_thread.start()
self.uhd_usrp_source_0 = uhd.usrp_source(
    ", ".join("**, **"),
    uhd.stream_args(
        cpu_format="fc32",
        args="",
        channels=list(range(0,1)),
    ),
)
self.uhd_usrp_source_0.set_center_freq(460e6, 0)
self.uhd_usrp_source_0.set_gain(65, 0)
self.uhd_usrp_source_0.set_antenna('RX2', 0)
self.uhd_usrp_source_0.set_bandwidth(1e6, 0)
self.uhd_usrp_source_0.set_samp_rate(samp_rate)
self.uhd_usrp_source_0.set_time_unknown_pps(uhd.time_spec())
self.uhd_usrp_sink_0 = uhd.usrp_sink(
    ", ".join("**, **"),
    uhd.stream_args(
        cpu_format="fc32",
        args="",
        channels=list(range(0,1)),
    ),
)

```

```

)
self.uhd_usrp_sink_0.set_center_freq(rmt_freq, 0)
self.uhd_usrp_sink_0.set_gain(40, 0)
self.uhd_usrp_sink_0.set_antenna('TX/RX', 0)
self.uhd_usrp_sink_0.set_bandwidth(1e6, 0)
self.uhd_usrp_sink_0.set_samp_rate(samp_rate)
self.uhd_usrp_sink_0.set_time_unknown_pps(uhd.time_spec())
self.qtgui_time_sink_x_0_0_1 = qtgui.time_sink_f(
    1024, #size
    samp_rate, #samp_rate
    "Signal Processing Time @ 460MHz", #name
    1 #number of inputs
)
self.qtgui_time_sink_x_0_0_1.set_update_time(0.10)
self.qtgui_time_sink_x_0_0_1.set_y_axis(-1, 1)

self.qtgui_time_sink_x_0_0_1.set_y_label('Amplitude', '')

self.qtgui_time_sink_x_0_0_1.enable_tags(False)
self.qtgui_time_sink_x_0_0_1.set_trigger_mode(qtgui.TRIG_MODE_FREE, qtgui.TRIG_SLOPE_POS, 0.0, 0, 0, "")
self.qtgui_time_sink_x_0_0_1.enable_autoscale(True)
self.qtgui_time_sink_x_0_0_1.enable_grid(True)
self.qtgui_time_sink_x_0_0_1.enable_axis_labels(True)
self.qtgui_time_sink_x_0_0_1.enable_control_panel(True)
self.qtgui_time_sink_x_0_0_1.enable_stem_plot(False)

labels = ['RxData', 'TxData', ".", ".",
          ".", ".", ".", "."]
widths = [1, 1, 1, 1, 1,
          1, 1, 1, 1, 1]
colors = ['blue', 'red', 'green', 'black', 'cyan',
          'magenta', 'yellow', 'dark red', 'dark green', 'dark blue']
alphas = [1.0, 1.0, 1.0, 1.0, 1.0,
          1.0, 1.0, 1.0, 1.0, 1.0]
styles = [1, 1, 1, 1, 1,
          1, 1, 1, 1, 1]
markers = [-1, -1, -1, -1, -1,
           -1, -1, -1, -1, -1]

for i in range(1):
    if len(labels[i]) == 0:
        self.qtgui_time_sink_x_0_0_1.set_line_label(i, "Data {0}".format(i))
    else:
        self.qtgui_time_sink_x_0_0_1.set_line_label(i, labels[i])
        self.qtgui_time_sink_x_0_0_1.set_line_width(i, widths[i])
        self.qtgui_time_sink_x_0_0_1.set_line_color(i, colors[i])
        self.qtgui_time_sink_x_0_0_1.set_line_style(i, styles[i])
        self.qtgui_time_sink_x_0_0_1.set_line_marker(i, markers[i])
        self.qtgui_time_sink_x_0_0_1.set_line_alpha(i, alphas[i])

self.qtgui_time_sink_x_0_0_1_win = sip.wrapinstance(self.qtgui_time_sink_x_0_0_1.pyqwidget(), Qt.QWidget)
self.top_grid_layout.addWidget(self.qtgui_time_sink_x_0_0_1_win)
self.qtgui_sink_x_0_1_0 = qtgui.sink_c(
    1024, #ffsize
    firdes.WIN_BLACKMAN_hARRIS, #wintype
    0, #fc
    samp_rate, #bw
    'PlotD', #name
    True, #plotfreq
    True, #plotwaterfall
    True, #plottime
    True #plotconst
)
self.qtgui_sink_x_0_1_0.set_update_time(1.0/10)
self.qtgui_sink_x_0_1_0_win = sip.wrapinstance(self.qtgui_sink_x_0_1_0.pyqwidget(), Qt.QWidget)

```

```

self.qtgui_sink_x_0_1_0.enable_rf_freq(False)

self.top_grid_layout.addWidget(self.qtgui_sink_x_0_1_0_win)
self.digital_pfb_clock_sync_xxx_0_0 = digital.pfb_clock_sync_ccf(sps, 62.8e-3, rrc_taps, 32, 16, 1.5, 1)
self.digital_costas_loop_cc_0 = digital.costas_loop_cc(0.0628, 2, False)
self.digital_constellation_modulator_0 = digital.generic_mod(
    constellation=bpsk,
    differential=False,
    samples_per_symbol=sps,
    pre_diff_code=True,
    excess_bw=excess_bw,
    verbose=False,
    log=False)
self.digital_constellation_decoder_cb_0 = digital.constellation_decoder_cb(bpsk)
self.dc_blocker_xx_0 = filter.dc_blocker_cc(1024, True)
self.channels_channel_model_0_0 = channels.channel_model(
    noise_voltage=noise_volt,
    frequency_offset=freq_offset,
    epsilon=time_offset,
    taps=noise_taps,
    noise_seed=0,
    block_tags=False)
self.blocks_wavfile_sink_0 = blocks.wavfile_sink('C:\Users\Ramsy\Programs\output.wav', 1, samp_rate, 8)
self.blocks_vector_source_x_0_0 = blocks.vector_source_b((0x46, 0x46, 0x30, 0x34, 0x30, 0x38, 0x30, 0x34, 0x30, 0x36, 0x30,
0x34, 0x32, 0x33, 0x31, 0x33, 0x30, 0x35, 0x30, 0x2E, 0x34, 0x31, 0x33, 0x33, 0x35, 0x33, 0x2E, 0x35, 0x31, 0x35, 0x31), True, 1, [])
self.blocks_unpack_k_bits_bb_0_0 = blocks.unpack_k_bits_bb(8)
self.blocks_file_sink_1 = blocks.file_sink(gr.sizeof_char*1, 'C:\Users\Ramsy\Programs\ouput.bin', False)
self.blocks_file_sink_1.set_unbuffered(True)
self.blocks_file_sink_0_1 = blocks.file_sink(gr.sizeof_char*1, 'C:\Users\Ramsy\Programs\input.bin', False)
self.blocks_file_sink_0_1.set_unbuffered(True)
self.blocks_char_to_float_0_0 = blocks.char_to_float(1, 1)
self.analog_age_xx_0 = analog.age_cc(1e-4, 1.0, 1.0)
self.analog_age_xx_0.set_max_gain(65536)
self.TxGain_range = Range(10, 100, 1, 40, 200)
self.TxGain_win = RangeWidget(self.TxGain_range, self.set_TxGain, 'TxGain', "counter slider", float)
self.top_grid_layout.addWidget(self.TxGain_win)
self.RxGain_range = Range(10, 100, 1, 65, 200)
self.RxGain_win = RangeWidget(self.RxGain_range, self.set_RxGain, 'RxGain', "counter slider", float)
self.top_grid_layout.addWidget(self.RxGain_win)

#####
# Connections
#####
self.connect((self.analog_age_xx_0, 0), (self.digital_pfb_clock_sync_xxx_0_0, 0))
self.connect((self.blocks_char_to_float_0_0, 0), (self.blocks_wavfile_sink_0, 0))
self.connect((self.blocks_char_to_float_0_0, 0), (self.qtgui_time_sink_x_0_0_1, 0))
self.connect((self.blocks_unpack_k_bits_bb_0_0, 0), (self.blocks_file_sink_0_1, 0))
self.connect((self.blocks_vector_source_x_0_0, 0), (self.blocks_unpack_k_bits_bb_0_0, 0))
self.connect((self.blocks_vector_source_x_0_0, 0), (self.digital_constellation_modulator_0, 0))
self.connect((self.channels_channel_model_0_0, 0), (self.uhd_usrp_sink_0, 0))
self.connect((self.dc_blocker_xx_0, 0), (self.analog_age_xx_0, 0))
self.connect((self.digital_constellation_decoder_cb_0, 0), (self.blocks_char_to_float_0_0, 0))
self.connect((self.digital_constellation_decoder_cb_0, 0), (self.blocks_file_sink_1, 0))
self.connect((self.digital_constellation_modulator_0, 0), (self.channels_channel_model_0_0, 0))
self.connect((self.digital_costas_loop_cc_0, 0), (self.digital_constellation_decoder_cb_0, 0))
self.connect((self.digital_costas_loop_cc_0, 0), (self.qtgui_sink_x_0_1_0, 0))
self.connect((self.digital_pfb_clock_sync_xxx_0_0, 0), (self.digital_costas_loop_cc_0, 0))
self.connect((self.uhd_usrp_source_0, 0), (self.dc_blocker_xx_0, 0))

def closeEvent(self, event):
    self.settings = Qt.QSettings("GNU Radio", "Thesis_SS_BPSK_XMLRPC_Tuning_Server_Transceiver_Program")
    self.settings.setValue("geometry", self.saveGeometry())
    event.accept()

def get_sps(self):
    return self.sps

```

```

def set_sps(self, sps):
    self.sps = sps
    self.set_rrc_taps(firdes.root_raised_cosine(self.nfilts, self.nfilts, 1.0/float(self.sps), self.excess_bw, 11*self.sps*self.nfilts))

def get_nfilts(self):
    return self.nfilts

def set_nfilts(self, nfilts):
    self.nfilts = nfilts
    self.set_rrc_taps(firdes.root_raised_cosine(self.nfilts, self.nfilts, 1.0/float(self.sps), self.excess_bw, 11*self.sps*self.nfilts))

def get_excess_bw(self):
    return self.excess_bw

def set_excess_bw(self, excess_bw):
    self.excess_bw = excess_bw
    self.set_rrc_taps(firdes.root_raised_cosine(self.nfilts, self.nfilts, 1.0/float(self.sps), self.excess_bw, 11*self.sps*self.nfilts))

def get_time_offset(self):
    return self.time_offset

def set_time_offset(self, time_offset):
    self.time_offset = time_offset
    self.channels_channel_model_0_0.set_timing_offset(self.time_offset)

def get_samp_rate(self):
    return self.samp_rate

def set_samp_rate(self, samp_rate):
    self.samp_rate = samp_rate
    self.qtgui_sink_x_0_1_0.set_frequency_range(0, self.samp_rate)
    self.qtgui_time_sink_x_0_0_1.set_samp_rate(self.samp_rate)
    self.uhd_usrp_sink_0.set_samp_rate(self.samp_rate)
    self.uhd_usrp_source_0.set_samp_rate(self.samp_rate)

def get_rrc_taps(self):
    return self.rrc_taps

def set_rrc_taps(self, rrc_taps):
    self.rrc_taps = rrc_taps
    self.digital_pfb_clock_sync_xxx_0_0.update_taps(self.rrc_taps)

def get_rmt_freq(self):
    return self.rmt_freq

def set_rmt_freq(self, rmt_freq):
    self.rmt_freq = rmt_freq
    self.uhd_usrp_sink_0.set_center_freq(self.rmt_freq, 0)

def get_noise_volt(self):
    return self.noise_volt

def set_noise_volt(self, noise_volt):
    self.noise_volt = noise_volt
    self.channels_channel_model_0_0.set_noise_voltage(self.noise_volt)

def get_noise_taps(self):
    return self.noise_taps

def set_noise_taps(self, noise_taps):
    self.noise_taps = noise_taps
    self.channels_channel_model_0_0.set_taps(self.noise_taps)

def get_freq_offset(self):
    return self.freq_offset

def set_freq_offset(self, freq_offset):
    self.freq_offset = freq_offset
    self.channels_channel_model_0_0.set_frequency_offset(self.freq_offset)

```

```

def get_eb(self):
    return self.eb

def set_eb(self, eb):
    self.eb = eb

def get_bpsk(self):
    return self.bpsk

def set_bpsk(self, bpsk):
    self.bpsk = bpsk

def get_TxGain(self):
    return self.TxGain

def set_TxGain(self, TxGain):
    self.TxGain = TxGain

def get_RxGain(self):
    return self.RxGain

def set_RxGain(self, RxGain):
    self.RxGain = RxGain

def main(top_block_cls=Thesis_SS_BPSK_XMLRPC_Tuning_Server_Transceiver_Program, options=None):

    if StrictVersion("4.5.0") <= StrictVersion(Qt.qVersion()) < StrictVersion("5.0.0"):
        style = gr.prefs().get_string('qtgui', 'style', 'raster')
        Qt.QApplication.setGraphicsSystem(style)
    qapp = Qt.QApplication(sys.argv)

    tb = top_block_cls()

    tb.start()

    tb.show()

    def sig_handler(sig=None, frame=None):
        Qt.QApplication.quit()

    signal.signal(signal.SIGINT, sig_handler)
    signal.signal(signal.SIGTERM, sig_handler)

    timer = Qt.QTimer()
    timer.start(500)
    timer.timeout.connect(lambda: None)

    def quitting():
        tb.stop()
        tb.wait()

    qapp.aboutToQuit.connect(quitting)
    qapp.exec_()

if __name__ == '__main__':
    main()

```

#### D. XMLRPC external python client program 1

```
#!/usr/bin/env python3
#Written by Ramson
# -*- coding: utf-8 -*-
from xmlrpc.client import ServerProxy
import time
xmlrpc_control_client = ServerProxy('https://'+localhost+':8000') #Once
executed, client connects to server
#freq_steps = [400e6, 800e6, 1000e6, 1500e6, 2000e6]
freq_steps = [400.15e6, 460e6] # Array of reconfigurable frequencies
while True: #While in the loop performs the block below
    for freq in freq_steps: #Loop through the frequency array
        print("New Frequency set to:",freq/1000000,"MHz") # New frequency
        Frequency
        xmlrpc_control_client.set_rmt_freq(freq) # Frequency is set through the
        setter function
        time.sleep(1)
```



## E. XMLRPC client program 2

```
#!/usr/bin/env python2
# -*- coding: utf-8 -*-
#####
# GNU Radio Python Flow Graph
# Title: Client Program
# Generated: Tue Sep 19 04:57:40 2023
#####

from distutils.version import StrictVersion

if __name__ == '__main__':
    import ctypes
    import sys
    if sys.platform.startswith('linux'):
        try:
            x11 = ctypes.cdll.LoadLibrary('libX11.so')
            x11.XInitThreads()
        except:
            print "Warning: failed to XInitThreads()"

from PyQt5 import Qt, QtCore
from gnuradio import eng_notation
from gnuradio import gr
from gnuradio.eng_option import eng_option
from gnuradio.filter import firdes
from gnuradio.qtgui import Range, RangeWidget
from optparse import OptionParser
import sys
import xmlrpclib
from gnuradio import qtgui

class Client_Program(gr.top_block, Qt.QWidget):

    def __init__(self):
        gr.top_block.__init__(self, "Client Program")
        Qt.QWidget.__init__(self)
        self.setWindowTitle("Client Program")
        qtgui.util.check_set_qss()
        try:
            self.setWindowIcon(Qt.QIcon.fromTheme('gnuradio-grc'))
        except:
            pass
        self.top_scroll_layout = Qt.QVBoxLayout()
```

```

self.setLayout(self.top_scroll_layout)
self.top_scroll = Qt.QScrollArea()
self.top_scroll.setFrameStyle(Qt.QFrame.NoFrame)
self.top_scroll_layout.addWidget(self.top_scroll)
self.top_scroll.setWidgetResizable(True)
self.top_widget = Qt.QWidget()
self.top_scroll.setWidget(self.top_widget)
self.top_layout = Qt.QVBoxLayout(self.top_widget)
self.top_grid_layout = Qt.QGridLayout()
self.top_layout.addLayout(self.top_grid_layout)

self.settings = Qt.QSettings("GNU Radio", "Client_Program")

if StrictVersion(Qt.qVersion()) < StrictVersion("5.0.0"):
    self.restoreGeometry(self.settings.value("geometry").toByteArray())
else:
    self.restoreGeometry(self.settings.value("geometry", type=QtCore.QByteArray))

#####
# Variables
#####
self.variable_qtgui_range_0 = variable_qtgui_range_0 = 400150000

#####
# Blocks
#####
self.xmlrpc_client_0 = xmlrpclib.Server("http://localhost:8080")
self._variable_qtgui_range_0_range = Range(400150000, 460000000, 598500000, 400150000, 200)
self._variable_qtgui_range_0_win = RangeWidget(self._variable_qtgui_range_0_range, self.set_variable_qtgui_range_0,
"variable_qtgui_range_0", "counter_slider", float)
self.top_layout.addWidget(self._variable_qtgui_range_0_win)

def closeEvent(self, event):
    self.settings = Qt.QSettings("GNU Radio", "Client_Program")
    self.settings.setValue("geometry", self.saveGeometry())
    event.accept()

def get_variable_qtgui_range_0(self):
    return self.variable_qtgui_range_0

def set_variable_qtgui_range_0(self, variable_qtgui_range_0):
    self.variable_qtgui_range_0 = variable_qtgui_range_0

def main(top_block_cls=Client_Program, options=None):

```

```
if StrictVersion("4.5.0") <= StrictVersion(Qt.qVersion()) < StrictVersion("5.0.0"):
    style = gr.prefs().get_string('qtgui', 'style', 'raster')
    Qt.QApplication.setGraphicsSystem(style)
qapp = Qt.QApplication(sys.argv)

tb = top_block_cls()
tb.start()
tb.show()

def quitting():
    tb.stop()
    tb.wait()
qapp.aboutToQuit.connect(quitting)
qapp.exec_()

if __name__ == '__main__':
    main()
```

## F. SS-BPSK with TCP/IP server algorithm

```
#!/usr/bin/env python3
# -*- coding: utf-8 -*-

#
# SPDX-License-Identifier: GPL-3.0
#
# GNU Radio Python Flow Graph
# Title: Not titled yet
# Author: Ramsy
# GNU Radio version: v3.8.2.0-57-gd71cd177

from distutils.version import StrictVersion

if name == ' main ':
    import ctypes
    import sys

    if sys.platform.startswith('linux'):
        try:
            x11 = ctypes.cdll.LoadLibrary('libX11.so')
            x11.XInitThreads()
        except:
            print("Warning: failed to XInitThreads()")

    from PyQt5 import Qt
    from gnuradio import qtgui
    from gnuradio.filter import firdes
    import sip
    from gnuradio import analog
    from gnuradio import blocks
    from gnuradio import channels
    from gnuradio import digital
    from gnuradio import filter
    from gnuradio import gr
    import sys
    import signal
    from argparse import ArgumentParser
    from gnuradio.eng_arg import eng float, intx
    from gnuradio import eng notation
    from gnuradio import uhd
    import time
    from gnuradio.qtgui import Range, RangeWidget
    import programmed_server software # embedded python module

    from gnuradio import qtgui
```

```

class Thesis_SS_BPSK_TCP_IP_Tuning_Server_Transceiver_Program(gr.top_block, Qt.QWidget):

    def __init__(self):
        gr.top_block.__init__(self, "Not titled yet")
        Qt.QWidget.__init__(self)
        self.setWindowTitle("Not titled yet")
        qtgui.util.check_set_qss()
        try:
            self.setWindowIcon(Qt.QIcon.fromTheme('gnuradio-grc'))
        except:
            pass

        self.top_scroll_layout = Qt.QVBoxLayout()
        self.setLayout(self.top_scroll_layout)
        self.top_scroll = Qt.QScrollArea()
        self.top_scroll.setFrameStyle(Qt.QFrame.NoFrame)
        self.top_scroll_layout.addWidget(self.top_scroll)
        self.top_scroll.setWidgetResizable(True)
        self.top_widget = Qt.QWidget()
        self.top_scroll.setWidget(self.top_widget)
        self.top_layout = Qt.QVBoxLayout(self.top_widget)
        self.top_grid_layout = Qt.QGridLayout()
        self.top_layout.addLayout(self.top_grid_layout)

        self.settings = Qt.QSettings("GNU Radio", "Thesis SS BPSK TCP IP Tuning Server Transceiver Program")

        try:
            if StrictVersion(Qt.qVersion()) < StrictVersion("5.0.0"):
                self.restoreGeometry(self.settings.value("geometry").toByteArray())
            else:
                self.restoreGeometry(self.settings.value("geometry"))
        except:
            pass

        #####
        # Variables
        #####
        self.sps = sps = 16
        self.nfilts = nfilts = 32
        self.excess_bw = excess_bw = 0.350
        self.time_offset = time_offset = 1
        self.samp_rate = samp_rate = 1000000
        self.rrc_taps = rrc_taps = firdes.root_raised_cosine(nfilts, nfilts, 1.0/float(sps), excess_bw, 11*sps*nfilts)
        self.rmt_freq = rmt_freq = 460000000
        self.noise_volt = noise_volt = 0.0001

```

```

self.noise_taps = noise_taps = [[1.0, 0.25-0.25j, 0.5+0.10j, 0.3+0.2j]]
self.freq_offset = freq_offset = 0
self.eb = eb = 0.22
self.bpsk = bpsk = digital.constellation_bpsk().base()
self.TxGain = TxGain = 40
self.RxGain = RxGain = 65

#####
# Blocks
#####
self.time_offset_range = Range(0.999, 1.001, 0.000100, 1, 200)
self.time_offset_win = RangeWidget(self.time_offset_range, self.set_time_offset, 'Channel Timing Offset', "counter_slider", float)
self.top_grid_layout.addWidget(self.time_offset_win)
self.noise_volt_range = Range(0, 1, 0.01, 0.0001, 200)
self.noise_volt_win = RangeWidget(self.noise_volt_range, self.set_noise_volt, 'Channel Noise Voltage', "counter_slider", float)
self.top_grid_layout.addWidget(self.noise_volt_win)
self.freq_offset_range = Range(-0.100, 0.100, 0.001, 0, 200)
self.freq_offset_win = RangeWidget(self.freq_offset_range, self.set_freq_offset, 'Channel Freq offset', "counter_slider", float)
self.top_grid_layout.addWidget(self.freq_offset_win)
self.uhd_usrp_source_0 = uhd.usrp_source(
    ','.join((" ", "")),
    uhd.stream_args(
        cpu_format="fc32",
        args='',
        channels=list(range(0,1)),
    ),
)
self.uhd_usrp_source_0.set_center_freq(460e6, 0)
self.uhd_usrp_source_0.set_gain(65, 0)
self.uhd_usrp_source_0.set_antenna('RX2', 0)
self.uhd_usrp_source_0.set_bandwidth(1e6, 0)
self.uhd_usrp_source_0.set_samp_rate(samp_rate)
self.uhd_usrp_source_0.set_time_unknown_pps(uhd.time_spec())
self.uhd_usrp_sink_0 = uhd.usrp_sink(
    ','.join((" ", "")),
    uhd.stream_args(
        cpu_format="fc32",
        args='',
        channels=list(range(0,1)),
    ),
    '',
)
self.uhd_usrp_sink_0.set_center_freq(rwt_freq, 0)
self.uhd_usrp_sink_0.set_gain(40, 0)
self.uhd_usrp_sink_0.set_antenna('TX/RX', 0)

```

```

self.uhd_usrp_sink_0.set_bandwidth(1e6, 0)
self.uhd_usrp_sink_0.set_samp_rate(samp_rate)
self.uhd_usrp_sink_0.set_time_unknown_pps(uhd.time_spec())
self.qtgui_time_sink_x_0_0_1 = qtgui.time_sink_f(
    1024, #size
    samp_rate, #smp_rate
    "Signal Processing Time @ 460MHz", #name
    1 #number of inputs
)
self.qtgui_time_sink_x_0_0_1.set_update_time(0.10)
self.qtgui_time_sink_x_0_0_1.set_y_axis(-1, 1)

self.qtgui_time_sink_x_0_0_1.set_y_label('Amplitude', '')

self.qtgui_time_sink_x_0_0_1.enable_tags(False)
self.qtgui_time_sink_x_0_0_1.set_trigger_mode(qtgui.TRIG_MODE_FREE, qtgui.TRIG_SLOPE_POS, 0.0, 0, 0, '')
self.qtgui_time_sink_x_0_0_1.enable_autoscale(True)
self.qtgui_time_sink_x_0_0_1.enable_grid(True)
self.qtgui_time_sink_x_0_0_1.enable_axis_labels(True)
self.qtgui_time_sink_x_0_0_1.enable_control_panel(True)
self.qtgui_time_sink_x_0_0_1.enable_stem_plot(False)

labels = ['RxData', 'TxData', '', '', '',
          '', '', '', '', '']
widths = [1, 1, 1, 1, 1,
          1, 1, 1, 1, 1]
colors = ['blue', 'red', 'green', 'black', 'cyan',
          'magenta', 'yellow', 'dark red', 'dark green', 'dark blue']
alphas = [1.0, 1.0, 1.0, 1.0, 1.0,
          1.0, 1.0, 1.0, 1.0, 1.0]
styles = [1, 1, 1, 1, 1,
          1, 1, 1, 1, 1]
markers = [-1, -1, -1, -1, -1,
           -1, -1, -1, -1, -1]

for i in range(1):
    if len(labels[i]) == 0:
        self.qtgui_time_sink_x_0_0_1.set_line_label(i, "Data (%)"%.format(i))
    else:
        self.qtgui_time_sink_x_0_0_1.set_line_label(i, labels[i])
    self.qtgui_time_sink_x_0_0_1.set_line_width(i, widths[i])
    self.qtgui_time_sink_x_0_0_1.set_line_color(i, colors[i])
    self.qtgui_time_sink_x_0_0_1.set_line_style(i, styles[i])

```

```

self.qtgui_time_sink_x_0_0_1.set_line_marker(1, markers[1])
self.qtgui_time_sink_x_0_0_1.set_line_alpha(1, alphas[1])

self.qtgui_time_sink_x_0_0_1.win = sip.wrapinstance(self.qtgui_time_sink_x_0_0_1.pyqwidget(), Qt.QWidget)
self.top_grid_layout.addWidget(self.qtgui_time_sink_x_0_0_1.win)

self.qtgui_sink_x_0_1_0 = qtgui.sink_c(
    1024, #fftsize
    firdes.WIN_BLACKMAN_HARRIS, #wintype
    0, #fc
    samp_rate, #bw
    'PlotD', #name
    True, #plotfreq
    True, #plotwaterfall
    True, #plottime
    True #plotconst
)

self.qtgui_sink_x_0_1_0.set_update_time(1.0/10)
self._qtgui_sink_x_0_1_0.win = sip.wrapinstance(self.qtgui_sink_x_0_1_0.pyqwidget(), Qt.QWidget)

self.qtgui_sink_x_0_1_0.enable_rf_freq(False)

self.top_grid_layout.addWidget(self._qtgui_sink_x_0_1_0.win)

self.digital_pfb_clock_sync_xxx_0_0 = digital.pfb_clock_sync_ccf(sps, 62.8e-3, rrc_taps, 32, 16, 1.5, 1)
self.digital_costas_loop_cc_0 = digital.costas_loop_cc(0.0628, 2, False)
self.digital_constellation_modulator_0 = digital.generic_mod(
    constellation=bpsk,
    differential=False,
    samples_per_symbol=sps,
    pre_diff_code=True,
    excess_bw=excess_bw,
    verbose=False,
    log=False)

self.digital_constellation_decoder_cb_0 = digital.constellation_decoder_cb(bpsk)
self.dc_blocker_xx_0 = filter.dc_blocker_cc(1024, True)
self.channels_channel_model_0_0 = channels.channel_model(
    noise_voltage=noise_volt,
    frequency_offset=freq_offset,
    epsilon=time_offset,
    taps=noise_taps,
    noise_seed=0,
    block_tags=False)

self.blocks_wavfile_sink_0 = blocks.wavfile_sink('C:\\Users\\Ramsy\\Programs\\output.wav', 1, samp_rate, 8)

self.blocks_vector_source_x_0_0 = blocks.vector_source_b([(0x46, 0x46, 0x30, 0x34, 0x30, 0x38, 0x38, 0x30, 0x34, 0x30, 0x36, 0x30,
0x34, 0x32, 0x33, 0x31, 0x33, 0x30, 0x35, 0x30, 0x2F, 0x34, 0x31, 0x33, 0x33, 0x35, 0x33, 0x2E, 0x35, 0x31, 0x35, 0x31), True, 1, []])

self.blocks_unpack_k_bits_bb_0_0 = blocks.unpack_k_bits_bb(8)

```



```

self.blocks_file_sink_1 = blocks.file_sink(gr.sizeof char*1, 'C:\\Users\\Ramsy\\Programs\\loupot.bin', False)
self.blocks_file_sink_1.set_unbuffered(True)

self.blocks_file_sink_0_1 = blocks.file_sink(gr.sizeof char*1, 'C:\\Users\\Ramsy\\Programs\\loupot.bin', False)
self.blocks_file_sink_0_1.set_unbuffered(True)

self.blocks_char_to_float_0_0 = blocks.char_to_float(1, 1)

self.analog_agc_xx_0 = analog.agc_cc(1e-4, 1.0, 1.0)

self.analog_agc_xx_0.set_max_gain(65536)

self._TxGain_range = Range(10, 100, 1, 40, 200)

self._TxGain_win = RangeWidget(self._TxGain_range, self.set_TxGain, "TxGain", "counter_slider", float)

self.top_grid_layout.addWidget(self._TxGain_win)

self._RxGain_range = Range(10, 100, 1, 65, 200)

self._RxGain_win = RangeWidget(self._RxGain_range, self.set_RxGain, "RxGain", "counter_slider", float)

self.top_grid_layout.addWidget(self._RxGain_win)

#####

# Connections

#####

self.connect((self.analog_agc_xx_0, 0), (self.digital_pfb_clock_sync_xxx_0_0, 0))
self.connect((self.blocks_char_to_float_0_0, 0), (self.blocks_wavfile_sink_0, 0))
self.connect((self.blocks_char_to_float_0_0, 0), (self.qtgui_time_sink_x_0_0_1, 0))
self.connect((self.blocks_unpack_k_bits_bb_0_0, 0), (self.blocks_file_sink_0_1, 0))
self.connect((self.blocks_vector_source_x_0_0, 0), (self.blocks_unpack_k_bits_bb_0_0, 0))
self.connect((self.blocks_vector_source_x_0_0, 0), (self.digital_constellation_modulator_0, 0))
self.connect((self.channels_channel_model_0_0, 0), (self.uhd_usrp_sink_0, 0))
self.connect((self.dc_blocker_xx_0, 0), (self.analog_agc_xx_0, 0))
self.connect((self.digital_constellation_decoder_cb_0, 0), (self.blocks_char_to_float_0_0, 0))
self.connect((self.digital_constellation_decoder_cb_0, 0), (self.blocks_file_sink_1, 0))
self.connect((self.digital_constellation_modulator_0, 0), (self.channels_channel_model_0_0, 0))
self.connect((self.digital_costas_loop_cc_0, 0), (self.digital_constellation_decoder_cb_0, 0))
self.connect((self.digital_costas_loop_cc_0, 0), (self.qtgui_sink_x_0_1_0, 0))
self.connect((self.digital_pfb_clock_sync_xxx_0_0, 0), (self.digital_costas_loop_cc_0, 0))
self.connect((self.uhd_usrp_source_0, 0), (self.dc_blocker_xx_0, 0))

def closeEvent(self, event):
    self.settings = Qt.QSettings("GMU Radio", "Thesis SS BPSK TCP IP Tuning Server Transceiver Program")
    self.settings.setValue("geometry", self.saveGeometry())
    event.accept()

def get_sps(self):
    return self.sps

def set_sps(self, sps):

```

```

self.sps = sps
self.set_rrc_taps(firdes.root_raised_cosine(self.nfilts, self.nfilts, 1.0/float(self.sps), self.excess_bw, 11*self.sps*self.nfilts))

def get_nfilts(self):
    return self.nfilts

def set_nfilts(self, nfilts):
    self.nfilts = nfilts
    self.set_rrc_taps(firdes.root_raised_cosine(self.nfilts, self.nfilts, 1.0/float(self.sps), self.excess_bw, 11*self.sps*self.nfilts))

def get_excess_bw(self):
    return self.excess_bw

def set_excess_bw(self, excess_bw):
    self.excess_bw = excess_bw
    self.set_rrc_taps(firdes.root_raised_cosine(self.nfilts, self.nfilts, 1.0/float(self.sps), self.excess_bw, 11*self.sps*self.nfilts))

def get_time_offset(self):
    return self.time_offset

def set_time_offset(self, time_offset):
    self.time_offset = time_offset
    self.channels.channel_model_0_0.set_timing_offset(self.time_offset)

def get_samp_rate(self):
    return self.samp_rate

def set_samp_rate(self, samp_rate):
    self.samp_rate = samp_rate
    self.qtgui_sink_x_0_1_0.set_frequency_range(0, self.samp_rate)
    self.qtgui_time_sink_x_0_0_1.set_samp_rate(self.samp_rate)
    self.uhd_usrp_sink_0.set_samp_rate(self.samp_rate)
    self.uhd_usrp_source_0.set_samp_rate(self.samp_rate)

def get_rrc_taps(self):
    return self.rrc_taps

def set_rrc_taps(self, rrc_taps):
    self.rrc_taps = rrc_taps
    self.digital_pfb_clock_sync_xxx_0_0.update_taps(self.rrc_taps)

def get_rmt_freq(self):
    return self.rmt_freq

def set_rmt_freq(self, rmt_freq):

```

```

self.rmt_freq = rmt_freq
self.uhd_usrp_sink_0.set_center_freq(self.rmt_freq, 0)

def get_noise_volt(self):
    return self.noise_volt

def set_noise_volt(self, noise_volt):
    self.noise_volt = noise_volt
    self.channels_channel_model_0_0.set_noise_voltage(self.noise_volt)

def get_noise_taps(self):
    return self.noise_taps

def set_noise_taps(self, noise_taps):
    self.noise_taps = noise_taps
    self.channels_channel_model_0_0.set_taps(self.noise_taps)

def get_freq_offset(self):
    return self.freq_offset

def set_freq_offset(self, freq_offset):
    self.freq_offset = freq_offset
    self.channels_channel_model_0_0.set_frequency_offset(self.freq_offset)

def get_eb(self):
    return self.eb

def set_eb(self, eb):
    self.eb = eb

def get_bpsk(self):
    return self.bpsk

def set_bpsk(self, bpsk):
    self.bpsk = bpsk

def get_TxGain(self):
    return self.TxGain

def set_TxGain(self, TxGain):
    self.TxGain = TxGain

def get_RxGain(self):
    return self.RxGain

```

```

def set_RxGain(self, RxGain):
    self.RxGain = RxGain

def snipfcn_snippet_0(self):
    print("Starting Server")
    import threading
    threading.Thread(target=programed_server_software.tcpip_server,args=(self,)).start()

def snippets_main_after_init(tb):
    snipfcn_snippet_0(tb)

def main(top_block_cls=Thesis_SS_BPSK_TCP_IP_Tuning_Server_Transceiver_Program, options=None):

    if StrictVersion("4.5.0") <= StrictVersion(Qt.qVersion()) < StrictVersion("5.0.0"):
        style = gr_prefs().get_string('qtgui', 'style', 'raster')
        Qt.QApplication.setGraphicsSystem(style)
    qapp = Qt.QApplication(sys.argv)

    tb = top_block_cls()
    snippets_main_after_init(tb)
    tb.start()

    tb.show()

    def sig_handler(sig=None, frame=None):
        Qt.QApplication.quit()

    signal.signal(signal.SIGINT, sig_handler)
    signal.signal(signal.SIGTERM, sig_handler)

    timer = Qt.QTimer()
    timer.start(500)
    timer.timeout.connect(lambda: None)

    def quitting():
        tb.stop()
        tb.wait()

    qapp.aboutToQuit.connect(quitting)
    qapp.exec_()

if __name__ == '__main__':
    main()

```

## 1. Python snippet code\_gateway\_of\_client\_to server

Properties: Python Snippet

General Advanced Documentation

Section of Flowgraph Main - After Init

Priority

```
print("Starting Server")
import threading
threading.Thread(target=programed_server_software.tcpip_server,args=(self,)).start()
```

Code Snippet

## 2. Python module code\_server base

```
1 # Programmed by Ramson
2 import socket # create socket capability of python
3 import string
4 import sys
5
6 def tcpip_server(sdrmanip): #name of the server
7
8 while True:
9 sock=socket.socket(socket.AF_INET, socket.SOCK_STREAM) # create socket stream to ensure each peace of data or command is transferred from client to server
10 sock.setsockopt(socket.SOL_SOCKET, socket.SO_REUSEADDR, 1)
11 sock.bind(('127.0.0.1', 4242)) # The socket is created on a given port and local host
12
13 print("Waiting for Client Connection Request")
14 sock.listen(1) # Listen to any connection request
15 conn, addr=sock.accept() # Accept client Connection Request
16 with conn:
17 print('connected from', addr)
18
19 while True:
20 data=conn.recv(1) # Get each command from the client to the server
21
22 if data:
23 data=data.decode()
24 print(data)
25
26 if '*' in data:
27 sdrmanip.rmt_freq=sdrmanip.rmt_freq-59850000 #frequency decrement when receiving '*'
28 sdrmanip.set_RXFreq(sdrmanip.rmt_freq)
29 print("New Frequency(MHz) is Set: "+str((sdrmanip.rmt_freq)/1000000)+str(" MHz"))
30
31 if '+' in data:
32 sdrmanip.rmt_freq=sdrmanip.rmt_freq+59850000 #frequency increment when receiving '+'
33 sdrmanip.set_RXFreq(sdrmanip.rmt_freq)
34 print("New Frequency(MHz) is Set: "+str((sdrmanip.rmt_freq)/1000000)+str(" MHz"))
35
36 if 'q' in data: #quit program
37 print("Reconfiguration process was sucessful")
38 sock.shutdown(socket.SHUT_RDWR)
39 sock.close
40 break
```

## G. TCP/IP external python client program 1

```
#!/usr/bin/env python3
#Written by Ramson
# -*- coding: utf-8 -*-
from tcp_ip.client import ServerProxy
import time
tcp_ip_control_client = ServerProxy('https://'+localhost+':8000') #Once
executed, client connects to server
#freq_steps = [400e6, 800e6, 1000e6, 1500e6, 2000e6]
freq_steps = [400.15e6, 460e6] # Array of reconfigurable frequencies
while True: #While in the loop performs the block below
    for freq in freq_steps: #loop through the frequency array
        print("New Frequency set to:",freq/1000000,"MHz") # New frequency
        Frequency
        tcp_ip_control_client.set_rmt_freq(freq) # Frequency is set through the
        setter function
        time.sleep(1)
```

## H. TCP/IP telnet client program 2

```
import sys
import telnetlib

HOST = "127.0.0.1" # connect to host
PORT = "8000" #connecting port

telnetObj=telnetlib.Telnet(HOST,PORT) # Create telnet object
message = ("GET /index.html HTTPS/1.1\nHost:"+HOST+"\n\n").encode('ascii') # Get all ASCII character
commands
telnetObj.write(message) # Receive command/ASCII character or message
output=telnetObj.read_all() # Telnet object get the command, and sent to server
print(output) # When successful acknowledgement is received
telnetObj.close() # Job done
```

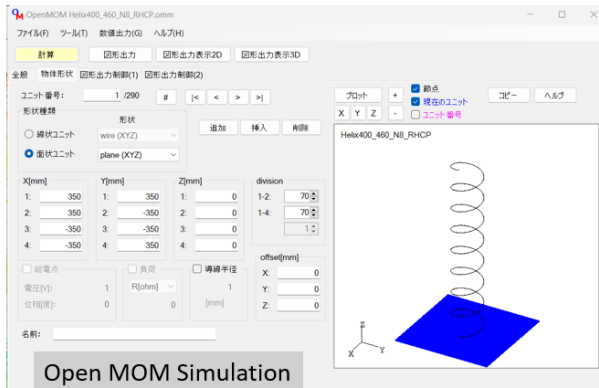
# I. Antenna Simulation Procedure

## Create Helix Parameters & Run Python Program: Anaconda Execution

```
(base) C:\Users\Ramsy\Downloads\20230929_Helix_Generator_Ramson (2)\20230929_Helix_Generator_Ramson>python .\HelixGenerator.py
py \DHF_Helix.csv
['Helix400_460_NS_RHCP' '4.00E+08' '4.60E+08' '3' '0' '0' '0' '0' '0'
'0.22' '0.16' '8' '0.7' '0' '0.005' '0' '0' '36' '70']
['Helix400_460_NS_LHCP' '4.00E+08' '4.60E+08' '3' '0' '0' '0' '0' '0'
'0.22' '0.16' '-8' '0.7' '0' '0.005' '0' '0' '36' '70']
(base) C:\Users\Ramsy\Downloads\20230929_Helix_Generator_Ramson (2)\20230929_Helix_Generator_Ramson>
```

## Feed Parameters in Open MOM and Execute

```
C:\Users\Ramsy\Downloads\2 x +
No. of feeds = 1
No. of loads = 0
No. of open ends = 1
Ground = NO
Plane wave = NO
Memory size [MB] = 419
No. of frequencies = 4
( 1/4).....
( 2/4).....
( 3/4).....
( 4/4).....
=== input impedance (Z0=150.0[ohm]) ===
feeds = 1
frequency[Hz] Rin[ohm] Xin[ohm] Gin[mS] Bin[mS] Ref[dB] VSWR
4.00000e+08 352.114 -178.781 2.258 1.146 -5.912 3.051
4.20000e+08 321.981 -64.834 2.985 0.601 -8.273 2.256
4.40000e+08 348.873 -174.716 2.295 1.152 -6.814 3.003
4.60000e+08 298.762 -161.440 2.591 1.400 -6.739 2.786
=== output files ===
omn.log, geom3d.htm, omm.out
=== normal end ===
Thu Oct 5 16:13:01 2023
=== cpu time [sec] ===
part-1 : 1.187
part-2 : 5.609
part-3 : 60.455
part-4 : 0.098
total : 76.229
```



Open MOM Simulation

## J. Antenna Simulation Python Program for Helix

C:\> Users > Ramsy > Downloads > 20230929\_Helix\_Generator\_Ramson (2) > 20230929\_Helix\_Generator\_Ramson > helixGenerator.py > ...

```
1 # read parameter.csv and generate Dish antenna model file for Open MOM
2
3 import csv
4 import sys
5 import numpy as np
6
7 import os
8
9 from helix import helixGen
10
11 if(len(sys.argv) <= 1):
12     print("please set parameter file path (*.csv)")
13     exit()
14
15 csvPath = sys.argv[1]
16
17 with open(csvPath) as f:
18     parameterList = np.loadtxt(f,delimiter = ",", dtype = str, skiprows=1)
19     for parameter in parameterList:
20
21
22         modelName = parameter[0]
23         if(modelName == ""):
24             continue
25         os.mkdir("./" + modelName)
26
27         print(parameter)
28
29         with open(modelName + "/" + modelName + ".omm", mode="w") as modelFile:
30
31
32             frequency1 = float(parameter[ 1])
33             frequency2 = float(parameter[ 2])
34             freqDiv = int(parameter[ 3])
35             paraDire = float(parameter[ 4])
36             focal = float(parameter[ 5])
37             paraOffset = float(parameter[ 6])
38             feedAngle = float(parameter[ 7]) / 180 * np.pi
39             feedOffset = float(parameter[ 8])
40             heliDire = float(parameter[ 9])
41             heliPitch = float(parameter[10])
42             heliNum = float(parameter[11])
43             heliGndSize = float(parameter[12])
44             heliInitPha = float(parameter[13]) / 180 * np.pi
45             feedLen = float(parameter[14])
46             paraAngDiv = int(parameter[15])
47             paraRadDiv = int(parameter[16])
48             heliAngDiv = int(parameter[17])
```



```

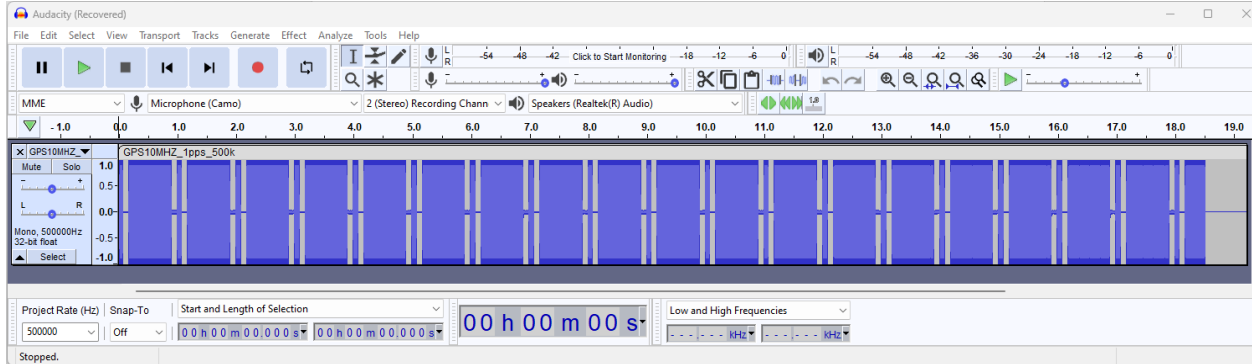
49     heliGndDiv = int(parameter[18])
50
51
52     modelText = ""
53
54     #header and title
55     modelText += "OpenMOM 1.7\n" #for OpenMOM1.7 or greater
56     modelText += "title = " + modelName + "\n"
57
58     heliDirection = 1
59
60     if(heliNum < 0):
61         heliNum = -heliNum
62         heliDirection = -1
63
64     modelText += helixGen(heliDirection, heliDire, heliPitch, heliNum, heliGndSize, heliInitPha, feedOffset, feedLen, -feedAngle, heliAngDiv, heliGndDiv)
65 #     modelText += paraSurGen(paraDire, focal, paraOffset, paraAngDiv, paraRadDiv)
66
67     #footer
68     modelText += "frequency = " + "{0:3e}".format(frequency1) + " " + "{0:3e}".format(frequency2) + " " + "{0:d}".format(freqDiv) + "\n"
69     modelText += "z0 = 150\n"
70     modelText += "radiusall = 2 0.2\n"
71     modelText += "geom3dnode = 0.05 1 0\n"
72     modelText += "plotcurrent = 0 1\n"
73     modelText += "plotfrequency = 1 1 0 1\n"
74     modelText += "plotfar1d = X 72\n"
75     modelText += "plotfar1d = Y 72\n"
76     modelText += "far1dstyle = 0\n"
77     modelText += "far1dcomponent = 0 0 1\n"
78     modelText += "far1ddb = 1\n"
79     modelText += "plotfar2d = 18 36\n"
80     modelText += "far2dcomponent = 1 0 0 0 0 0\n"
81     modelText += "far2ddb = 1\n"
82     modelText += "window2d = 750 500 15 0\n"
83     modelText += "window3d = 600 600 12 60 30\n"
84     modelText += "end\n"
85
86     modelFile.write(modelText)
87     modelFile.close()
88

```

## K. Other software

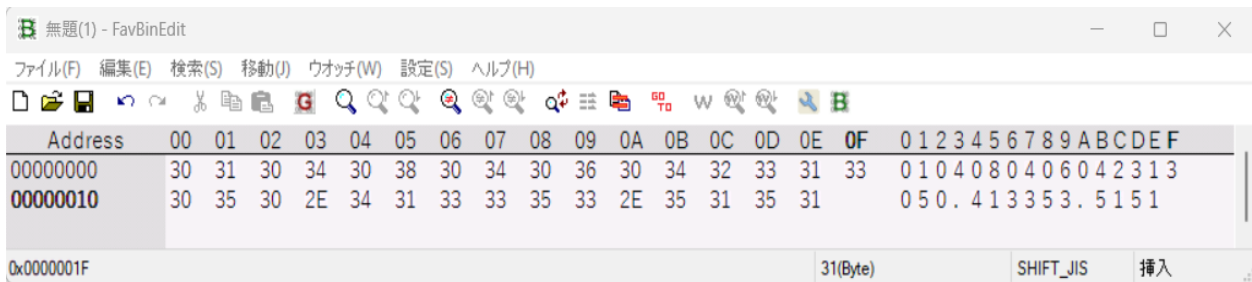
### I. Audacity

Software to analyze wave files



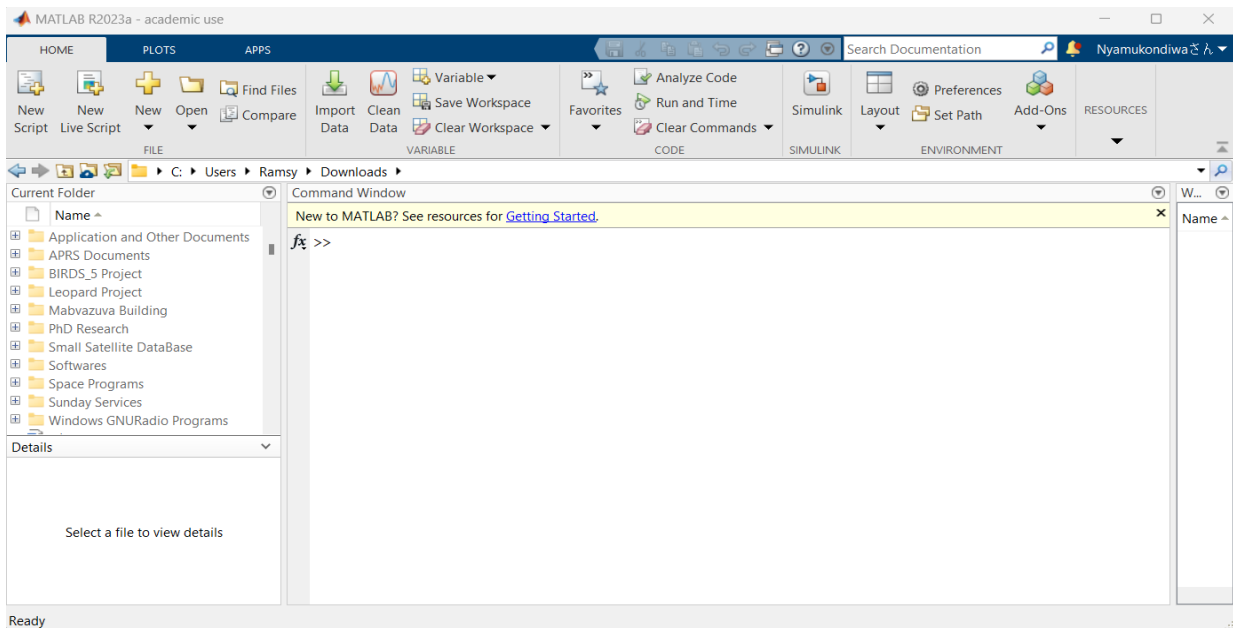
### II. FavBin Edit

Software to open binary or hex files and analyze the data



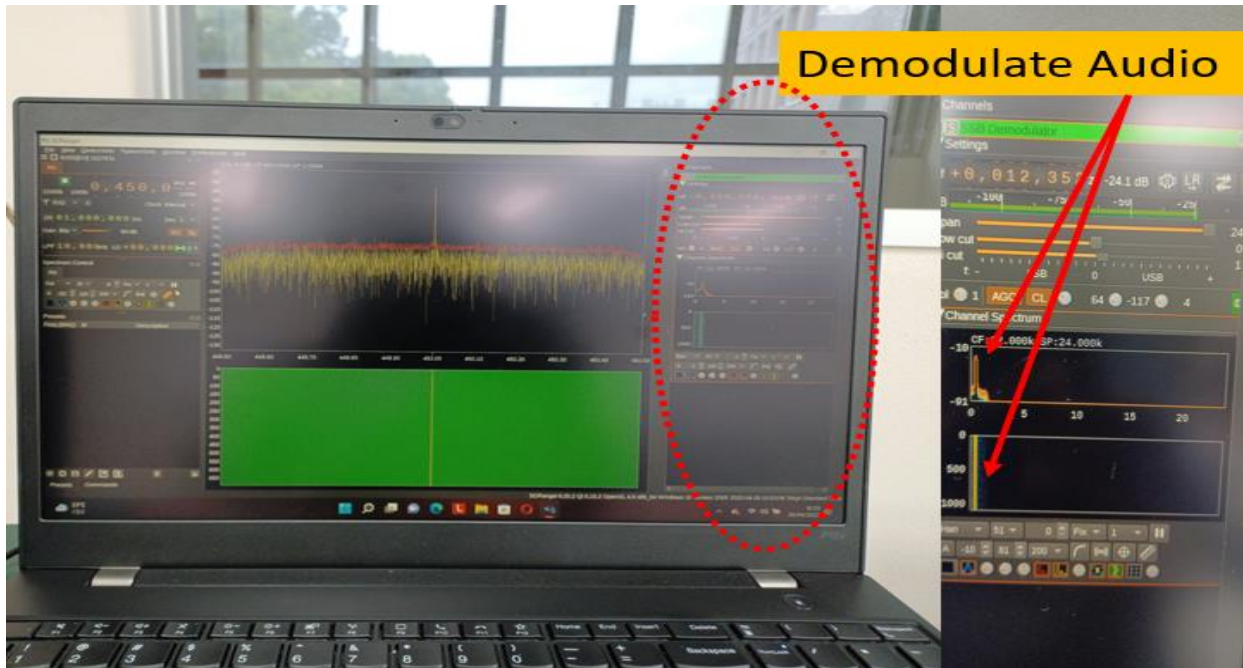
### III. MATLAB programs

MATLAB used to program and simulate some codes for testing and verification.



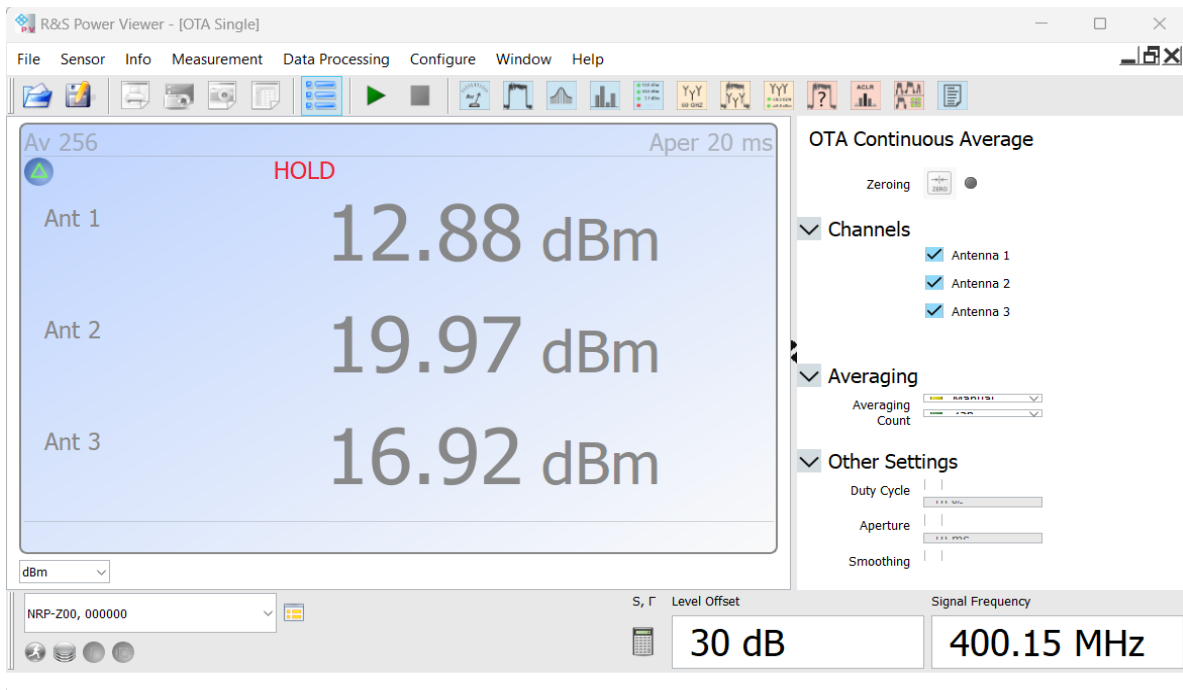
#### IV. SDRAngel/ SDR Sharp

Software to support RF testing with SDR



#### V. Power Viewer

Software to measure SDR output power



## References

- [1] R.M. Nyamukondiwa, N.C. Orger, D. Nakayama, M. Cho, A Study on the Derivation of Atmospheric Water Vapor Based on Dual Frequency Radio Signals and Intersatellite Communication Networks, *Aerospace*. 10 (2023) 807. <https://doi.org/10.3390/aerospace10090807>.
- [2] Q. Zhou, H. Liu, S. Zhang, X. Deng, Sensitivity analyses of precipitable water vapor retrieval from the ground-based infrared measurements in clear sky conditions, *J Appl Remote Sens.* 13 (2019) 1. <https://doi.org/10.1117/1.jrs.13.044513>.
- [3] W. Junkermann, J. Hacker, Unprecedented levels of ultrafine particles, major sources, and the hydrological cycle, *Sci Rep.* 12 (2022). <https://doi.org/10.1038/s41598-022-11500-5>.
- [4] UCAR, The Water Cycle and Climate Change | Center for Science Education, (2023). <https://scied.ucar.edu/learning-zone/climate-change-impacts/water-cycle-climate-change> (accessed April 3, 2023).
- [5] European Commission, Consequences of climate change, [https://Climate.Ec.Europa.Eu/Climate-Change/Consequences-Climate-Change\\_en](https://Climate.Ec.Europa.Eu/Climate-Change/Consequences-Climate-Change_en). (n.d.). [https://climate.ec.europa.eu/climate-change/consequences-climate-change\\_en](https://climate.ec.europa.eu/climate-change/consequences-climate-change_en) (accessed July 15, 2023).
- [6] Climate Change - United Nations Sustainable Development, (n.d.). [https://www.un.org/sustainabledevelopment/climate-change/?fbclid=IwAR1nC2m2YioXkEvzdXQRa\\_AL5hPkL-chZe2QIVRNQz4TOHwPEsRGLHwCMkg](https://www.un.org/sustainabledevelopment/climate-change/?fbclid=IwAR1nC2m2YioXkEvzdXQRa_AL5hPkL-chZe2QIVRNQz4TOHwPEsRGLHwCMkg). (accessed April 3, 2023).
- [7] Michael Case, Climate Change Impacts on East Africa, n.d.
- [8] 1267\_Atlas\_of\_Mortality\_en\_2, (n.d.).
- [9] M.D. Lebsock, K. Suzuki, L.F. Millán, P.M. Kalmus, The feasibility of water vapor sounding of the cloudy boundary layer using a differential absorption radar technique, *Atmos Meas Tech.* 8 (2015) 3631–3645. <https://doi.org/10.5194/amt-8-3631-2015>.
- [10] K.M. Firsov, T.Y. Chesnokova, E. V. Bobrov, I.I. Klitochenko, Total water vapor content retrieval from sun photometer data, *Atmospheric and Oceanic Optics.* 26 (2013) 281–284. <https://doi.org/10.1134/S1024856013040040>.
- [11] S. Manandhar, Y.H. Lee, Y.S. Meng, J.T. Ong, A Simplified Model for the Retrieval of Precipitable Water Vapor from GPS Signal, *IEEE Transactions on Geoscience and Remote*

- Sensing. 55 (2017) 6245–6253. <https://doi.org/10.1109/TGRS.2017.2723625>.
- [12] NOAA Physical Science Laboratory, Surface Meteorology, <https://psl.noaa.gov/data/obs/instruments/surfacemetdescription.html>. (n.d.).
- [13] I. Mattis, A. Ansmann, D. Althausen, V. Jaenisch, U. Wandinger, Y.F. Arshinov, S.M. Bobrovnikov, I.B. Serikov, Relative-humidity profiling in the troposphere with a Raman lidar, 2002.
- [14] E. Musico, C. Cesaroni, L. Spogli, J.P. Merryman Boncori, G. De Franceschi, R. Seu, The Total Electron Content from InSAR and GNSS: A Midlatitude Study, *IEEE J Sel Top Appl Earth Obs Remote Sens.* 11 (2018) 1725–1733. <https://doi.org/10.1109/JSTARS.2018.2812305>.
- [15] R.N. Halthore, T.F. Eck, B.N. Holben, B.L. Markham, Sun photometric measurements of atmospheric water vapor column abundance in the 940-nm band, *Journal of Geophysical Research Atmospheres.* 102 (1997) 4343–4352. <https://doi.org/10.1029/96jd03247>.
- [16] von Marion Elsa Amelie Heublein aus Nürnberg, D.-I. habil Stefan Hinz, Xiaoxiang Zhu *Signal Processing in Earth Observation Remote Sensing Technology Institute German Aerospace*, 2019.
- [17] Boehm Johannes, Boehm Johannes - 2004 - Troposphärische Laufzeitverzögerungen in der VLBI, (n.d.).
- [18] M.A. Aleshina, V.A. Semenov, A. V. Chernokulsky, A link between surface air temperature and extreme precipitation over Russia from station and reanalysis data, *Environmental Research Letters.* 16 (2021). <https://doi.org/10.1088/1748-9326/ac1cba>.
- [19] H. Liu, S. Tang, S. Zhang, J. Hu, Evaluation of MODIS water vapour products over China using radiosonde data, *Int J Remote Sens.* 36 (2015) 680–690. <https://doi.org/10.1080/01431161.2014.999884>.
- [20] T. Jingshu, C. Biyan, W. Wei, Y. Wenkun, D. Wujiao, Evaluating Precipitable Water Vapor Products from Fengyun-4A Meteorological Satellite Using Radiosonde, GNSS, and ERA5 Data, *IEEE Transactions on Geoscience and Remote Sensing.* 60 (2022). <https://doi.org/10.1109/TGRS.2022.3146018>.
- [21] F. Alshawaf, T. Fuhrmann, A. Knöpfler, X. Luo, M. Mayer, S. Hinz, B. Heck, Accurate Estimation of Atmospheric Water Vapor Using GNSS Observations and Surface Meteorological Data, *IEEE Transactions on Geoscience and Remote Sensing.* 53 (2015)

- 3764–3771. <https://doi.org/10.1109/TGRS.2014.2382713>.
- [22] Y. Yao, Q. Zhao, Maximally Using GPS Observation for Water Vapor Tomography, *IEEE Transactions on Geoscience and Remote Sensing*. 54 (2016) 7185–7196. <https://doi.org/10.1109/TGRS.2016.2597241>.
- [23] P. Campos-Arias, G. Esquivel-Hernández, J.F. Valverde-Calderón, S. Rodríguez-Rosales, J. Moya-Zamora, R. Sánchez-Murillo, J. Boll, GPS precipitable water vapor estimations over Costa Rica: A comparison against atmospheric sounding and moderate resolution imaging spectrometer (MODIS), *Climate*. 7 (2019). <https://doi.org/10.3390/cli7050063>.
- [24] K. Aheieva, R. Rahmatillah, R. Ninagawa, I. Owulatobi Adebolu, S. Kim, Y. Kakimoto, T. Yamauchi, H. Masui, M. Cho, C. Chee Lap, Z. Ying, T. Man Siu, L. King Ho Holden, Project Overview of SPATIUM-I: A Technology Demonstration Mission Toward Global Three-Dimensional Ionosphere Mapping via CubeSat Constellation Equipped with an Atomic Clock, 2021. [www.jossonline.com](http://www.jossonline.com).
- [25] C.K. Carbajal Henken, H. Diedrich, R. Preusker, J. Fischer, MERIS full-resolution total column water vapor: Observing horizontal convective rolls, *Geophys Res Lett*. 42 (2015) 10074–10081. <https://doi.org/10.1002/2015GL066650>.
- [26] S. Varamesh, S.M. Hosseini, M. Rahimzadegan, Estimation of Atmospheric Water Vapor Using MODIS Data 1. (Case Study: Golestan Ptovince of Iran), *Journal of Materials and Environmental Sciences* ISSN: 2028-2508. 8 (20017) 1690–1695. <http://www.jmaterenvironsci.com/> (accessed August 2, 2023).
- [27] H. Diedrich, F. Wittchen, R. Preusker, J. Fischer, Representativeness of total column water vapour retrievals from instruments on polar orbiting satellites, *Atmos Chem Phys*. 16 (2016) 8331–8339. <https://doi.org/10.5194/acp-16-8331-2016>.
- [28] S. Haji-Aghajany, Y. Amerian, A. Amiri-Simkooei, Impact of Climate Change Parameters on Groundwater Level: Implications for Two Subsidence Regions in Iran Using Geodetic Observations and Artificial Neural Networks (ANN), *Remote Sens (Basel)*. 15 (2023). <https://doi.org/10.3390/rs15061555>.
- [29] S. Haji-Aghajany, Y. Amerian, A. Amiri-Simkooei, Function-Based Troposphere Tomography Technique for Optimal Downscaling of Precipitation, *Remote Sens (Basel)*. 14 (2022). <https://doi.org/10.3390/rs14112548>.
- [30] H. Wazneh, M.A. Arain, P. Coulibaly, P. Gachon, Evaluating the Dependence between

- Temperature and Precipitation to Better Estimate the Risks of Concurrent Extreme Weather Events, *Advances in Meteorology*. 2020 (2020). <https://doi.org/10.1155/2020/8763631>.
- [31] M.S. Wong, X. Jin, Z. Liu, J.E. Nichol, S. Ye, P. Jiang, P.W. Chan, Geostationary satellite observation of precipitable water vapor using an Empirical Orthogonal Function (EOF) based reconstruction technique over eastern China, *Remote Sens (Basel)*. 7 (2015) 5879–5900. <https://doi.org/10.3390/rs70505879>.
- [32] E. Peral, S. Tanelli, Z. Haddad, O. Sy, G. Stephens, E. Im, Raincube: A proposed constellation of precipitation profiling radars in CubeSat, in: 2015 IEEE International Geoscience and Remote Sensing Symposium (IGARSS), IEEE, 2015: pp. 1261–1264. <https://doi.org/10.1109/IGARSS.2015.7326003>.
- [33] N. Cihan ORGER, KITSUNE Satellite Bus System Overview, 2022. [https://birds-project.com/open-source/pdf/20221012\\_BIRDS\\_BUS\\_Open-Source\\_Webinar\\_KITSUNE\\_overview.pdf](https://birds-project.com/open-source/pdf/20221012_BIRDS_BUS_Open-Source_Webinar_KITSUNE_overview.pdf) (accessed July 22, 2023).
- [34] C. Lap Chow, Y. Zhang, M. Siu Tse, K. Ho Holden Li, K. Aheieva, R. Rahmatillah, R. Ninagawa, I. Owulatobi Adebolu, S. Kim, Y. Kakimoto, T. Yamauchi, H. Masui, M. Cho, Overview of Project SPATIUM-Space Precision Atomic-clock Timing Utility Mission, 2019.
- [35] G-Nut Software s.r.o., GNSS and troposphere, <https://Gnutsoftware.Com/Gnss-and-Troposphere>. (n.d.). <https://gnutsoftware.com/gnss-and-troposphere> (accessed July 23, 2023).
- [36] K.-N. Wang, C.O. Ao, M.G. Morris, G.A. Hajj, M.J. Kurowski, F.J. Turk, A.W. Moore, Joint 1DVar Retrievals of Tropospheric Temperature and Water Vapor from GNSS-RO and Microwave Radiometer Observations, *EGUsphere Preprint Repository*, California, USA. (2023) 1–25. <https://doi.org/10.5194/egusphere-2023-85>.
- [37] X. Calbet, C. Carbajal Henken, S. Desouza-Machado, B. Sun, T. Reale, L. Prieto, Small scale variability of water vapor in the atmosphere: implications for inter-comparison of data from different measuring systems, (n.d.) 1–3. <https://doi.org/10.5194/amt-2022-111>.
- [38] K. Lonitz, GNSS radio occultation (GNSS-RO): Lecture 1-Principles and NWP use ECMWF/EUMETSAT Satellite training course, 2023. <http://www.romsaf.org>.
- [39] Hoda Awany, UHF SIGNAL ANALYSIS FOR IONOSPHERE TOTAL ELECTRON CONTENT ESTIMATION, 2020.

- [40] R. Rahmatillah, K. Aheieva, M. Cho, L.K.H. Holden, Ionosphere irregularity observation using reference signals from CubeSat constellation, 2018. <https://www.scopus.com/inward/record.uri?eid=2-s2.0-85065331067&partnerID=40&md5=01ff82c545c3122c9796c939e42e539>.
- [41] G. Elgered, T. Ning, J. Wang, G. Elgered, G. Dick, J. Wickert, M. Bradke, M. Sommer, The uncertainty of the atmospheric integrated water vapour estimated from GNSS observations, *Atmos. Meas. Tech. Discuss.* 8 (2015) 8817–8857. <https://doi.org/10.5194/amtd-8-8817-2015>.
- [42] Holly Shaftel, Susan Callery, Randal Jackson, Daniel Bailey, Susan Callery, Earth's Atmosphere: A Multi-layered Cake, <https://Climate.Nasa.Gov/News/2919/Earths-Atmosphere-a-Multi-Layered-Cake/>. (2019). <https://climate.nasa.gov/news/2919/earths-atmosphere-a-multi-layered-cake/> (accessed July 24, 2023).
- [43] Joseph Mitola, Preston Marshall, Kwang-cheng Chen, Markus Mueck, Zoran Zvonar, Software defined radio - 20 years later: part 2 [Guest Editorial], *IEEE*. 54 (2016).
- [44] Advantages of BPSK | Disadvantages of BPSK, (n.d.). <https://www.rfwireless-world.com/Terminology/Advantages-and-Disadvantages-of-BPSK.html> (accessed April 3, 2023).
- [45] A. Daniel Ogundele, AAS 22-646 MODELING AND ANALYSIS OF SPACECRAFT FORMATION FLYING UNDER THE EFFECTS OF J2, DRAG AND LIFT PERTURBATION FORCES, 2022. <https://www.researchgate.net/publication/363261611>.
- [46] O. Hoda, A. El, Ionosphere Measurement: On-Board Pseudo-range Measurement using UHF Ground station-Cube-Sat Uplink, Chee Lap Chow, 2019.
- [47] Wojciech Gomolka, The concept of Sockets and basic Function Blocks for communication over Ethernet Part 2 TCP Server and TCP Client, 2014. <https://www.researchgate.net/publication/264081315>.
- [48] XML-RPC | Common APIs Handbook | WordPress Developer Resources, (n.d.). <https://developer.wordpress.org/apis/xml-rpc/> (accessed April 3, 2023).
- [49] Q. Zhu, H. Tao, Y. Cao, X. Li, Laser Inter-Satellite Link Visibility and Topology Optimization for Mega Constellation, *Electronics (Switzerland)*. 11 (2022). <https://doi.org/10.3390/electronics11142232>.
- [50] The COMET, Introduction to Tropical Meteorology, 2nd Edition,



- [https://www.chanthaburi.buu.ac.th/~wirote/met/tropical/textbook\\_2nd\\_edition/navmenu.php\\_tab\\_2\\_page\\_5.3.0.htm](https://www.chanthaburi.buu.ac.th/~wirote/met/tropical/textbook_2nd_edition/navmenu.php_tab_2_page_5.3.0.htm), 2013.
- [https://www.chanthaburi.buu.ac.th/~wirote/met/tropical/textbook\\_2nd\\_edition/navmenu.php\\_tab\\_2\\_page\\_5.3.0.htm](https://www.chanthaburi.buu.ac.th/~wirote/met/tropical/textbook_2nd_edition/navmenu.php_tab_2_page_5.3.0.htm) (accessed July 15, 2023).
- [51] C. Borger, S. Beirle, T. Wagner, A 16-year global climate data record of total column water vapour generated from OMI observations in the visible blue spectral range, *Earth Syst Sci Data*. 15 (2023) 3023–3049. <https://doi.org/10.5194/essd-15-3023-2023>.
- [52] NOAA, TEACHER BACKGROUND: UNDERSTANDING FEEDBACK LOOPS, n.d. [https://gml.noaa.gov/outreach/info\\_activities/pdfs/TBI\\_understanding\\_feedback\\_loops.pdf](https://gml.noaa.gov/outreach/info_activities/pdfs/TBI_understanding_feedback_loops.pdf) (accessed July 15, 2023).
- [53] BioNinja, Greenhouse Gases, <https://ib.bioninja.com.au/standard-level/topic-4-ecology/44-climate-change/greenhouse-gases.html>. (n.d.). <https://ib.bioninja.com.au/standard-level/topic-4-ecology/44-climate-change/greenhouse-gases.html> (accessed July 15, 2023).
- [54] L. Facheris, A. Antonini, F. Argenti, F. Barbara, U. Cortesi, F. Cuccoli, S. Del Bianco, F. Dogo, A. Feta, M. Gai, A. Gregorio, G. Macelloni, A. Mazzinghi, S. Melani, F. Montomoli, A. Ortolani, L. Rovai, L. Severin, T. Scopa, Towards Space Deployment of the NDSA Concept for Tropospheric Water Vapour Measurements, *Atmosphere (Basel)*. 14 (2023). <https://doi.org/10.3390/atmos14030550>.
- [55] Luca Facheris, Fabrizio Cuccoli, Global ECMWF Analysis Data for Estimating the Water Vapor Content Between Two LEO Satellites Through NDSA Measurements, *IEEE Transactions on Geoscience and Remote Sensing*. 56 (2018).
- [56] F. Cuccoli, L. Facheris, Normalized Differential Spectral Attenuation (NDSA): A novel approach to estimate atmospheric water vapor along a LEO-LEO satellite link in the Ku/K bands, *IEEE Transactions on Geoscience and Remote Sensing*. 44 (2006) 1493–1502. <https://doi.org/10.1109/TGRS.2006.870438>.
- [57] B. Fersch, A. Wagner, B. Kamm, E. Shehaj, A. Schenk, P. Yuan, A. Geiger, G. Moeller, B. Heck, S. Hinz, H. Kutterer, H. Kunstmann, Tropospheric water vapor: A comprehensive high resolution data collection for the transnational Upper Rhine Graben region, n.d.
- [58] M. Zhu, Z. Liu, W. Hu, Observing Water Vapor Variability During Three Super Typhoon Events in Hong Kong Based on GPS Water Vapor Tomographic Modeling Technique,

- Journal of Geophysical Research: Atmospheres. 125 (2020).  
<https://doi.org/10.1029/2019JD032318>.
- [59] P. Withers, L. Moore, How to Process Radio Occultation Data: 2. From Time Series of Two-Way, Single-Frequency Frequency Residuals to Vertical Profiles of Ionospheric Properties, *Radio Sci.* 55 (2020). <https://doi.org/10.1029/2019RS007046>.
- [60] M. Bevis, S. Businger, T.A. Herring, C. Rocken, R.A. Anthes, R.H. Ware, GPS meteorology: remote sensing of atmospheric water vapor using the global positioning system, *J Geophys Res.* 97 (1992). <https://doi.org/10.1029/92jd01517>.
- [61] G.G.J.D.G.D.S. de H.E.P.O.B.R.P.R. van M. Jonathan Jones, *Advanced GNSS Tropospheric Products for Monitoring Severe Weather Events and Climate*, 2020.
- [62] C.T. Nguyen, S.T. Oluwadare, N.T. Le, M. Alizadeh, J. Wickert, H. Schuh, Spatial and temporal distributions of ionospheric irregularities derived from regional and global roti maps, *Remote Sens (Basel)*. 14 (2022). <https://doi.org/10.3390/rs14010010>.
- [63] B. Chen, Z. Liu, W.K. Wong, W.C. Woo, Detecting water vapor variability during heavy precipitation events in Hong Kong using the GPS tomographic technique, *J Atmos Ocean Technol.* 34 (2017) 1001–1019. <https://doi.org/10.1175/JTECH-D-16-0115.1>.
- [64] K. Wilgan, F. Hurter, A. Geiger, W. Rohm, J. Bosy, Tropospheric refractivity and zenith path delays from least-squares collocation of meteorological and GNSS data, *J Geod.* 91 (2017) 117–134. <https://doi.org/10.1007/s00190-016-0942-5>.
- [65] P. Meunram, C. Satirapod, Spatial variation of precipitable water vapor derived from GNSS CORS in Thailand, *Geod Geodyn.* 10 (2019) 140–145. <https://doi.org/10.1016/j.geog.2019.01.003>.
- [66] P. Meunram, C. Satirapod, Spatial variation of precipitable water vapor derived from GNSS CORS in Thailand, *Geod Geodyn.* 10 (2019) 140–145. <https://doi.org/10.1016/j.geog.2019.01.003>.
- [67] Z. Dong, S. Jin, 3-D water vapor tomography in Wuhan from GPS, BDS and GLONASS observations, *Remote Sens (Basel)*. 10 (2018). <https://doi.org/10.3390/rs10010062>.
- [68] P. Yuan, A. Hunegnaw, F. Alshawaf, J. Awange, A. Klos, F.N. Teferle, H. Kutterer, Feasibility of ERA5 integrated water vapor trends for climate change analysis in continental Europe: An evaluation with GPS (1994–2019) by considering statistical significance, *Remote Sens Environ.* 260 (2021). <https://doi.org/10.1016/j.rse.2021.112416>.

- [69] J.R. Eyre, An introduction to GPS radio occultation and its use in numerical weather prediction, n.d.
- [70] T. Sievert, GNSS RADIO OCCULTATION INVERSION METHODS AND REFLECTION OBSERVATIONS IN THE LOWER TROPOSPHERE, n.d.
- [71] T.S.M.S.L.S.M.S. J. Wickert, GNSS radio Occultation, <https://Ggos.Org/Item/Gnss-Radio-Occultation/#learn-This>. (2023).
- [72] C.L. Liu, G. Kirchengast, S. Syndergaard, E.R. Kursinski, Y.Q. Sun, W.H. Bai, Q.F. Du, A review of low Earth orbit occultation using microwave and infrared-laser signals for monitoring the atmosphere and climate, *Advances in Space Research*. 60 (2017) 2776–2811. <https://doi.org/10.1016/j.asr.2017.05.011>.
- [73] NASA, Moderate Resolution Imaging Spectroradiometer, NASA Website. (n.d.). <https://terra.nasa.gov/about/terra-instruments/modis#:~:text=MODIS%20helps%20scientists%20determine%20the,to%20understanding%20Earth's%20climate%20system>. (accessed July 23, 2023).
- [74] K. Wilgan, M.A. Siddique, T. Strozzi, A. Geiger, O. Frey, Comparison of tropospheric path delay estimates from GNSS and space-borne SAR interferometry in alpine conditions, *Remote Sens (Basel)*. 11 (2019). <https://doi.org/10.3390/rs11151789>.
- [75] Z. Li, Y. Cao, J. Wei, M. Duan, L. Wu, J. Hou, J. Zhu, Time-series InSAR ground deformation monitoring: Atmospheric delay modeling and estimating, *Earth Sci Rev*. 192 (2019) 258–284. <https://doi.org/10.1016/j.earscirev.2019.03.008>.
- [76] R. Azeriansyah, . H., Integration PS-InSAR and MODIS PWV Data to Monitor Land Subsidence in Semarang City 2015–2018, *KnE Engineering*. (2019). <https://doi.org/10.18502/keg.v4i3.5826>.
- [77] Z. Liu, M.S. Wong, J. Nichol, P.W. Chan, A multi-sensor study of water vapour from radiosonde, MODIS and AERONET: A case study of Hong Kong, *International Journal of Climatology*. 33 (2013) 109–120. <https://doi.org/10.1002/joc.3412>.
- [78] A.E. Niell, A.J. Coster, F.S. Solheim, V.B. Mendes, P.C. Toor, R.B. Langley, C.A. Upham, Comparison of measurements of atmospheric wet delay by radiosonde, water vapor radiometer, GPS, and VLBI, *J Atmos Ocean Technol*. 18 (2001) 830–850. [https://doi.org/10.1175/1520-0426\(2001\)018<0830:COMOAW.2.0.CO;2](https://doi.org/10.1175/1520-0426(2001)018<0830:COMOAW.2.0.CO;2).
- [79] K.-M. Lee, J.-H. Park, Retrieval of Total Precipitable Water from the Split-Window

- Technique in the East Asian Region, n.d.
- [80] C.Y. Wu, J. Mossa, L. Mao, M. Almulla, Comparison of different spatial interpolation methods for historical hydrographic data of the lowermost Mississippi River, *Ann GIS*. 25 (2019) 133–151. <https://doi.org/10.1080/19475683.2019.1588781>.
- [81] J.A. Sobrino, Z.L. Li, M.P. Stoll, F. Becker, Improvements in the Split-Window Technique for Land Surface Temperature Determination, *IEEE Transactions on Geoscience and Remote Sensing*. 32 (1994) 243–253. <https://doi.org/10.1109/36.295038>.
- [82] D. Chesters, L.W. Uccellini, W.D. Robinson, Low-level water vapor fields from the VISSR Atmospheric Sounder (VAS) “split window” channels, *Journal of Climate and Applied Meteorology*. 22 (1983).
- [83] V. V. Forsythe, T. Duly, D. Hampton, V. Nguyen, Validation of Ionospheric Electron Density Measurements Derived From Spire CubeSat Constellation, *Radio Sci.* 55 (2020). <https://doi.org/10.1029/2019RS006953>.
- [84] K. Aheieva, R. Rahmatillah, R. Ninagawa, I. Owulatobi Adebolu, S. Kim, Y. Kakimoto, T. Yamauchi, H. Masui, M. Cho, C. Chee Lap, Z. Ying, T. Man Siu, L. King Ho Holden, Project Overview of SPATIUM-I: A Technology Demonstration Mission Toward Global Three-Dimensional Ionosphere Mapping via CubeSat Constellation Equipped with an Atomic Clock, 2021. [www.jossonline.com](http://www.jossonline.com).
- [85] J.J. Braun, Remote Sensing of Atmospheric Water Vapor with the Global Positioning System A Dissertation, 1991.
- [86] L.M. Miloshevich, H. Vömel, T. Leblanc, Accuracy Assessment and Correction of Vaisala RS92 Radiosonde Water Vapor Measurements, n.d.
- [87] Y.-A. Liou, J.C. Liljegren, Y.-T. Teng, Comparison of Precipitable Water Observations in the Near Tropics by GPS, Microwave Radiometer, and Radiosondes Radiometrics View project Improvement and development of new methods of an analysis in the radio-physical and probe measurements for investigations of wave .. View project Comparison of Precipitable Water Observations in the Near Tropics by GPS, Microwave Radiometer, and Radiosondes, Article in *Journal of Applied Meteorology and Climatology*. (2001). [https://doi.org/10.1175/1520-0450\(2001\)0402.0.CO](https://doi.org/10.1175/1520-0450(2001)0402.0.CO).
- [88] Radiometrics, Profiling solutions that keep you Ahead of the Weather: Radiometrics, <https://www.Radiometrics.Com/>. (n.d.).

- [89] J.C. Antuña-Marrero, R. Román, V.E. Cachorro, D. Mateos, C. Toledano, A. Calle, J.C. Antuña-Sánchez, J. Vaquero-Martínez, M. Antón, Á.M. de Frutos Baraja, Integrated water vapor over the Arctic: Comparison between radiosondes and sun photometer observations, *Atmos Res.* 270 (2022). <https://doi.org/10.1016/j.atmosres.2022.106059>.
- [90] R. Philipona, A. Kräuchi, R. Kivi, T. Peter, M. Wild, R. Dirksen, M. Fujiwara, M. Sekiguchi, D.F. Hurst, R. Becker, Balloon-borne radiation measurements demonstrate radiative forcing by water vapor and clouds, *Meteorologische Zeitschrift.* 29 (2020) 501–509. <https://doi.org/10.1127/METZ/2020/1044>.
- [91] IEEE M A G A Z I N E A Publication of the IEEE Communications Society • Software Defined Radio-20 Years Later • Software Defined 5G Networks for Anything as a Service, n.d. [www.comsoc.org](http://www.comsoc.org).
- [92] Ettus Research, USRP™ B200mini Series Product Overview, n.d. [www.ni.com](http://www.ni.com) (accessed July 17, 2023).
- [93] GNU Radio, (n.d.). <https://www.gnuradio.org>. (accessed July 17, 2023).
- [94] Skytraq, Orion\_B16\_DS (1), (n.d.). <https://www.skytraq.com.tw/homesite/home-product> (accessed July 17, 2023).
- [95] AliExpress, Digital rf power amplifier 400-470mhz uhf 20w 30w 40w 50w 80w radio dmr amplifier fm power amplifier dmr. C4fm dpmrcw fm, <https://Ja.Aliexpress.Com/Item/1005003270063331.Html?GatewayAdapt=glo2jpn>. (n.d.).
- [96] Mini Circuits, RF, MW & mmWave Amplifiers, Mini Circuits. (n.d.). <https://www.minicircuits.com/WebStore/Amplifiers.html?interface=Conn.&subcategories=High%20Power%20Amplifier> (accessed September 18, 2023).
- [97] Digital Delay Generator, (n.d.). <https://www.thinksrs.com/products/dg535.html> (accessed September 21, 2023).
- [98] R. Radhakrishnan, W.W. Edmonson, F. Afghah, R. Martinez Rodriguez-Osorio, F. Pinto, S.C. Burleigh, Survey of Inter-Satellite Communication for Small Satellite Systems: Physical Layer to Network Layer View, n.d.
- [99] D. Bulanov, K. Ocheretyanyy, Y. Wang, Q. Bin Chen, Inter-Satellite Communication for LEO CubeSat Network: QoS Parameters and Feasibility of Massive MIMO, *Journal of Communications Technology and Electronics.* 63 (2018) 1174–1182. <https://doi.org/10.1134/S1064226918100054>.

- [100] R. Radhakrishnan, W. Edmonson, F. Afghah, R. Rodriguez-Osorio, F. Pinto, S. Burleigh, Survey of Inter-satellite Communication for Small Satellite Systems: Physical Layer to Network Layer View, (2016). <http://arxiv.org/abs/1609.08583>.
- [101] ESA, PRISMA (Prototype Research Instruments and Space Mission technology Advancement), (2012). <https://www.eoportal.org/satellite-missions/prisma-prototype#vbs-vision-based-sensor> (accessed September 17, 2023).
- [102] Z. Yoon, W. Frese, K. Briess, Design and implementation of a narrow-band intersatellite network with limited onboard resources for IoT, Sensors (Switzerland). 19 (2019). <https://doi.org/10.3390/s19194212>.
- [103] ESA, EDSN (Edison Demonstration of SmallSat Networks), EoPortal. (2014). <https://www.eoportal.org/satellite-missions/edsn#edsn-edison-demonstration-of-smallsat-networks> (accessed September 17, 2023).
- [104] J. Cockrell, R. Alena, D. Mayer, H. Sanchez, T. Luzod, B. Yost, D.M. Klumpar, EDSN: A Large Swarm of Advanced Yet Very Affordable, COTS-based NanoSats that Enable Multipoint Physics and Open Source Apps, n.d. <http://www.nasa.gov/offices/oct/home/i>.
- [105] QB50, WWW.QB50.EU, (n.d.). <https://www.qb50.eu/> (accessed September 17, 2023).
- [106] ESA, Proba-3 Mission, (n.d.). [https://www.esa.int/Enabling\\_Support/Space\\_Engineering\\_Technology/Proba\\_Missions/Proba-3\\_Mission#:~:text=Proba%2D3%20is%20devoted%20to,flying%20as%20one%20virtual%20structure.](https://www.esa.int/Enabling_Support/Space_Engineering_Technology/Proba_Missions/Proba-3_Mission#:~:text=Proba%2D3%20is%20devoted%20to,flying%20as%20one%20virtual%20structure.) (accessed September 17, 2023).
- [107] ESA, GRACE-FO (Gravity Recovery And Climate Experiment - Follow-On), EePortal. (2013). <https://www.eoportal.org/satellite-missions/grace-fo#Grace-FO.html.1> (accessed September 17, 2023).
- [108] J. Chen, A. Cazenave, C. Dahle, W. Llovel, I. Panet, J. Pfeffer, L. Moreira, Applications and Challenges of GRACE and GRACE Follow-On Satellite Gravimetry, Surv Geophys. 43 (2022) 305–345. <https://doi.org/10.1007/s10712-021-09685-x>.
- [109] S.J. Chung, S. Bandyopadhyay, R. Foust, G.P. Subramanian, F.Y. Hadaegh, Review of formation flying and constellation missions using nanosatellites, J Spacecr Rockets. 53 (2016) 567–578. <https://doi.org/10.2514/1.A33291>.
- [110] R. Agarwal, B. Oh, D. Fitzpatrick, A. Buynovskiy, S. Lowe, C. Lisy, A. Kriezis, B. Lan, Z.

- Lee, A. Thomas, B. Wallace, E. Costantino, G. Miner, J. Thayer, S. D'amico, K. Lemmer, W. Lohmeyer, S. Palo, [SSC21-WKI-02] Coordinating Development of the SWARM-EX CubeSat Swarm Across Multiple Institutions, n.d.
- [111] S.P. Ho, S. Kireev, X. Shao, X. Zhou, X. Jing, Processing and Validation of the STAR COSMIC-2 Temperature and Water Vapor Profiles in the Neural Atmosphere, *Remote Sens (Basel)*. 14 (2022). <https://doi.org/10.3390/rs14215588>.
- [112] M. Kirkko-Jaakkola, L. Leppälä, G. Ferrara, S. Honkala, M. Mäkelä, H. Kuusniemi, S. Miettinen-Bellevergue, Publications of the Ministry of Transport and Communications 2020:1 Challenges in Arctic Navigation and Geospatial Data User Perspective and Solutions Roadmap, n.d.
- [113] B. Cao, J.S. Haase, M.J. Murphy, M.J. Alexander, M. Bramberger, A. Hertzog, Equatorial waves resolved by balloon-borne Global Navigation Satellite System radio occultation in the Strateole-2 campaign, *Atmos Chem Phys*. 22 (2022) 15379–15402. <https://doi.org/10.5194/acp-22-15379-2022>.
- [114] A.M. Balakhder, M.M. Al-Khaldi, J.T. Johnson, On the Coherency of Ocean and Land Surface Specular Scattering for GNSS-R and Signals of Opportunity Systems, *IEEE Transactions on Geoscience and Remote Sensing*. 57 (2019) 10426–10436. <https://doi.org/10.1109/TGRS.2019.2935257>.
- [115] M.P. Rennie, L. Isaksen, F. Weiler, J. de Kloe, T. Kanitz, O. Reitebuch, The impact of Aeolus wind retrievals on ECMWF global weather forecasts, *Quarterly Journal of the Royal Meteorological Society*. 147 (2021) 3555–3586. <https://doi.org/10.1002/qj.4142>.
- [116] A.G. Straume, M. Rennie, L. Isaksen, J. de Kloe, G.-J. Marseille, A. Stoffelen, T. Flament, H. Stieglitz, A. Dabas, D. Huber, O. Reitebuch, C. Lemmerz, O. Lux, U. Marksteiner, F. Weiler, B. Witschas, M. Meringer, K. Schmidt, I. Nikolaus, A. Geiss, P. Flamant, T. Kanitz, D. Wernham, J. von Bismarck, S. Bley, T. Fehr, R. Floberghagen, T. Parinello, ESA's Space-Based Doppler Wind Lidar Mission Aeolus – First Wind and Aerosol Product Assessment Results, *EPJ Web Conf*. 237 (2020) 01007. <https://doi.org/10.1051/epjconf/202023701007>.
- [117] ESA, LAGEOS (Laser Geodynamics Satellite-I) / LAGEOS-II, <https://www.eoportal.org/satellite-missions/lageos#eop-quick-facts-section>. (2012). <https://www.eoportal.org/satellite-missions/lageos#eop-quick-facts-section> (accessed September 17, 2023).

- [118] J.-M. Friedt, F. Com, Software defined radio based Synthetic Aperture noise and OFDM (Wi-Fi) RADAR mapping, 2016.
- [119] GNU Radio - The Free & Open Source Radio Ecosystem · GNU Radio, (n.d.). <https://www.gnuradio.org/> (accessed April 3, 2023).
- [120] RapidTables, Binary to Text Translator, Webpage. (n.d.). <https://www.rapidtables.com/convert/number/binary-to-ascii.html> (accessed July 29, 2023).
- [121] B.C. Kindel, P. Pilewskie, K.S. Schmidt, T. Thornberry, A. Rollins, T. Bui, Upper-troposphere and lower-stratosphere water vapor retrievals from the 1400 and 1900 nm water vapor bands, *Atmos Meas Tech.* 8 (2015) 1147–1156. <https://doi.org/10.5194/amt-8-1147-2015>.
- [122] P. Sibanda, Particle precipitation effects on the South African ionosphere, n.d. <https://www.researchgate.net/publication/29806954>.
- [123] M. Kishimoto, N. Cihan Orger, H. Awny Elmegharbel, T. Dayarathna, P. Lepcha, T. Yamauchi, S. Kim, M. Teramoto, H. Masui, C. Mengu, C. Lap Chow, M.S. Tse, K. Ho, L. Holden, On-Orbit Observation of Total Electron Content in the Ionosphere by UHF Ranging Signal from the Ground, 2021.
- [124] F. Alshawaf, T. Fuhrmann, B. Heck, S. Hinz, A. Knoepfler, X. Luo, M. Mayer, A. Schenk, A. Thiele, M. Westerhaus, ATMOSPHERIC WATER VAPOUR DETERMINATION BY THE INTEGRATION OF INSAR AND GNSS OBSERVATIONS, 2011.
- [125] Michael Bevis, Steven Businger, Steven Chriwell, Thomas A Herring, Richard Anthes, Christian Rocken, Randolph H Ware, GPS Meteorology: Mapping Zenith Water Delays onto Precipitable Water, (n.d.).
- [126] ITU, Frequency Allocation Table Table-2 (27.5MHz-10000MHz), (n.d.). <https://www.tele.soumu.go.jp/resource/e/search/share/pdf/t2.pdf> (accessed July 9, 2023).
- [127] ITU, Footnotes to National Frequency Allocation of Japan (Column 4), (n.d.). <https://www.tele.soumu.go.jp/resource/e/search/share/pdf/fj.pdf> (accessed July 9, 2023).
- [128] M.G. Kibria, G.P. Villardi, K. Ishizu, F. Kojima, H. Yano, Resource allocation in shared spectrum access communications for operators with diverse service requirements, *EURASIP J Adv Signal Process.* 2016 (2016). <https://doi.org/10.1186/s13634-016-0381-8>.
- [129] A.A. Mohammed, A.S. Abdullah, Integrated Spectrum Sensing and Frequency Reconfigurable Antennas for Inter-Weave Cognitive-Radio Applications, in: *J Phys Conf*



- Ser, IOP Publishing Ltd, 2021. <https://doi.org/10.1088/1742-6596/1804/1/012053>.
- [130] V. Ristić, B. Todorović, N. Stojanović, Frequency hopping spread spectrum: History, principles and applications, *Vojnotehnicki Glasnik*. 70 (2022) 856–876. <https://doi.org/10.5937/vojtehg70-38342>.
- [131] L.T. Ong, Adaptive beamforming algorithms for cancellation of multiple interference signals, *Progress In Electromagnetics Research M*. 43 (2015) 109–118. <https://doi.org/10.2528/PIERM15061202>.
- [132] A. Ceriana Eska, Adaptive Modulation and Coding (AMC) around Building Environment for MS Communication at The Train, *EMITTER International Journal of Engineering Technology*. 6 (2018).
- [133] XMLRPC Server - GNU Radio, (n.d.). [https://wiki.gnuradio.org/index.php/XMLRPC\\_Server](https://wiki.gnuradio.org/index.php/XMLRPC_Server) (accessed April 3, 2023).
- [134] © electronics-notes, Radio Antenna Directivity, Gain & Polar Diagrams, <https://www.electronics-notes.com/articles/antennas-propagation/antenna-theory/gain-directivity.php>. (n.d.). <https://www.electronics-notes.com/articles/antennas-propagation/antenna-theory/gain-directivity.php> (accessed July 30, 2023).
- [135] D. Ochoa, K. Hummer, M. Ciffone, Deployable Helical Antenna for Nano-Satellites, n.d.
- [136] S. Lu, P.I. Theoharis, R. Raad, F. Tubbal, A. Theoharis, S. Iranmanesh, S. Abulgasem, M.U.A. Khan, L. Matekovits, A Survey on CubeSat Missions and Their Antenna Designs, *Electronics (Switzerland)*. 11 (2022). <https://doi.org/10.3390/electronics11132021>.
- [137] S. Abulgasem, F. Tubbal, R. Raad, P.I. Theoharis, S. Lu, S. Iranmanesh, Antenna Designs for CubeSats: A Review, *IEEE Access*. 9 (2021) 45289–45324. <https://doi.org/10.1109/ACCESS.2021.3066632>.
- [138] Waleed Alomar, Jonas Degnan, teven Mancewicz, Matthew Sidley, James Cutler, Brian Gilchrist, An Extendable Solar Array Integrated Yagi-Uda UHF Antenna for CubeSat Platforms, In *Proceedings of the 2011 IEEE International Symposium on Antennas and Propagation (APSURSI)*. (2011) 3022–3024.
- [139] R.E. Hodges, O. Scott Sands, J. Huang, S. Bassily, High-Capacity Communications from Martian Distances Part 4: Assessment of Spacecraft Pointing Accuracy Capabilities Required For Large Ka-Band Reflector Antennas, n.d.
- [140] F. Santoni, F. Piergentili, S. Donati, M. Perelli, A. Negri, M. Marino, An innovative

- deployable solar panel system for Cubesats, *Acta Astronaut.* 95 (2014) 210–217. <https://doi.org/10.1016/j.actaastro.2013.11.011>.
- [141] Canonical Ltd. Ubuntu, Install Ubuntu Server, Ubuntu.Com. (2023). <https://ubuntu.com/tutorials/install-ubuntu-server#1-overview> (accessed July 22, 2023).
- [142] H.H. Abdullah, A. Elboushi, A.E. Gohar, E.A. Abdallah, An Improved S-Band CubeSat Communication Subsystem Design and Implementation, *IEEE Access.* 9 (2021) 45123–45136. <https://doi.org/10.1109/ACCESS.2021.3066464>.